POLITECNICO DI TORINO

Collegio di Ingegneria Chimica e dei Materiali

Master of Science Course

in Materials Engineering

Master of Science Thesis

Polymer Nanocomposites based on UV-Curable Thiol-Ene System and Surface-Modified Cellulose Nanofibrils for Bio-Inspired Super-Hydrophobic Coatings

Politecnico di Torino

Tutors

Prof. Marco Sangermano

Dr. Yves Leterrier

Candidate

Enrico Sola 290008

October 2022

Contents

Summary ..... **i**
List of Abbreviations I
List of Figures II
List of Tables IV
1. Introduction 1
1.1. Motivation 1
1.2. Research Objectives 1
1.3. Structure of the Thesis 2
2. State of Art 3
2.1. Photopolymerization 3
2.1.1. Definition 3
2.1.2. UV Light Photoinitiation 3
2.1.3. Photopolymerization Mechanisms 4
2.1.3.1. Free Radical Photopolymerization 4
2.1.3.2. Cationic Photopolymerization 5
2.2. “Click” Reactions 5
2.3. Thiol-Ene Reactions 6
2.3.1. Thiol-Ene Reaction Features 6
2.3.2. Thiol-Ene Reaction Applications 7
2.3.3. Thiol-Ene Drawbacks and Improvement 8
2.4. Cellulose 8
2.4.1. Cellulose Features and Sustainability 8
2.4.2. Cellulose Sources 8
2.4.3. Cellulose Structure 9
2.4.4. Nanocellulose 10
2.4.4.1. Cellulose Nanofibrils (CNFs) 11
2.4.4.2. TEMPO-Oxidized CNFs 13
2.5. Nanocomposites 15
2.5.1. Second Phase Morphologies 15
2.5.1.1. Nanoparticles 15
2.5.1.2. Nanoclays 16
2.5.1.3. Nanofibers 16
2.5.2. Nanocomposite Advantages and Limitations 17
2.5.3. Polymer Nanocomposites 18

2.5.3.1. Cellulosic Polymer Nanocomposites and their Applications 18
2.5.4. Thiol-Ene Chemistry and Nanocellulose 19
2.5.4.1. Thiol-Ene Systems in UV Nanoimprint Lithography (UV-NIL) 19
2.6. Nature-Inspired Hierarchical Surfaces with Micro- and Nano-Structures 20
2.6.1. “Lotus Effect” and “Rose Petal Effect” 20
2.6.2. Replication of Rose Petal and Lotus Leaf Hierarchical Surfaces 21
3. Materials and Methods 22
3.1. Selection and Categorization of Resin Contents 22
3.2. Preparation of TOCNF surface chemistry modifiers 23
3.2.1. Pre-Hydrolysis of Modifiers with Ene and Thiol Moieties 23
3.2.2. TOCNFs Surface Modfication with Bu_4NOH by Ion Exchange 24
3.3. Preparation of Composite Films 24
3.3.1. Processing of Reference Resin without Fillers 24
3.3.2. Processing of Nanocomposite Films 25
3.3.3. Photo-Crosslinking of Thiol-Ene Nanocomposites with as received TOCNFs 25
3.3.4. Photo-Crosslinking of Thiol-Ene Nanocomposites with hyMPS/hyMPTMS-Modified TOCNFs 26
3.3.5. Photo-Crosslinking of Thiol-Ene Nanocomposites with Bu_4NOH-Modified TOCNFs 27
3.3.6. Photo-Crosslinking of Thiol-Ene Nanocomposites with Double Modified TOCNFs 27
3.4. Replication of Micro- and Nano-Structured Lotus Leaf Surface to obtain Super-Hydrophobic Films 28
3.5. Characterization Methods 28
3.5.1. Fourier Transform-Infrared (FT-IR) Spectroscopy 28
3.5.2. Zeta Potential Measurements 29
3.5.3. Ultraviolet-Visible Light (UV-Vis) Spectroscopy 30
3.5.4. Thermogravimetric Analysis (TGA) 30
3.5.5. Rheology Analysis 30
3.5.6. Photo-Rheology Analysis 31
3.5.7. Photo-Differential Scanning Calorimetry (Photo-DSC) 31
3.5.8. Nanoindentation Measurements 31
3.5.9. Contact Angle Measurements and Self-Cleaning Test 32
3.5.10. Scanning Electron Microscopy (SEM) 32
4. Results and Discussion 33
4.1. Optimization of the Cured Reference and Composite Films Preparation Method 33
4.2. Material Properties of TOCNFs and Modified TOCNFs 34

4.2.1. Thermal Stability of TOCNFs 34
4.2.2. TOCNFs Surface Modifications 35
4.3. Characteristics of Reference and Composite Resins 38
4.3.1. Rheological Behaviour of Reference and Composite Resins 38
4.3.2. UV-Curing of Reference and Composite Resins 39
4.4. Material Properties of Cured Reference and Composite Films 42
4.4.1. Transmission and Transparency Properties of Cured Reference and Composite Films 42
4.4.2. Thermal Stability of Cured Reference and Composite Films 43
4.4.3. Surface Properties of Cured Reference and Composite Films 44
5. Conclusions 49
Acknowledgements 51
References 52

Summary

This section summarises the content of the thesis, in Italian, as required by Politecnico di Torino in its guidelines.

Introduzione

Motivazione

La chimica, definita "click" chemistry, che contraddistingue i sistemi tiolo-ene appare molto promettente in quanto consente di attuare reazioni di foto-polimerizzazione rapide, non ostacolate dalla presenza di ossigeno e non caratterizzate dalla generazione di prodotti secondari, mediante irraggiamento con radiazioni UV. Nonostante ciò, i polimeri tiolo-ene sono caratterizzati da basse proprietà meccaniche, pertanto una soluzione efficace può essere la produzione di compositi tramite l'incorporazione di cariche per rafforzarli. A questo scopo, sono state scelte le nanofibrille di cellulosa (CNFs), un materiale bio-based ottenibile da numerose risorse naturali a partire dalla cellulosa.

A causa della loro natura idrofila, risulta complicato incorporarle in un mezzo organico come una resina polimerica. Per risolvere questo problema, è possibile applicare modificazioni superficiali per migliorarne la compatibilità con la matrice.

Inoltre, in questo progetto è fondamentale, per la processabilità con luce UV, mantenere la trasparenza caratteristica del sistema tiolo-ene scelto, quindi l'ottimizzazione del processing e l'impiego di step specifici, volti ad aumentare la dispersione del filler, sono essenziali. Questo approccio permette anche di sfruttare efficacemente il rinforzo associato all'incorporazione dei nanofiller, che sono caratterizzati da un'area superficiale specifica molto elevata quando ben dispersi.

Obiettivi della Ricerca

L'obiettivo primario di questo progetto di tesi è valutare la processabilità delle nanofibrille di cellulosa (CNFs) come cariche all'interno di un sistema tiolo-ene foto-polimerizzabile tramite luce UV, al fine di produrre materiali nanocompositi.

In particolare, è essenziale ottenere una buona dispersione dei nanofiller allo scopo di massimizzare la loro efficacia nel migliorare le proprietà della matrice. Per raggiungere questo obiettivo, sono stati proposti diversi approcci, tra cui la modificazione superficiale delle CNFs al fine di aumentarne la compatibilità con il polimero e l'ottimizzazione delle fasi di lavorazione.

È stata eseguita una caratterizzazione completa sia delle materie prime che dei film nanocompositi prodotti con diverse concentrazioni di filler, concentrandosi sulle proprietà meccaniche, ottiche e superficiali, oltre che sui principali parametri legati alla foto-reticolazione e al processing della resina, come la viscosità, con lo scopo di valutare l'influenza della presenza delle CNFs funzionalizzate.

Per dimostrare l'utilità di questa ricerca, è stata proposta un'applicazione dimostrativa. In particolare, è stata utilizzata la tecnica di UV nanoimprint lithography (UV-NIL) per replicare superfici bio-inspired caratterizzate da strutture gerarchiche di dimensioni micro- e nano-metriche, con l'obiettivo di produrre superfici super-idrofobiche e trasparenti con migliorate proprietà meccaniche.

Struttura della tesi

La tesi è suddivisa in cinque capitoli, i restanti quattro sono organizzati nel seguente ordine: Stato dell'arte, Materiali e Metodi, Risultati e Discussione, Conclusioni.

Il Capitolo 2 presenta lo stato dell'arte per quanto riguarda i settori scientifici correlati all'area di ricerca. Argomenti come la foto-polimerizzazione, le reazioni "click" e i sistemi tiolo-ene, la cellulosa e le nanofibrille di cellulosa, i nanocompositi e la replica di superfici bio-inspired, sono stati presentati per fornire una panoramica delle sfide legate a questo progetto.

Il Capitolo 3 descrive in dettaglio i metodi di sintesi e caratterizzazione utilizzati durante il processing dei materiali. In particolare, sono state illustrate le specie utilizzate per produrre le resine, la preparazione dei modificatori di superficie delle CNFs, la fabbricazione dei film compositi, la procedura per produrre le repliche della superficie gerarchica della foglia di loto e i metodi di caratterizzazione.

Il Capitolo 4 illustra i risultati ottenuti e offre un commento critico, oltre a una discussione basata su ragionamenti e ipotesi personali. In particolare, l'attenzione si è concentrata sia

sull'ottimizzazione delle fasi di lavorazione sia sull'analisi delle proprietà delle resine, delle CNFs funzionalizzate e dei film compositi foto-polimerizzati con raggi UV.

Infine, il Capitolo 5 sintetizza i principali risultati ottenuti, oltre a fornire idee e suggerimenti per possibili ricerche future.

Materiali e Metodi

Materiali

I materiali utilizzati per la produzione di resine nanocomposite sono stati elencati nella Tabella 1 insieme al loro ruolo e alle loro proprietà.

Tabella 1: Elenco dei materiali utilizzati per la preparazione delle resine nanocomposite.

Name	Acronym	Molecular formula	Brand	Molecular weight (g/mol)	Purity / Concentration	Role
Trimetilolpropano diallil-etere	TMPDE	$C_{12}H_{24}O$	Sigma Aldrich	214.30	90%	Monomero Ene
Trimetilolpropano tris (3mercaptopropionato)	TMPTMP	$C_{15}H_{26}O_6S_3$	Sigma Aldrich	398.56	≥95%	Monomero Tiolo
2,2-dimetossi-2-fenilacetofenone	DMPA	$C_{16}H_{16}O_3$	TCI Chemicals	256.30	>98%	Fotoiniziatore
Idrossitoluene butilato	BHT	$C_{15}H_{24}O$	Sigma Aldrich	220.35	≥99%	Inibitore
Nanofibrille di cellulosa TEMPO-ossidate (sospensione H2O)	TOCNFs	-	University of Maine	-	1 wt.%	Filler
3-(Metacrilossi) propil-trimetossisilano	MPS	$C_{10}H_{20}O_5Si$	Sigma Aldrich	248.35	98%	Modificatori superficiali delle TOCNFs
3-(Mercaptopropile) trimetossisilano	MPTMS	$C_6H_{16}O_3SSi$	Sigma Aldrich	196.34	95%	
Idrossido di tetrabutilammonio	Bu_4NOH	$C_{16}H_{37}NO$	Sigma Aldrich	259.47	40 wt.%	
Acetone	-	C_3H_6O	Thommen-Furler	58.08	≥99.5%	Solvente

Preparazione dei film nanocompositi

Al fine di aumentare la compatibilità delle TOCNFs con la matrice polimerica, sono state applicate due modificazioni superficiali. In particolare, l'MPS e l'MPTMS hanno dovuto subire una pre-idrolisi in modo da generare dei gruppi OH sulle molecole (Figure 1 e 2) in grado di condensare con i gruppi OH della cellulosa per formare un legame stabile, a differenza del Bu_4NOH che è stato impiegato senza necessità di ulteriori reazioni.

Il procedimento per effettuare i processi di pre-idrolisi è riportato di seguito.

Miscelando 1.5 g di acido cloridrico (HCl) in 24.5 g di acqua (circa 6 wt.%) è stata ottenuta una soluzione acquosa con pH = 1, dopodiché 10 g di MPS sono stati miscelati con 2.2 g di soluzione acquosa con pH = 1 insieme a 1.25 g di etanolo per migliorare la miscibilità tra MPS e acqua, fino a ottenere un pH = 4. La soluzione omogenea così ottenuta è stata sottoposta a stirring magnetico a 1000 rpm a temperatura ambiente per tutta la notte per garantire la reazione di idrolisi dell'MPS. Infine, il materiale è stato degasato in un forno sotto-vuoto (70 mbar, 50 °C) per 1.5 ore per far evaporare l'acqua residua e ottenere MPS idrolizzato puro.

La stessa procedura e le stesse quantità sono state utilizzate anche per la pre-idrolisi del MPTMS.

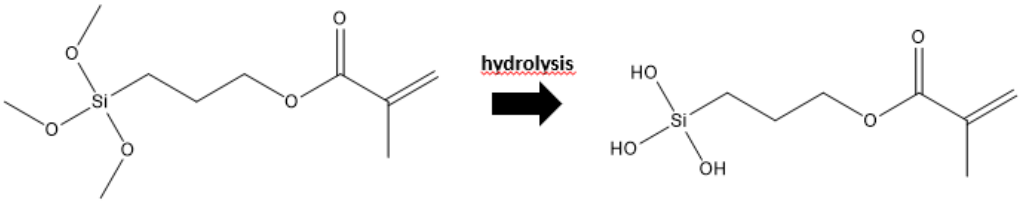

Figura 1- Rappresentazione schematica del processo di pre-idrolisi dell'MPS.

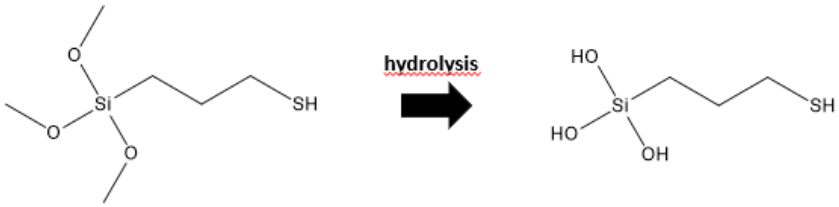

Figura 2- Rappresentazione schematica del processo di pre-idrolisi dell'MPTMS.

Dopodichè, sono state preparate le resine nanocomposite con differenti combinazioni di modificazioni superficiali e concentrazioni di fillers, oltre alla resina a base tiolo-ene pura da utilizzare come riferimento per il confronto delle proprietà. Al termine di numerosi esperimenti, è stato osservato che per ottenere una resina nanocomposita processabile, completamente priva di solvente, trasparente, con una ottima dispersione e una distribuzione omogenea delle nanofibrille di cellulosa, è necessario applicare entrambe le modificazioni. Il metodo ottimizzato per il processing dei materiali è descritto di seguito; l'acetone è stato scelto come solvente grazie alla buona dispersione delle TOCNFs al suo interno e per l'elevata velocità di evaporazione, fondamentale per ridurre i tempi di processo.

Una certa quantità di sospensione acquosa di TOCNFs (1 wt.%), in particolare 6 g, è stata miscelata con la sospensione acquosa di Bu_4NOH (40 wt.%), circa 200 mg, in modo da raggiungere un rapporto in peso di 1:1 tra TOCNFs e Bu_4NOH. Quindi è stato applicato uno step di ultrasonificazione, con un ciclo di lavoro composto da 15 s di impulso e 30 s di pausa per un tempo totale di impulso di 5 minuti e una potenza di 55 W, per una miscelazione ottimale. Dopodichè, il solvent exchange tra acqua e acetone è stato eseguito mediante centrifugazione (Heraeus Biofuge Primo, Thermo Scientific, Svizzera) a 6000 rpm per 10 minuti, rimuovendo la parte liquida e aggiungendo ogni volta 5 mL di solvente fresco (operazione ripetuta 3 volte), consentendo anche la rimozione del Bu_4NOH in eccesso non legato alle TOCNFs.

In seguito, le nanofibrille di cellulosa sono state modificate anche con l'MPS (o l'MPTMS) pre-drolizzato, aggiungendo alla sospensione di acetone e filler una certa quantità di hyMPS (o hyMPTMS) per raggiungere un rapporto in peso di 1:1 rispetto alle TOCNFs, ovvero circa 70 mg. La miscelazione ottimale è stata assicurata tramite ultrasonificazione a 55 W per 5 minuti totali di impulso, come descritto precedentemente nel caso del Bu_4NOH. Infine, per rimuovere l'hyMPS (o l'hyMPTMS) in eccesso è stata utilizzata la centrifuga, con rimozione della parte liquida e aggiunta di 5 mL di solvente fresco (operazione ripetuta 3 volte).

Un ulteriore step di ultrasonificazione è stato applicato per garantire una migliore dispersione, questa volta con un ciclo di lavoro composto da 15 s di impulso e 1 minuto di pausa per un tempo totale di impulso di 15 minuti e una potenza di 165 W.

La resina foto-reticolabile a base tiolo-ene è stata preparata miscelando i monomeri TMPDE (ene) e TMPTMP (tiolo) con un rapporto di funzionalità molare 1:1, 1 wt.% di DMPA (fotoiniziatore) e 9 mmol/l di BHT (inibitore). Un'ulteriore fase di ultrasonificazione, con i parametri precedentemente descritti e un controllo della temperatura < 50 °C per evitare la polimerizzazione termicamente indotta, è stata effettuata per ottimizzare la miscelazione.

La rimozione del solvente è avvenuta sotto cappa a temperatura ambiente, attendendo tutta la notte e coprendo la resina con un foglio di alluminio per evitare l'esposizione alla luce. La completa evaporazione del solvente è stata provata dal raggiungimento di una massa costante nel tempo.

La resina nanocomposita è stata successivamente depositata su un substrato di vetro tramite la tecnica “doctor blade” manuale, ad ottenere un film di circa 200 µm di spessore.

Infine, il film è stato fotoreticolato mediante luce UV (ECE PC-2000, Dymax, USA) tramite l’esposizione per 1 min ad una radiazione di intensità luminosa pari a 75 mW/cm^2.

Per quanto riguarda la preparazione dei film processati tramite UV nanoimprint lithography (UV-NIL) per replicare la superficie gerarchizzata delle foglie di loto, il metodo utilizzato è il seguente.

Una replica in negativo della superficie della foglia di Nelumbo Lutea (loto) è stata inizialmente prodotta in polidimetilsilossano (PDMS). Il PDMS è stato miscelato con l'agente indurente (presente con esso nel Sylgard 184 Silicone Elastomer Kit, Dow, Germania) con un rapporto in peso di 10:1, rispettivamente 80 g e 8 g, fino a ottenere una miscela omogenea, che è stata poi degasata per 10 min. In parallelo, le foglie di loto sono state tagliate per ottenere dei quadratini di 2x2 cm^2, poi posizionati sul fondo di una piastra di Petri con uno scotch biadesivo della stessa. Dopo il degasaggio, la miscela di PDMS e agente indurente è stata versata nella piastra di Petri fino a ricoprire completamente le foglie con uno strato sufficientemente spesso. Quindi la piastra di Petri è stata degasata ulteriormente per 20 minuti al fine di rimuovere completamente le bolle d'aria generate dalla miscelazione. Sono necessarie 48 ore a temperatura ambiente per assicurare la completa polimerizzazione del PDMS, dopodiché i quadratini patternati sono stati ritagliati e raccolti. Successivamente, la resina nanocomposita è stata depositata su un substrato di poli(metacrilato di metile) (PMMA) utilizzando la tecnica “doctor blade” manuale per ottenere un film spesso circa 200 µm. Il template negativo in PDMS è stato posizionato sulla resina e su di esso è stata applicata una pressione di 2 bar. Infine, dopo aver atteso un tempo di creep di 2 o 5 minuti per consentire alla

resina di fluire in tutta la nanostruttura, il sistema è stato esposto alla luce UV a 75 mW/cm^2 di intensità luminosa per 3 minuti per assicurare una completa fotoreticolazione.

Una volta rimosso il template negativo in PDMS dalla parte superiore, è stato ottenuto il film nanostrutturato che rappresenta la replica positiva della superficie gerarchizzata del loto.

Preparazione dei campioni e Caratterizzazione

Spettroscopia Infrarossa in trasformata di Fourier (FT-IR)

La tecnica FT-IR è stata utilizzata per valutare la reazione tiolo-ene tra TMPDE e TMPTMP e l'efficacia delle modifiche superficiali dei TOCNFs. In particolare, è stato utilizzato lo spettrometro Nicolet 6700 FT-IR (Thermo Fisher Scientific, USA) per l'analisi in un intervallo di numero d'onda compreso tra 650 e 4000 cm-1.

L'efficacia della modifica superficiale dei TOCNF con Bu_4NOH e hyMPS o hyMPTMS è stata testata confrontando gli spettri FT-IR dei TOCNF non modificati e modificati, in particolare utilizzando campioni costituiti da nanofibrille di cellulosa essiccate e incorporate in una pastiglia di bromuro di potassio (KBr) attraverso la procedura descritta di seguito.

Una determinata quantità di sospensione di TOCNFs, in particolare 6 g, ha subito un solvent exchange con acetone mediante centrifugazione a 6000 rpm per 10 minuti (3 volte) per beneficiare di una evaporazione del solvente più rapida negli step successivi. Quindi, il solvente è stato completamente evaporato mediante trattamento termico in forno a 120 °C. Infine, la polvere ottenuta, circa 60 mg, è stata mescolata con polvere di KBr per ottenere una concentrazione di 1.5% in peso e quindi pressata per 2 minuti a 10 bar per formare la pastiglia, che è stata successivamente mantenuta in forno a 120 °C per 2 giorni per garantire la completa rimozione dell'umidità residua.

La stessa procedura è stata seguita anche per le TOCNFs modificate con Bu_4NOH dopo aver mescolato la sospensione acquosa di Bu_4NOH con quella delle TOCNFs, in particolare utilizzando una quantità tale da ottenere un rapporto in peso di 1:1. Lo step di solvent exchange (ripetuto 3 volte) ha anche permesso di rimuovere il Bu_4NOH in eccesso non legato alla superficie delle nanofibrille di cellulosa.

Nel caso delle TOCNFs modificate con hyMPS e hyMPTMS, la miscelazione con i modificatori superficiali ha avuto luogo dopo la fase di solvent exchange ed è stata aggiunta una fase di lavaggio con solvente fresco mediante centrifugazione (3 volte) per rimuovere il silano in eccesso.

Potenziale Zeta

Per ulteriori indagini sulla modificazione superficiale delle TOCNFs con Bu_4NOH, sono state eseguite delle misurazioni del potenziale zeta con lo Zetasizer Nano ZS (Malvern Panalytical, Regno Unito).

I campioni analizzati consistevano in una sospensione di acqua diluita allo 0.1% in peso di TOCNFs e di TOCNFs modificati con Bu_4NOH.

Spettroscopia UV-Visibile (UV-Vis)

Le analisi di spettroscopia UV-Vis sono state effettuate con lo spettrofotometro Lambda 365 UV-Vis (PerkinElmer, USA) in un intervallo di lunghezze d'onda compreso tra 250 e 700 nm in trasmittanza, al fine di valutare la trasparenza dei film nanocompositi rispetto al film di resina tiolo-ene pura.

Analisi Termogravimetrica (TGA)

La TGA è stata utilizzata per valutare la degradazione termica di vari materiali, tra cui la resina tiolo-ene polimerizzata con raggi UV, la polvere di TOCNF essiccata e il film nanocomposito, allo scopo di confrontarne la stabilità termica. La polvere di TOCNF è stata ottenuta seguendo la stessa procedura descritta per la preparazione dei campioni per l'analisi FT-IR, senza incorporare la polvere nella pastiglia di KBr.

In particolare, campioni di circa 10 mg sono stati analizzati in flusso d'aria con una rampa di temperatura da 30 a 600 °C a una velocità costante di 10 °C/min, utilizzando l'analizzatore termogravimetrico TGA 4000 (PerkinElmer, USA).

Analisi Reometrica

Il comportamento reologico dei monomeri (TMPDE e TMPTMP), delle resine tiolo-ene e nanocomposite, prima della fotopolimerizzazione, è stato analizzato con il reometro MCR 302e (Anton-Paar, Austria) nella configurazione piatto-piatto (25 mm di diametro). I campioni di circa 500 µL sono stati sottoposti a una velocità di taglio compresa tra 0.1 e 100 1/s.

Analisi Foto-Reometrica

Il reometro AR 2000ex (TA Instruments, USA) è stato utilizzato per eseguire le analisi di foto-reologia al fine di valutare la fotopolimerizzazione delle resine nanocomposite rispetto alla resina tiolo-ene pura.

In particolare, i campioni di circa 100 µL sono stati sottoposti a radiazioni UV di intensità luminosa pari a 5.5 mW/cm2 tramite la lampada OmniCure UV3-Surface Cure da 200 W Series 2000 (Exfo, Canada) dopo 20 s di pre-sollecitazione, mantenendo l'applicazione di una deformazione dell'1% con frequenza di 1 Hz, a temperatura ambiente (25 °C); l'intensità luminosa è stata misurata e calibrata utilizzando il radiometro UV Silver Line (CON-TROL-CURE, Germania).

Foto-Calorimetria a Scansione Differenziale (Photo-DSC)

Per valutare l'effetto delle modifiche superficiali sulla cinetica della fotoreticolazione, è stata effettuata un'analisi foto-DSC su campioni di circa 20 mg applicando un'intensità luminosa UV di 05 mW/cm2 dopo 2 minuti di attesa (per consentire il raggiungimento di una condizione stabile) per circa 20 minuti per garantire il completamento della reazione, a temperatura ambiente (25 °C). L'intensità luminosa di 0.5 mW/cm2 è stata utilizzata per consentire una reazione più lenta che rendesse possibile seguire la cinetica con maggiore precisione.

In particolare, ci si è focalizzati sull'effetto sia della concentrazione di TOCNFs che sulla tipologia di modificazione superficiale applicata alle nanofibrille di cellulosa.

Nanoindentazione

L'effetto sulle proprietà meccaniche dei film prodotti, legato all'aggiunta di TOCNFs, è stato valutato attraverso misure di nanoindentazione, in particolare concentrandosi sulle variazioni di proprietà come il modulo e la durezza superficiale.

I test sono stati eseguiti sui film nanocompositi co,nfrontati con le proprietà del film di resina tiolo-ene pura.

In particolare, è stato utilizzato il nanoindentatore Hysitron TI 950 TriboIndenter (Bruker, USA) applicando da 16 a 100 indentature con forza da 10 a 150 µN e utilizzando la legge di potenza per il fitting delle curve di unloading.

Misurazioni dell'Angolo di Contatto e Test di Self-Cleaning

Le misurazioni degli angoli di contatto sono state effettuate con il goniometro DSA20E Easy Drop (Krüss, Germania), per verificare la bagnabilità delle superfici dei film nanocompositi rispetto al film di resina tiolo-ene pura. In particolare, è stato utilizzato il metodo "sessile drop" depositando 2 µL di gocce di diversi liquidi, polari e non, come acqua, glicole etilenico e diiodometano (Tabella 2), a temperatura ambiente (25 °C). Per ogni campione sono state ripetute 3 misurazioni per ogni liquido.

Tabella 2: Contributi di energia superficiale dei diversi liquidi utilizzati per i test di angolo di contatto.

Liquido	**Contributo di Energia Superficiale [mN/m]**		
	Polare	**Dispersivo**	**Totale**
Acqua	51.0	21.8	72.8
Glicole Etilenico	19.0	29.0	48.0
Diiodometano	0.0	50.8	50.8

Inoltre, è stato misurato anche l'angolo di contatto dell'acqua dei film patternati con la replica della superifcie della foglia di loto, ma depositando gocce di 8 µL.

Infine, il test di self-cleaning è stato eseguito sul film nanocomposito patternato, posizionando dei granelli di pepe sulla superficie, inclinandola e facendovi cadere sopra delle gocce d'acqua. Le proprietà autopulenti sono verificate nel caso in cui l'acqua sia in grado di intrappolare i granelli di pepe, particelle idrofobiche, scivolando sulla superficie.

Microscopia Elettronica a Scansione (SEM)

I campioni per l'analisi al SEM sono stati preparati immobilizzandoli sui porta-campioni utilizzando un nastro biadesivo di carbonio. Inoltre, è stato applicato un sottile foglio di rame con una colla conduttiva tra la superficie del campione e il supporto metallico per ridurre il più possibile l'accumulo di carica elettrostatica. Successivamente, sui campioni è stato depositato uno strato di Iridio di 10 nm utilizzando il multi-coater Q150T (Quorum Technologies, UK) per rendere la superficie conduttiva e quindi analizzabile al SEM. L'iridio è stato scelto perché permette di ottenere

un rivestimento più liscio e omogeneo, anche se molto sottile, rispetto all'oro e quindi consente di analizzare la morfologia superficiale con un ingrandimento maggiore e una risoluzione più elevata.

In particolare, sono stati analizzati il template in PDMS, che rappresenta la replica negativa della superficie nanostrutturata della foglia di loto, e i film patternati con tecnica UV-NIL, che mostrano la replica positiva della superficie della foglia di loto, realizzati con resina tiolo-ene pura e resina nanocomposita con 0.5%vol di Bu_4NOH-hyMPS-TOCNF. Le immagini sono state acquisite con l'analizzatore SEM (Gemini-SEM 300, Zeiss, USA) utilizzando il rivelatore In-Lens a una distanza di lavoro di 3 mm e una tensione di accelerazione di 1 kV, oltre al rivelatore esterno di elettroni secondari (SE2) a una distanza di lavoro di 6 mm e una tensione di accelerazione di 3 kV.

Risultati e Discussione

Caratterizzazione delle TOCNFs e delle TOCNFs funzionalizzate

Stabilità termica delle TOCNFs

I risultati della TGA (Figura 3) mostrano che le TOCNFs sono caratterizzate da una temperatura di onset della degradazione termica di circa 215 °C. Il processo di degradazione termica è caratterizzato da tre fasi: disidratazione, depolimerizzazione e decomposizione delle unità glicosiliche, come mostrato anche dai risultati della TGA in derivata (DTGA); inoltre, presentano circa 7-8 wt.% di char residuo a 600 °C.

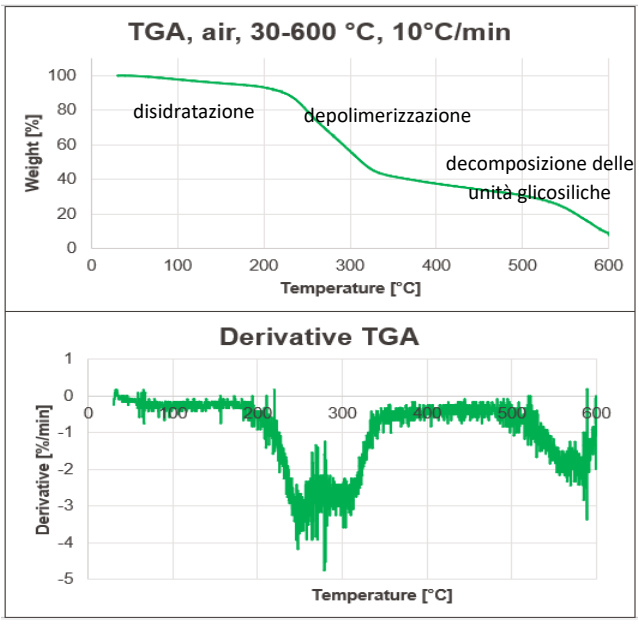

Figura 3- Curve di TGA e TGA in derivata (DTGA) della polvere di TOCNFs essiccate, valutate in aria tra 30 °C e 600 °C con una rampa di temperatura di 10 °C/min.

Modificazione superficiale delle TOCNFs

L'effettivo avvenimento della modifica superficiale delle TOCNFs con l'hyMPS è dimostrato dall'aumento dell'assorbimento nel picco del gruppo carbonilico (C=O, circa 1720 cm^{-1}) (Figura 4), già presente nello spettro delle nanofibrille di cellulosa a causa della TEMPO-ossidazione, dovuta alla presenza di gruppi carbonilici nelle molecole di hyMPS.

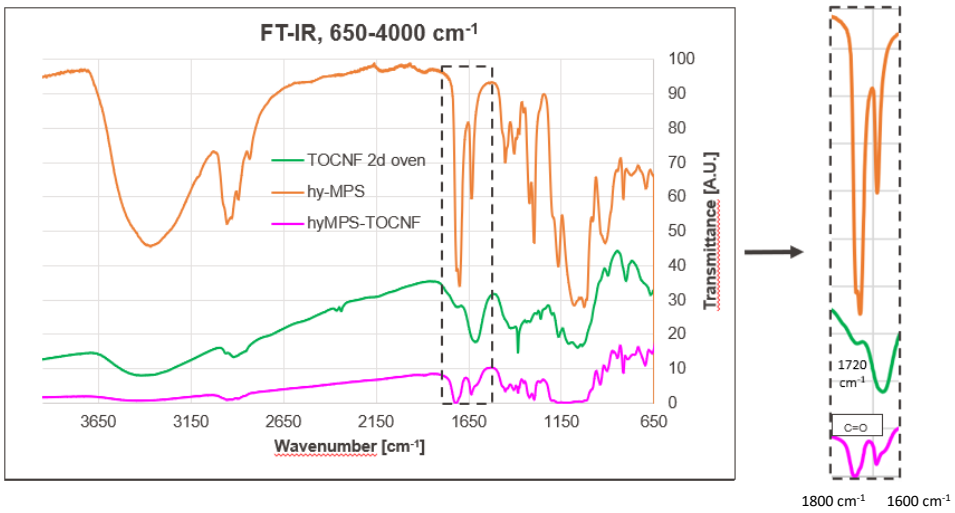

Figura 4- Spettri FT-IR delle TOCNFs essiccate (inserite nella pastiglia di KBr), MPS idrolizzato puro e TOCNFs modificate con hyMPS essiccate (inserite nella pastiglia di KBr).

La modifica delle TOCNFs da parte dell'hyMPTMS è dimostrata dalla comparsa del picco relativo al gruppo tiolo (SH) (circa 2550 cm^{-1}) (Figura 5), presente nelle molecole di hyMPTMS. L'ampiezza del picco è bassa ma chiaramente visibile rispetto allo spettro delle TOCNFs non funzionalizzate, dove non è presente.

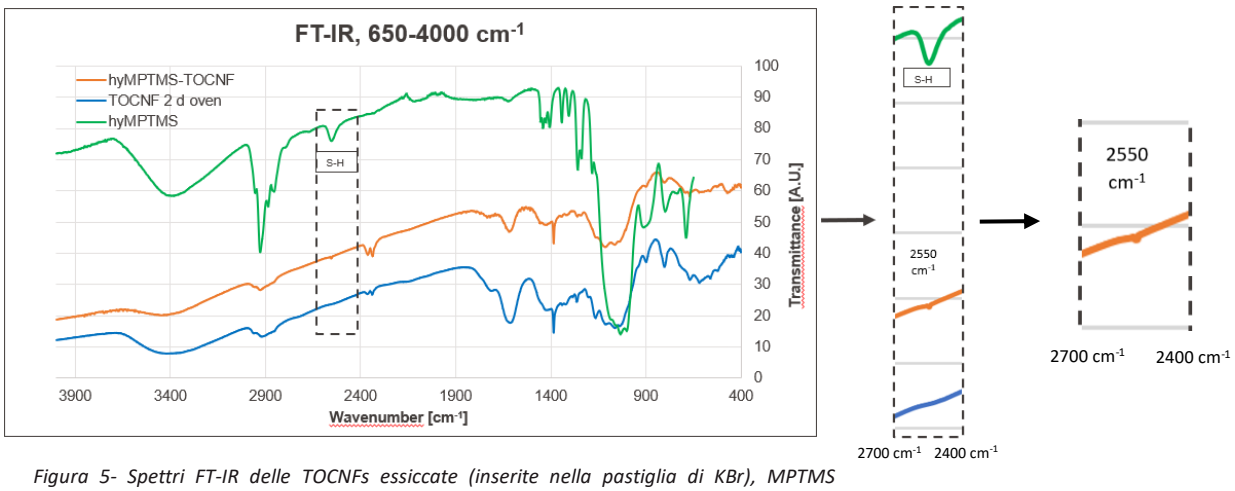

Figura 5- Spettri FT-IR delle TOCNFs essiccate (inserite nella pastiglia di KBr), MPTMS idrolizzato puro e TOCNFs modificate con hyMPTMS essiccate (inserite nella pastiglia di KBr).

La presenza di tetrabutilammonio legato alla superficie delle nanofibrille di cellulosa è dimostrata dal red-shift del picco del gruppo carbonilico C=O (circa 1720 cm^{-1}) appartenente alle TOCNFs (Figura 6), dovuto all'aumento della densità elettronica e alla formazione di legami ionici permanenti tra COO- e N+, che sostituiscono i legami covalenti con gli atomi di H, in relazione alla struttura stabile simile a un sale che si è generata. Il red-shift rende il picco C=O dominato dal più intenso picco adiacente (circa 1650 cm^{-1}).

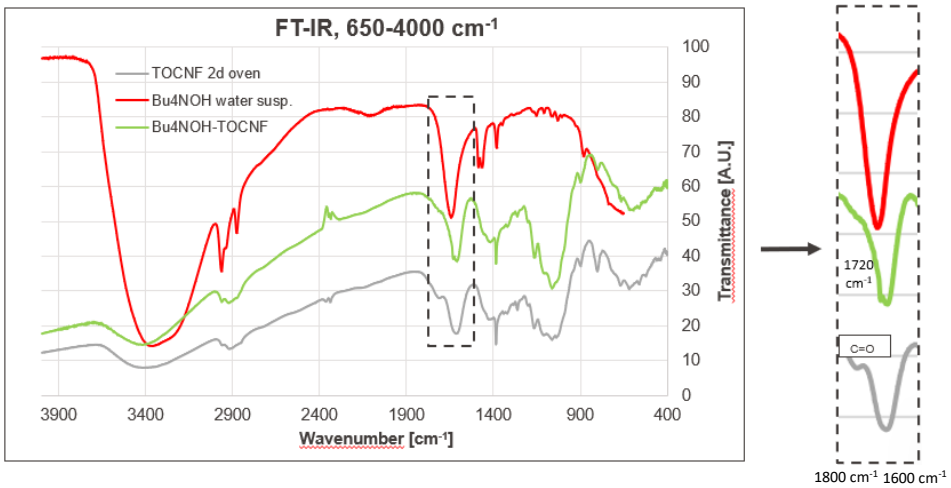

Figura 6- Spettri FT-IR delle TOCNFs essiccate (inserite nella pastiglia di KBr), sospensione acquosa contentente Bu_4NOH (40 wt.%) e TOCNFs modificate con Bu_4NOH essiccate (inserite nella pastiglia di KBr).

Per ulteriori indagini sulla funzionalizzazione delle TOCNFs con Bu_4NOH, sono state eseguite misurazioni del potenziale zeta (Tabella 3).

La diminuzione del modulo del potenziale zeta, in seguito alla modificazione superficiale con Bu_4NOH, indica che le nanofibrille di cellulosa funzionalizzate presentano un minore potere repellente e quindi una minore stabilità in un mezzo acquoso. Al contrario, la dispersione in un mezzo apolare non acquoso, come la resina utilizzata in questo progetto, sarà migliore, giustificando l'utilizzo di questo modificatore per migliorare la compatibilità con la matrice polimerica.

Tabella 3: Risultati delle misurazione del potenziale zeta riguardanti le sospensioni acquose contenenti TOCNFs e Bu_4NOH-TOCNFs (0.1 wt.%).

Materiale	**Mezzo**	**Concentrazione [wt.%]**	**Potenziale zeta [mV]**
TOCNFs	acqua	0.1	-54.5
Bu_4NOH-TOCNFs	acqua	0.1	-39.0

Caratterizzazione della resina tiolo-ene pura e delle resine nanocomposite

Comportamento reologico

Le curve di flusso (Figura 7) mostrano una viscosità più elevata per il TMPTMP, mentre sia il TMPDE che la resina tiolo-ene mpresentano una maggiore fluidità.

Per quanto riguarda le resine nanocomposite, la presenza delle cariche porta a un chiaro aumento della viscosità rispetto alla resina tiolo-ene pura e il comportamento è di shear-thinning. Inoltre, modificando la concentrazione delle TOCNFs da 0.5 a 1 wt.%, la variazione della viscosità è piuttosto bassa a causa del fatto che una minore concentrazione di cariche consente di ottenere una migliore dispersione all'interno della matrice.

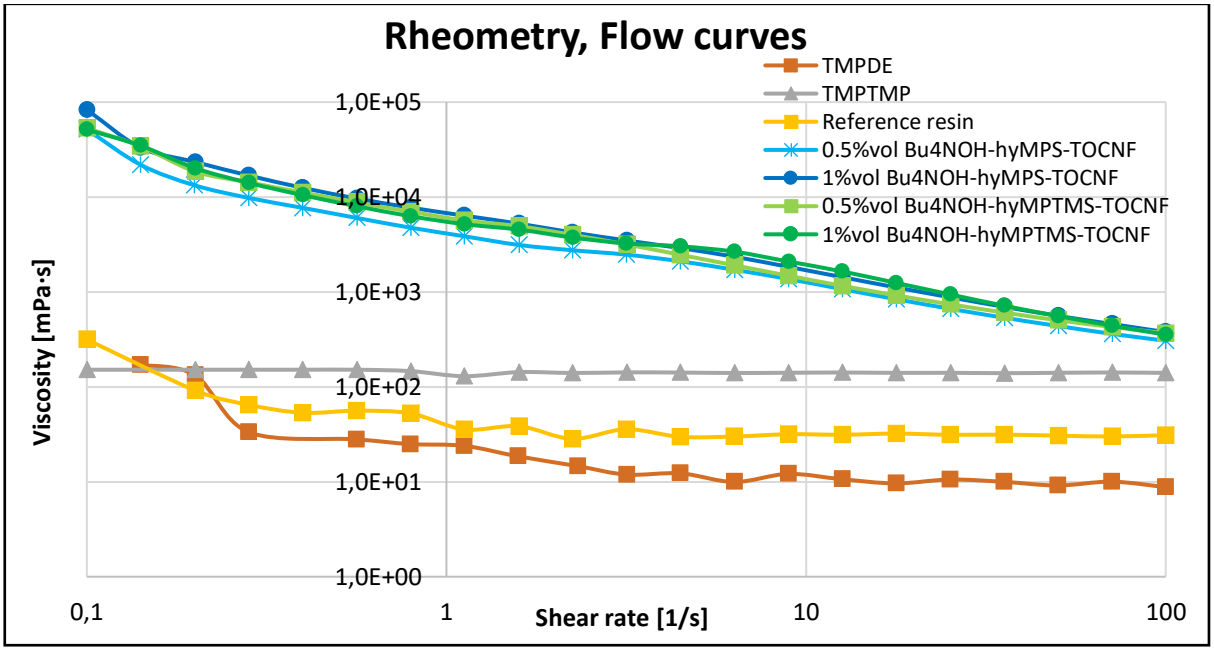

Figura 7- Curve di flusso dei monomeri TMPDE e TMPTMP, della resina tiolo-ene pura e delle resine nanocomposite con diverse composizioni, prima della fotoreticolazione.

La tecnica FT-IR è stata utilizzata per analizzare la reazione tiolo-ene tra TMPDE e TMPTMP, in seguito alla fotoiniziazione eseguita dal DMPA, in particolare analizzando i monomeri e la resina tiolo-ene pura fotoreticolata, focalizzandosi sui gruppi C=C e SH coinvolti nella reazione.

Confrontando gli spettri FT-IR delle diverse specie (Figura 8), è evidente la scomparsa dei gruppi C=C (920, 1600 e 3080 cm^{-1}) e SH (2550 cm^{-1}), presenti nei monomeri, in seguito alla fotoreticolazione UV, a conferma dell'avvenuta reazione.

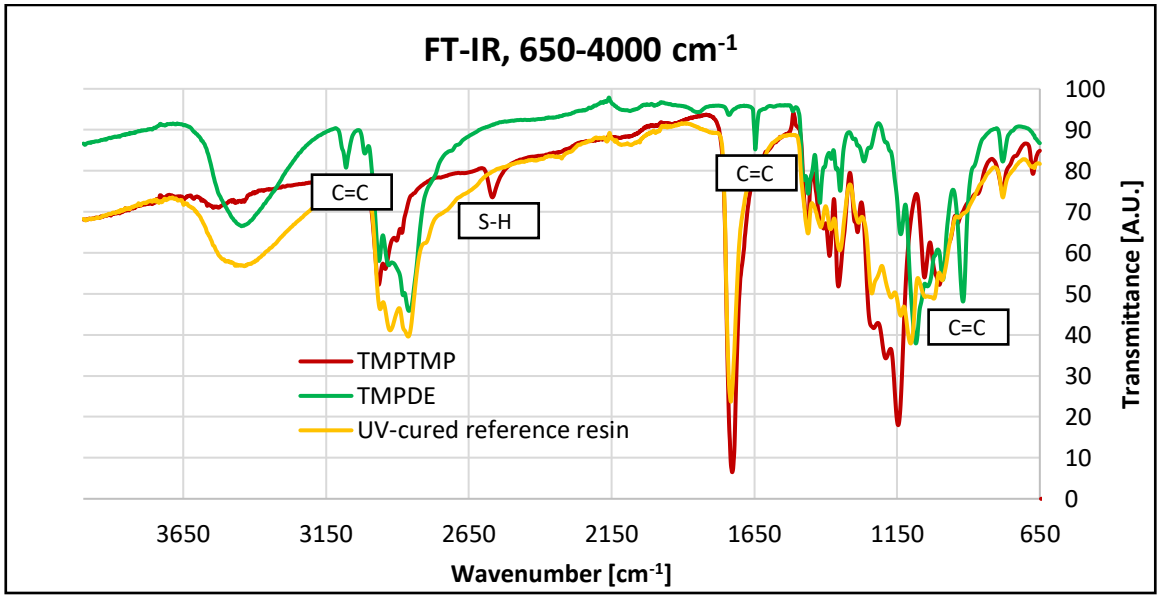

Figura 8- Spettri FT-IR dei monomeri TMPDE e TMPTMP e della resina tiolo-ene fotoreticolata.

In base ai risultati delle misurazioni foto-reologiche (Figura 9), si osserva che l'introduzione di TOCNFs determina una maggiore viscosità iniziale a causa dell'aumento delle interazioni particella-particella e particella-mezzo e della diminuzione della distanza inter-particella, ma, nonostante ciò, tutte le formulazioni nanocomposite sono caratterizzate comunque da una rapida reazione di fotoreticolazione. Infatti, le resine nanocomposite raggiungono il limite superiore di viscosità misurabile dallo strumento in tempi paragonabili a quelli della resina tiolo-ene pura o addirittura più brevi (circa 4-5 s). Al contrario, la resina con 1 vol.% Bu_4NOH-hyMPTMS-TOCNF è caratterizzata da una reazione più lenta.

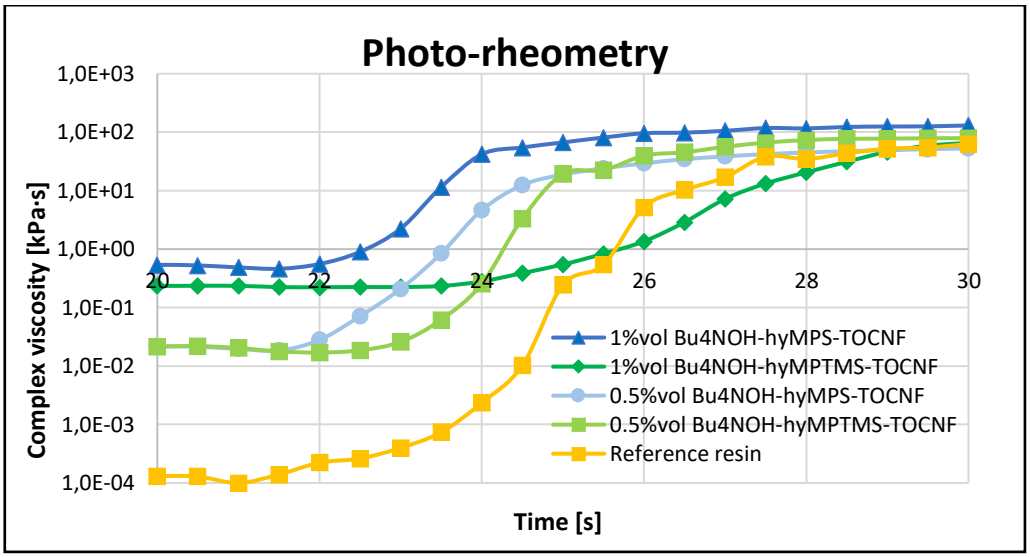

Figura 9- Curve foto-reologiche della resina tiolo-ene pura e delle resine nanocomposite con differenti composizioni, soggette ad una radiazione UV con 5.5 mW/cm² di intensità luminosa al fine di valutare la cinetica della fotoreticolazione.

Analizzando le curve foto-DSC ottenute (Figura 10) e focalizzando l'attenzione sul tempo necessario per raggiungere la cima del picco (Time to peak), sull'area del picco (Peak area) e sul tempo totale necessario per completare la reazione (Total reaction time) (Tabella 4), si osserva che l'aggiunta di TOCNFs funzionalizzate all'interno della resina permette di ottenere una velocità di reazione maggiore rispetto alla resina pura. Anche utilizzando una concentrazione maggiore di TOCNFs, passando da 0.5 a 1 wt.%, e in particolare la resina nanocomposita con 1 vol.% Bu_4NOH-hyMPS-TOCNF presenta la velocità di reazione più elevata.

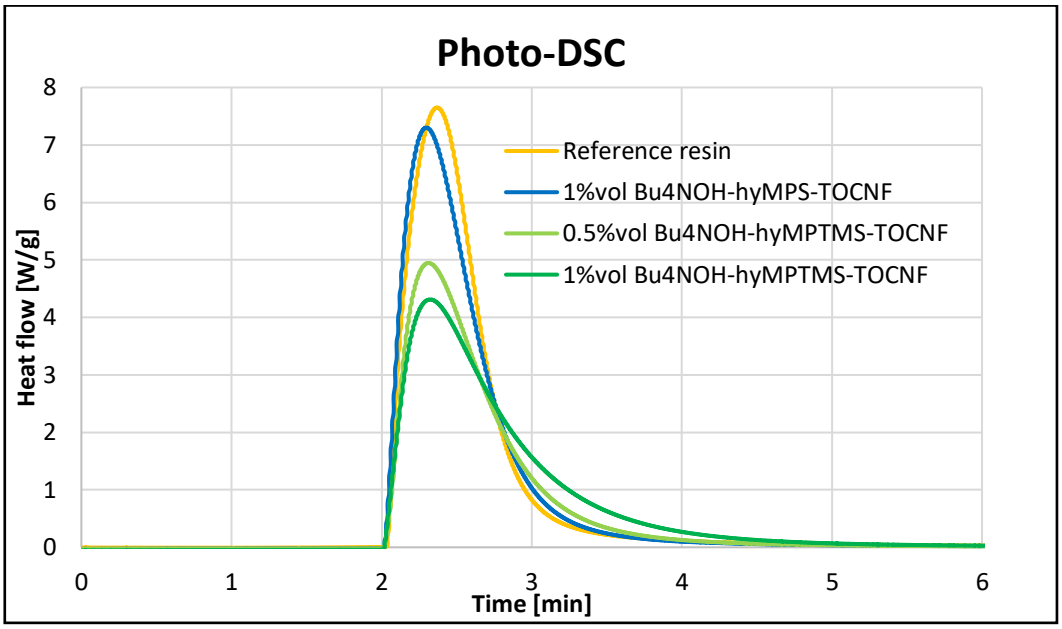

Figura 10- Curve foto-DSC della resina tiolo-ene pura e delle resine nanocomposite con differenti composizioni, soggette da una radiazione UV con 0.5 mW/cm² di intensità luminosa al fine di analizzare la cinetica della fotoreticolazione.

Tabella 4: Parametri relativi all'analisi delle curve foto-DSC.

Materiale	Time to peak [s]	Peak area [J/g]	Total reaction time* [s]	
			0.1 W/g	0.01 W/g
Resina tiolo-ene pura	33	280	247	567
1 vol.% Bu_4NOH-hyMPS-TOCNF	27	278	238	466
0.5 vol.% Bu_4NOH-hyMPTMS-TOCNF	27	226	249	416
1 vol.% Bu_4NOH-hyMPTMS-TOCNF	30	254	281	538

In generale, la reazione di fotoreticolazione è rapida per tutte le formulazioni: occorrono circa 30 s per raggiungere il massimo del picco e circa 4 min per completare la reazione. Tuttavia, confrontando i tempi necessari per raggiungere la fine della reazione, è evidente che la formulazione con 1 vol.% Bu_4NOH-hyMPTMS-TOCNF necessita di un tempo consistentemente più lungo (280 s) rispetto alle altre formulazioni (circa 240 s).

Inoltre, si è notato che l'uso dell'hyMPS come modifica consente di raggiungere una velocità di reazione più elevata rispetto al caso delle TOCNFs modificate con hyMPTMS, nonché una maggiore reattività, dimostrata dall'ottenimento di un'area del picco più estesa. Inoltre, la funzionalizzazione con hyMPTMS determina anche un'area del picco nettamente inferiore e quindi una minore reattività, anche rispetto alla resina tiolo-ene pura.

Caratterizzazione dei film di resina tiolo-ene pura e nanocompositi fotopolimerizzati

Proprietà di trasmissione e trasparenza

Gli spettri UV-Vis (Figura 11) mostrano che è possibile ottenere film nanocompositi trasparenti (circa 85-90% di trasmittanza), paragonabili alla resina tiolo-ene pura, nel caso in cui la concentrazione di TOCNFs sia sufficientemente bassa, in particolare ≤ 5 vol.%. Inoltre, è necessario applicare le modificazioni superficiali alle nanofibrille di cellulosa per permettere di ottenere una buona dispersione delle cariche all'interno della matrice polimerica, mantenendo così le TOCNFs di dimensioni nanometriche e quindi minori rispetto alla lunghezza d'onda della luce visibile.

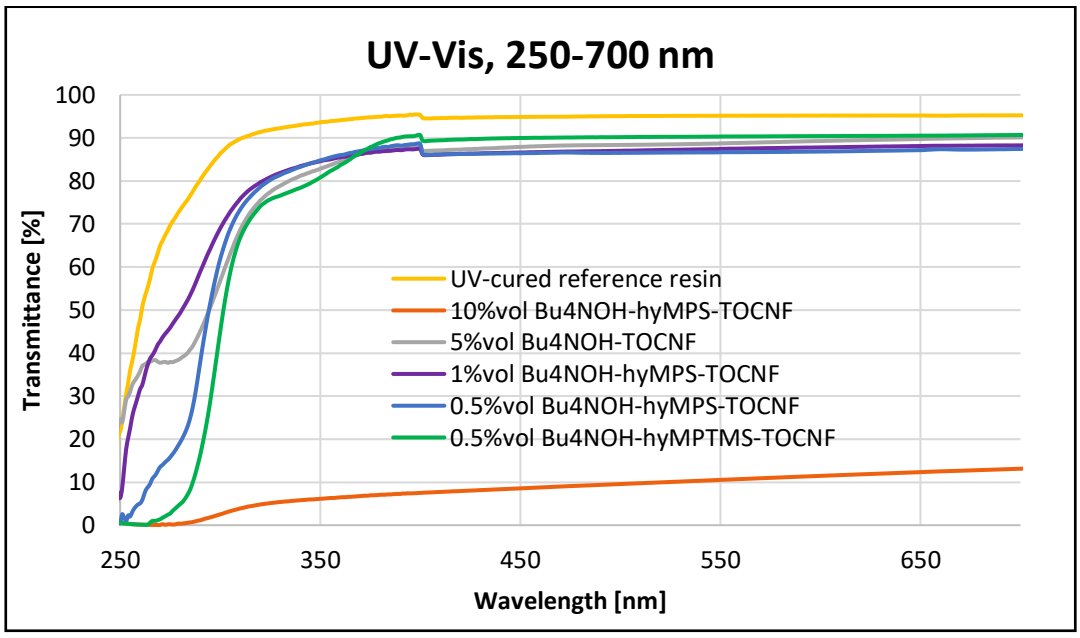

Figura 11- Spettri UV-Vis dei film fotopolimerizzati di resina tiolo-ene pura e nanocompositi con composizioni diverse.

Stabilità termica

Le curve TGA risultanti (Figura 12) hanno mostrato che la resina tiolo-ene pura polimerizzata ha una maggiore stabilità termica (T_{onset} ≈ 350 °C) rispetto alle TOCNFs (T_{onset} ≈ 215 °C) e il processo di degradazione è diverso anche in termini di numero di fasi di degradazione. Infatti, le nanofibrille di cellulosa sono caratterizzate da 3 fasi di degradazione, mentre la resina presenta una sola fase, come mostrato anche dalle curve DTGA. Infine, la stabilità termica del film nanocomposito fotopolimerizzato non è influenzata dalla presenza delle TOCNFs, mantenendo una T_{onset} paragonabile a quello della resina tiolo-ene pura (circa 340 °C), nonché un processo di degradazione termica simile caratterizzato da un singolo step.

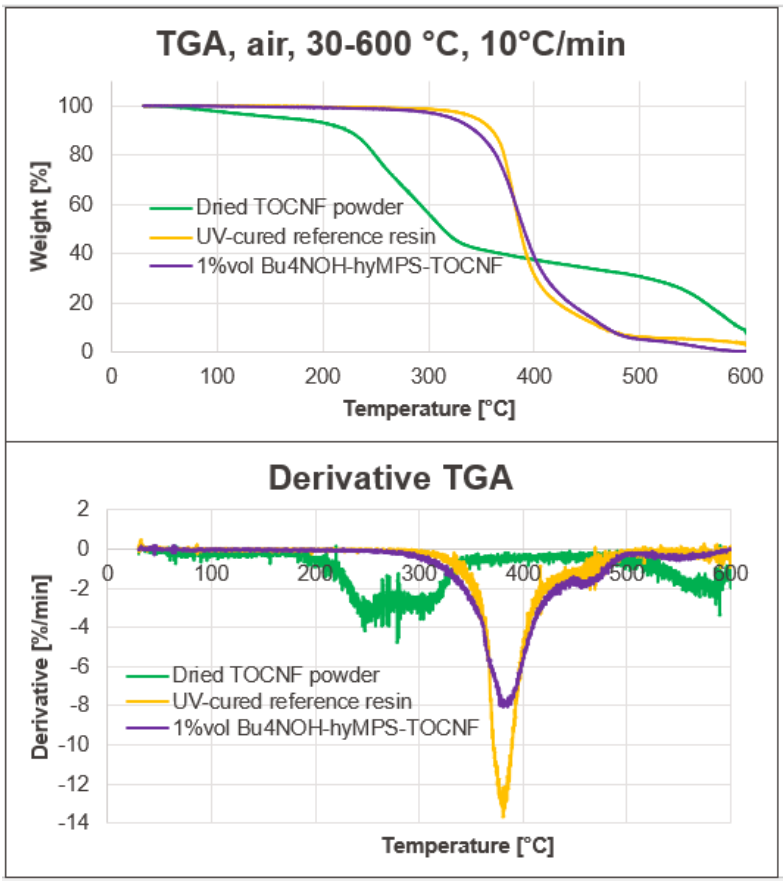

Figura 12- Curve TGA e DTGA delle TOCNFs essiccate e dei film fotopolimerizzati di resina tiolo-ene pura e nanocomposito con 1 vol.% Bu_4NOH-hyMPS-TOCNF, analizzati in aria tra 30 °C e 600 °C con una rampa di temperatura di 10 °C/min.

Proprietà superficiali

Confrontando i risultati ottenuti dai test di nanoindentazione (Tabella 5, Figura 13), risulta evidente che l'aggiunta di TOCNFs permette di raggiungere valori di modulo ridotto (R.M.) e durezza superficiale (S.H.) molto più elevati rispetto alla resina pura, soprattutto se si utilizzano alte

concentrazioni di nanofibrille di cellulosa e hyMPTMS come modificatore. È addirittura possibile ottenere valori di R.M. 6 volte superiori e di S.H. 3 volte superiori rispetto alla resina nel caso in cui si utilizzi il 10 vol.% di TOCNFs funzionalizzate.

A basse concentrazioni di TOCNFs, la modificazione superficiale con hyMPTMS ha permesso di ottenere proprietà meccaniche migliori rispetto all'utilizzo di hyMPS; ciò potrebbe essere legato alla maggiore reattività dei tioli che, essendo presenti anche come funzionalità sulle nanofibrille di cellulosa, potrebbero aver generate un network più fittamente connesso tra particelle e matrice. Al contrario, nel caso dell'hyMPS, i gruppi C=C, presenti sulla superficie delle TOCNFs, sono meno reattivi e questo potrebbe aver portato alla formazione di un network meno denso intorno alle particelle.

Tabella 5: Modulo ridotto e durezza superficiale misurati tramite test di nanoindentazione, con relativa variazione percentuale rispetto alla resina tiolo-ene pura utilizzata come riferimento.

Materiale	**Modulo Ridotto [MPa]**	**Durezza Superficiale [MPa]**	**R.M. increase [%]**	**S.H. increase [%]**
Resina pura	11.1	2.3	riferimento	riferimento
10%vol Bu_4NOH-hyMPS-TOCNF	78.5	10.1	606	346
5%vol Bu_4NOH-hyMPS-TOCNF	34.8	4.5	213	98
1%vol Bu_4NOH-hyMPS-TOCNF	13.3	2.5	19	10
1%vol Bu_4NOH-hyMPTMS-TOCNF	15.5	3.5	39	53
0.5%vol Bu_4NOH-hyMPS-TOCNF	9.6	2.2	-13	-4
0.5%vol Bu_4NOH-hyMPTMS-TOCNF	12.9	3.1	16	35

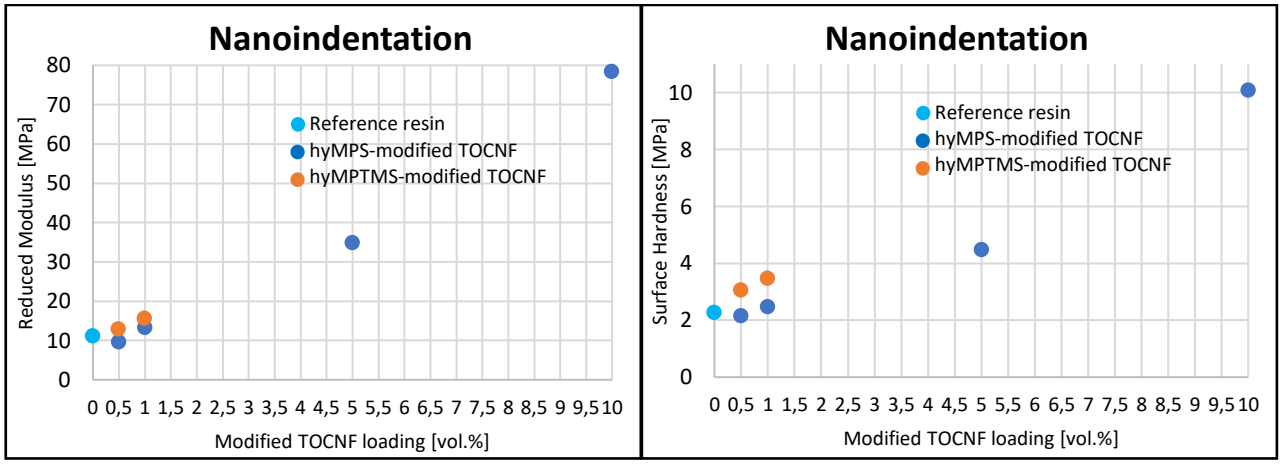

Figura 13- Grafici che mostrano l'andamento del modulo ridotto e della durezza superficiale, misurati tramite test di nanoindentazione, dei film fotopolimerizzati di resina tiolo-ene e nanocomposite con composizioni diverse, in funzione della concentrazione di TOCNFs funzionalizzate impiegata.

Osservando le immagini ottenute con lo strumento di nanoindentazione (Figura 14), è evidente che, al diminuire della concentrazione di TOCNFs, la rugosità superficiale si riduce consistentemente.

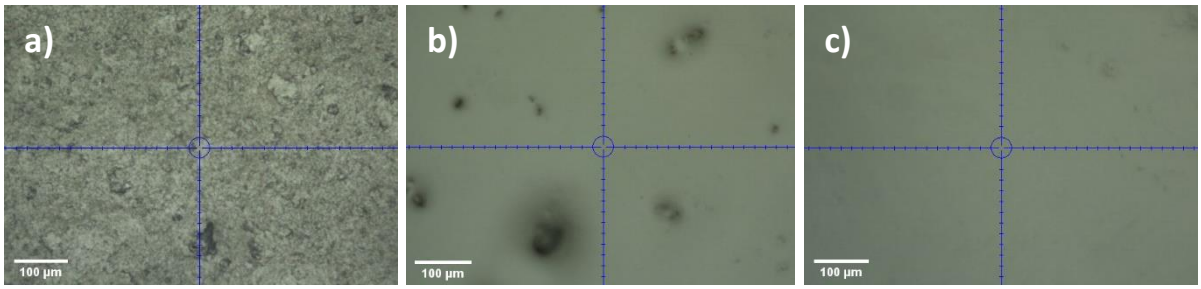

Figura 14- Immagini ottenute tramite lo strumento di nanoindentazione che mostrano la rugosità superficiale dei film fotopolimerizzati nanocompositi contenenti: a) 10%vol Bu_4NOH-hyMPS-TOCNF, b) 5%vol Bu_4NOH-hyMPS-TOCNF and c) 1%vol Bu_4NOH-hyMPS-TOCNF.

In base ai risultati delle misurazioni dell'angolo di contatto (Tabella 6), si osserva che la resina tiolo-ene è leggermente idrofobica (78° water contact angle "WCA"), mentre l'introduzione di nanofibrille di cellulosa funzionalizzate permette di ottenere una maggiore idrofobicità (circa 85-90° WCA) grazie sia all'aumento della rugosità superficiale sia all'incremento della frazione non polare, legato all'applicazione dei modificatori superficiali come Bu_4NOH e hyMPS o hyMPTMS.

Tabella 6: Risultati dei test di angoli di contatto con diversi liquidi, i valori mostrati sono stati calcolati tramite la media di 3 valori.

Materiale	Acqua [°]	Glicole Etilenico [°]	Diiodometano [°]
Resina pura	78.1	50.3	42.3
0.5%vol Bu_4NOH-hyMPS-TOCNF	87.6	49.7	35.1
0.5%vol Bu_4NOH-hyMPTMS-TOCNF	86.6	55.6	26.6
1%vol Bu_4NOH-hyMPS-TOCNF	83.8	53.7	23.1
1%vol Bu_4NOH-hyMPTMS-TOCNF	89.5	59.8	29.9

La replicazione della superficie nanostrutturata della foglia di loto, con la tecnica UV-NIL, ha permesso di produrre rivestimenti super-idrofobici caratterizzati da valori di WCA molto elevati (Tabella 7); il valore massimo di WCA raggiunto è 155° (Figura 15), un valore eccezionale se si considera che la natura originale della cellulosa è idrofila e non sono stati utilizzati tensioattivi.

Tabella 7: Risultati dei test di angolo di contatti con l'acqua, che mostrano il valore medio (basato su 5 misurazioni) e il valore massimo di WCA.

Materiale	WCA medio [°]	WCA max [°]
Resina pura	132	147
0.5%vol Bu_4NOH-hyMPS-TOCNF	142	155
0.5%vol Bu_4NOH-hyMPTMS-TOCNF	136	150

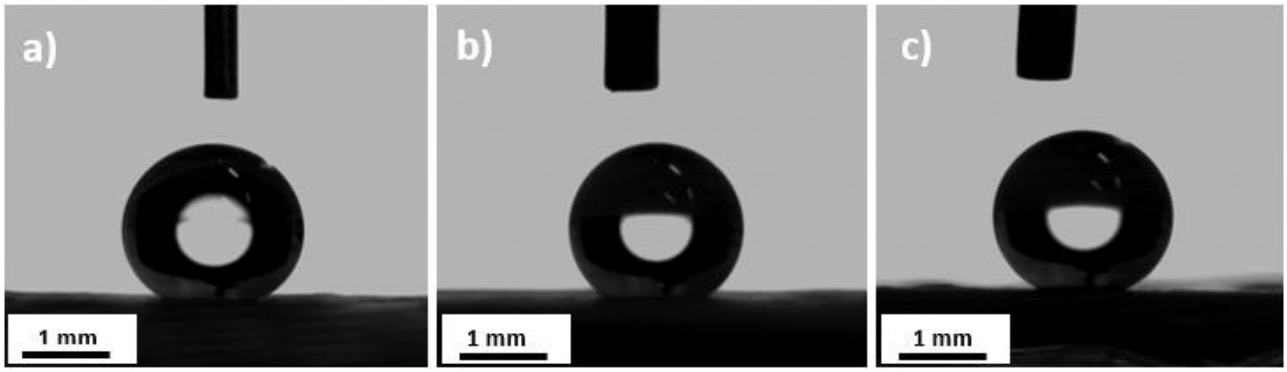

Figura 15- Immagini raffiguranti la morfologia delle gocce d'acqua (8 µL) sulla superficie dei film patternati di: a) resina pura (147° WCA), b) 0.5% vol Bu_4NOH-hyMPTMS-TOCNF (150° WCA) e c) 0.5% vol Bu_4NOH-hyMPS-TOCNF (155° WCA).

Inoltre, tramite il test con i granelli di pepe, è stata dimostrata la capacità autopulente dei film nanocompositi patternati. In particolare, inclinando il film di 25°, è stato possibile pulire la superficie con gocce d'acqua (Figura 16). L'angolo di scorrimento dipende molto dal materiale utilizzato, nel nostro caso non era funzionalizzato con fluoro, che viene spesso utilizzato per aumentare l'idrofobicità e le proprietà autopulenti a causa della sua migrazione e accumulo sulla superficie, quindi il risultato è comunque impressionante.

I grani di pepe sono caratterizzati da una natura idrofobica, quindi aderiscono fortemente al film super-idrofobico. Tuttavia, grazie al patterning a livello nanometrico, l'area di contatto tra le particelle e la superficie è molto ridotta e quindi le gocce d'acqua sono comunque in grado di catturare i contaminanti idrofobici mentre scivolano.

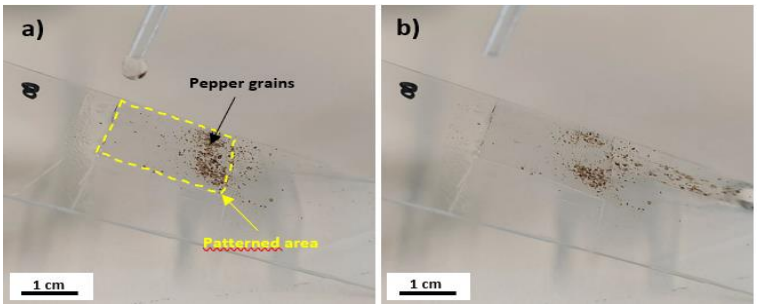

Figura 16- Immagini che mostrano la proprietà di self-cleaning del film nanocomposito patternato con 0.5%vol Bu_4NOH-hyMPS-TOCNF, contaminato da granelli di pepe: a) prima della pulizia, b) dopo la pulizia, dovuta al passaggio delle gocce d'acqua che sono state in grado di catturare i contaminanti durante lo scorrimento, lasciando una chiara traccia di pulizia.

Come mostrato dalle immagini SEM (Figura 17), il template in PDMS prodotto è in grado di imitare la superficie rugosa micro- e nano-strutturata della foglia di loto, sotto forma di replica negativa.

Per quanto riguarda il film patternato di resina pura, la replica in positivo della superficie del loto non è completamente riuscita, poiché sono state copiate le micropapille ma non i nanopillar nella parte superiore; inoltre, la morfologia è caratterizzata anche da regioni piatte e, di conseguenza, la superficie rugosa della foglia di loto non risulta imitata in modo ottimale.

Al contrario, il film nanocomposito patternato, con 0.5%vol di Bu_4NOH-hyMPS-TOCNF, mostra una replicazione ottimale di micropapille, nanopillar e superficie rugosa, che permette di ottenere proprietà super-idrofobiche ancora maggiori, in accordo con i risultati delle misurazioni dei WCA.

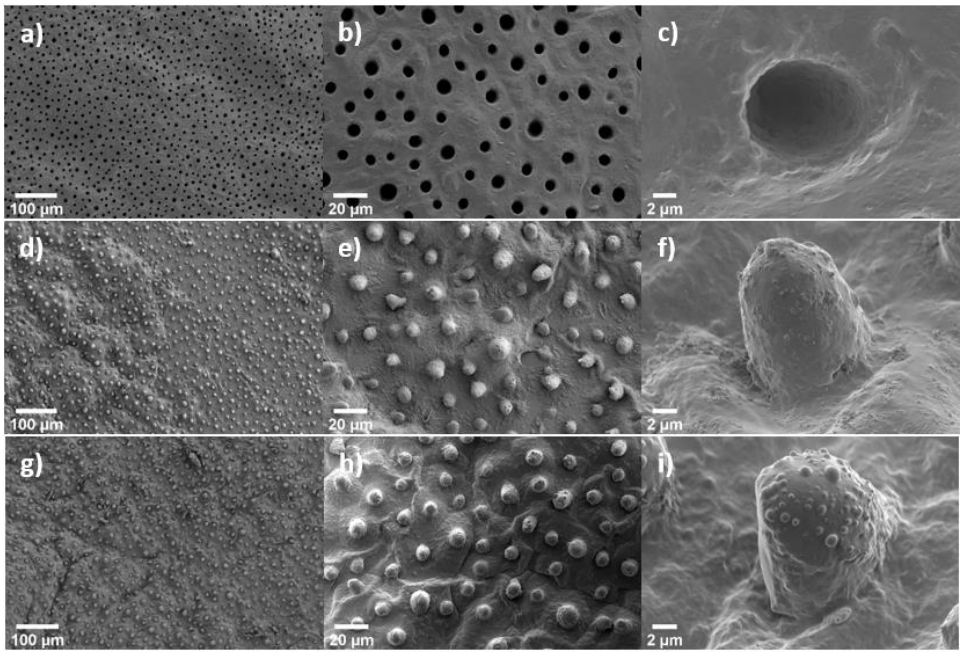

Figura 17- Immagini SEM prodotte a 3 differenti ingrandimenti (150x, 600x e 4000x rispettivamente) del template in negativo in PDMS della superficie della foglia di loto (a-c), film patternato in resina pura (d-f) e del film nanocmposito patternato (con 0.5%vol Bu_4NOH-hyMPS-TOCNF).

Conclusioni

L'obiettivo principale di questa tesi era il processing di una resina tiolo-ene foto-polimerizzabile tramite luce UV, con l'aggiunta di nanofibrille di cellulosa come filler, per produrre un film nanocomposito.

L'utilizzo della cellulosa, un materiale bio-based ottenibile da numerose fonti naturali, ha permesso di migliorare le basse prestazioni meccaniche della matrice polimerica, oltre a ottenere proprietà superficiali notevoli.

La possibilità di sfruttare la chimica delle reazioni tiolo-ene, definita “click”, e la fotoreticolazione UV ha consentito una lavorazione molto rapida e semplice, senza inibizione da parte dell'ossigeno, come dimostrato dalle analisi foto-reologia e foto-calorimetria a scansione differenziale (foto-DSC).

Attraverso la sperimentazione di diversi step di lavorazione alternativi, è stato possibile determinare un metodo ottimizzato; l'obiettivo di preparare una resina composita processabile, sufficientemente fluida e caratterizzata da una buona dispersione delle nanocariche, è stato raggiunto. Inoltre, i materiali costituenti della resina sono ridotti al minimo, poiché non vengono utilizzati tensioattivi, disperdenti o solventi reattivi.

Grazie all'efficacia delle modificazioni superficiali applicate alle TOCNFs, una migliore compatibilità e un'eccellente dispersione delle fibrille nella resina sono stati ottenuti. Ciò ha permesso di sfruttare efficacemente il rinforzo dato dalle nanoparticelle, mantenendo la trasparenza tipica della matrice tiolo-ene, come dimostrato rispettivamente dalle analisi di nanoindentazione e di spettroscopia UV-Vis.

Mediante l'analisi termogravimetrica (TGA), si è dimostrato che la stabilità termica del composito rimane pressoché invariata rispetto a quella del polimero puro, anche se le TOCNFs sono caratterizzate da una minore temperatura di degradazione termica.

Basandosi sulle proprietà superficiali e di bagnabilità dei film prodotti, è stata proposta un'applicazione dimostrativa che sfrutta l'imitazione della superficie gerarchica di una foglia di loto per ottenere un comportamento super-idrofobico, utilizzando la tecnica di UV nanoimprint lithography (UV-NIL).

Nonostante la natura idrofila della cellulosa, l'applicazione di funzionalizzazioni superficiali, atte a migliorare la compatibilità con la matrice non polare, e l'aumento della rugosità superficiale, hanno

permesso di aumentare l'idrofobicità del materiale. Come evidenziato dall'analisi di microscopia elettronica a scansione (SEM) e dalle misurazioni dell'angolo di contatto con l'acqua (WCA), è stato possibile produrre un film nanocomposito trasparente, micro- e nano-strutturato, super-idrofobico con proprietà meccaniche migliorate e capacità autopulente, che potrebbe risultare promettente in vari campi applicativi in cui vengono utilizzati rivestimenti protettivi. Inoltre, è stato osservato che l'aggiunta di nanofibrille di cellulosa ha permesso di replicare con maggiore precisione la forma della struttura gerarchica, probabilmente grazie alle migliori proprietà meccaniche.

Grazie alle promettenti caratteristiche dei film nanocompositi ottenuti, risulterebbe interessante implementare la caratterizzazione delle proprietà di resistenza all'usura, essenziali in caso di utilizzo come rivestimento protettivo.

Un'ulteriore prospettiva futura può basarsi sulla comprovata processabilità attraverso l'UV-NIL, come dimostrato da questo progetto, delle resine a base tiolo-ene, da sfruttare per la produzione di film nanopatternati caratterizzati anche da capacità di memoria di forma, come recentemente dimostrato da Zhang X. et al. [70].

List of Abbreviations

BC bacterial cellulose

BHT butylated hydroxytoluene

Bu_4NOH tetrabutylammonium hydroxide

CNC cellulose nanocrystals

CNF cellulose nanofibrils

DMF N,N-dimethylformamide

DMPA 2,2-dimethoxy-2-phenylacetophenone

DSC differential scanning calorimetry

DTGA derivative TGA

ECNF electrospun cellulose nanofibers

Ethanol EtOH

FT-IR Fourier transform-infrared spectroscopy

HBP hyperbranched polyester

hyMPS hydrolyzed MPS

hyMPTMS hydrolyzed MPTMS

MEMS/NEMS micro/nano-electro-mechanical systems

MFC microfibrillated cellulose

MPS 3-(methacryloyloxy) propyltrimethoxysilane

MPTMS 3-(mercaptopropyl) trimethoxysilane

NFC nanofibrillated cellulose

NP nanoparticle

PDMS polydimethylsiloxane

PFPE perfluoropolyether

PFUA perfluoropolyether-urethane acrylate

PMMA poly(methyl methacrylate)

PVDF polyvinylidene fluoride

R.M. reduced modulus

S.H. surface hardness

SEM scanning electron microscopy

T temperature

TEM transmission electron microscopy

TEMPO 2,2,6,6-tetramethylpiperidine-N-oxyl

TGA thermogravimetric analysis

TMPDE trimethylolpropane diallyl ether

TMPTMP trimethylolpropane tris (3-mercaptopropionate)

TOCNF TEMPO-oxidized cellulose nanofibrils

T_{onset} onset temperature

UV ultraviolet

UV-NIL UV nanoimprint lithography

UV-Vis ultraviolet-visible light spectroscopy

vol.% or %vol volume percentage

WCA water contact angle

wt.% or %wt weight percentage

List of Figures

Figure 1- Schematic illustration of the photoinitiated free radical polymerization of a common ene monomer M [1].

Figure 2- Schematic illustration of different types of click reactions [6].

Figure 3- Schematic illustration of an idealized reaction between thiol and ene [5].

Figure 4- Illustrations of common a) alkyl thiols and (b) multifunctional thiols used in thiol–ene polymerization processes [5].

Figure 5- Illustrations of typical multifunctional enes used in thiol–ene polymerization processes [5].

Figure 6- Illustration of the molecular structure of cellulose polymer [19].

Figure 7- Illustration of the hierarchical structure of wood, showing: the middle lamella (ML), the primary wall (P), the outer (S1), middle (S2) and inner (S3) layers of secondary wall, the wartylayer (W), cellulose (C), hemicellulose (H), lignin (L), microfibril (MF), elementary fibril (EF), crystalline domain (Cr) and amorphous domain (Am) [19].

Figure 8- High-resolution transmission electron microscopy (TEM) images of (a) CNCs and (b) CNFs [24].

Figure 9- Supermass colloider grinder used in mechanical processes to produce CNFs [19].

Figure 10- Schematic representation of the regioselective TEMPO oxidation of cellulose alcohol groups using TEMPO/NaBr/NaClO in water at basic pH [26].

Figure 11- TEM images of dried dispersions of TEMPO-oxidized hardwood celluloses with carboxylate contents of 1.0 and 1.5 mmol g-1, observed by negative staining with uranyl acetate. The insets show the corresponding aqueous dispersions, showing the difference in transparency [26].

Figure 12- Visual appearance of TEMPO-oxidized CNF aqueous suspension at 1 wt.% (in Petri dishes, top view) [19].

Figure 13- TEM images showing nanoparticles, nanofibers and nanoclays appearances [29].

Figure 14- Schematic images representing different types of nanoclays dispersion [36].

Figure 15- Grafical abstract representing some application fields of nanocellulosic materials, e.g. celllulose nanofibrils (CNFs), cellulose nanocrystals (CNCs) and bacterial cellulose (BC) [48].

Figure 16- Schematic representation of UV-NIL process on a thiol-ene system [57].

Figure 17- Scanning electron microscopy (SEM) images of UV-NIL nanostructured patterns [57].

Figure 18- Schematic representation of general cases of wetting behaviour: super-hydrophobic, hydrophobic, hydrophilic, super-hydrophilic [67].

Figure 19- Schematic representation of lotus leaves and rose petals wetting behaviour [61].

Figure 20- SEM image of lotus leaves nano-structure with nano-pillars [60].

Figure 21- SEM images of rose petal micro- and nano-structure with micro-papillae and nano-folds [68].

Figure 22- Rose petal static water contact angle (WCA) and upside-down behaviour [68].

Figure 23- Schematic representation of the change in the molecular structure due to the hydrolysis step of MPS; specifically, CH_3 groups are replaced by OH groups.

Figure 24- Schematic representation of the change in the molecular structure due to the hydrolysis step of MPTMS; specifically, CH_3 groups are replaced by OH groups.

Figure 25- TMPDE molecular structure.

Figure 26- TMPTMP molecular structure.

Figure 27- Silicone mold with glass slide substrates used to produce films by casting followed by UV curing.

Figure 28- Transparency of the nanocomposite resin, thanks to well dispersed modified CNFs.

Figure 29- TGA and derivative TGA (DTGA) curve of dried TOCNF powder tested in air between 30-600 °C with a constant rate of 10 °C /min.

Figure 30- FT-IR spectra of dried TOCNFs (inside KBr disk), pure hydrolyzed MPS and dried hyMPS modified TOCNFs (inside KBr disk); both dried TOCNFs and hyMPS-TOCNFs samples were subjected to a drying step of 2 days in oven at 120 °C to ensure a reduction in residual humidity.

Figure 31- FT-IR spectra of dried TOCNFs (inside KBr disk), pure hydrolyzed MPTMS and dried hyMPTMS modified TOCNFs (inside KBr disk); both dried TOCNFs and hyMPTMS-TOCNFs samples were subjected to a drying step of 2 days in oven at 120 °C to ensure a reduction in residual humidity.

Figure 32- FT-IR spectra of dried TOCNFs (inside KBr disk), Bu_4NOH water suspension (40wt.%) and dried Bu_4NOH modified TOCNFs (inside KBr disk); both dried TOCNFs and Bu_4NOH-TOCNFs samples were subjected to a drying step of 2 days in oven at 120 °C to ensure a reduction in residual humidity.

Figure 33- Flow curves of TMPDE and TMPTMP monomers, reference resin and nanocomposite resins with different compositions before UV-curing step.

Figure 34- FT-IR spectra of TMPDE, TMPTMP and UV-cured reference resin.

Figure 35- Photo-rheometry curves of reference resin and nanocomposite resins with different compositions, subjected to 5.5 mW/cm^2 light intensity to analyse the photo-crosslinking kinetics.

Figure 36- Photo-DSC curves of reference resin and nanocomposite resins with different compositions, subjected to 0.5 mW/cm^2 light intensity to analyse the photo-crosslinking kinetics.

Figure 37- UV-Vis spectra of UV-cured nanocomposite films with different compositions compared to UV-cured reference resin film.

Figure 38- Transparency of UV-cured nanocomposite films with 1%vol Bu4NOH-hyMPS-TOCNF.

Figure 39- TGA and derivative TGA (DTGA) curves of UV-cured reference resin, dried TOCNF powder and UV-cured nanocomposite film with 1 vol.% of Bu_4NOH-hyMPS-TOCNF tested in air between 30-600 °C with a constant rate of 10 °C /min.

Figure 40- Graphs showing the behaviour of the reduced modulus and surface hardness of cured films of reference resin and nanocomposite resins as a function of the concentration of modified TOCNF used; results obtained through nanoindentation tests.

Figure 41- Nanoindentation images showing the surface roughness of cured nanocomposite films containing a) 10%vol Bu4NOH-hyMPS-TOCNF, b) 5%vol Bu4NOH-hyMPS-TOCNF and c) 1%vol Bu4NOH-hyMPS-TOCNF.

Figure 42- Picture showing the morphology of the 8 µL water drop on the surface of a) reference resin (with 147 ° WCA), b) 0.5% vol Bu_4NOH-hyMPTMS-TOCNF (with 150° WCA) and c) 0.5% vol Bu_4NOH-hyMPS-TOCNF (with 155° WCA), lotus leaf nano-patterned film.

Figure 43- Pictures showing the behaviour of lotus leaf nano-patterned composite film (0.5%vol Bu4NOH-hyMPS-TOCNF) contaminated by pepper grains on the surface: a) before water cleaning, b) after cleaning, water droplets captured pepper grains while sliding and a clean trace has been left on the imprinted surface.

Figure 44- SEM images at 3 different magnifications (150X, 600X and 4000X respectively) of PDMS negative replica of lotus leaf hierarchical surface (a-c), UV-NIL imprinted reference resin film (d-f) and UV-NIL imprinted 0.5%vol Bu_4NOH-hyMPS-TOCNF nanocomposite resin film.

Figure 45- SEM image of PDMS mold surface after UV-NIL imprinting of 1%vol Bu_4NOH-hyMPS-TOCNF nanocomposite resin, showing the residues of the imprinted cured film remaining on the PDMS surface following peeling off.

List of Tables

Table I: *Chosen materials for resin preparation.*

Table II: *Classification of nanocomposite resin formulations.*

Table III: *Nanocomposite resin processing routes.*

Table IV: *List of quantities used in the preparation of formulations.*

Table V: *Procedures used for spin coating multiple resin types.*

Table VI: *Surface energy contributions of different liquids used in contact angle measurements.*

Table VII: *Zeta-potential measurements results concerning TOCNFs and Bu_4NOH-TOCNFs water suspensions (0.1 wt.%).*

Table VIII: *Photo-DSC parameters obtained from the analysis of the photo-DSC curves of reference resin and nanocomposite resins with different compositions.*

Table IX: *Reduced modulus and surface hardness of the reference resin and nanocomposite cured films, measured by means of nanoindentation tests, with relative percentage variations in properties compared to the reference resin.*

Table X: *Contact angle measurements results, displaying average contact angle values calculated between 5 values.*

1. Introduction

1.1 Motivation

Thiol-ene “click” chemistry appears to be very attractive as it enables rapid photo-polymerization reactions insensitive to oxygen presence and without side products generation, by irradiation with UV radiation [5]. Despite this, thiol-ene polymers are characterized by very low mechanical properties [5], therefore an efficient solution can be the incorporation of fillers in order to strengthen them. For this purpose, cellulose nanofibrils (CNFs), a bio-based material obtainable from numerous natural resources, were chosen to produce the composites.

Due to their hydrophilic nature [19], also enhanced by the TEMPO-oxidation [26] they undergo to increase their dispersion in an aqueous medium, it is complicated to incorporate them into an organic medium such as a polymer resin. To solve this issue, surface modifications can be applied to TEMPO-oxidized CNFs (TOCNFs) in order to improve their compatibility with the matrix.

Furthermore, in this project it is fundamental, for the UV processability, to maintain the characteristic transparency of the chosen thiol-ene system [5], thus optimizing the processing and performing specific steps to increase the filler dispersion are essential. In addition, this approach also makes it possible to efficiently exploit the reinforcement associated with the incorporation of nanofillers, which are characterized by a very high specific surface area when well-dispersed [45].

1.2. Research Objectives

The primary aim of this thesis project is to investigate the processability of cellulose nanofibrils (CNFs) as fillers within a UV-curable thiol-ene system, in order to produce nanocomposite materials.

In particular, it is essential to achieve a good dispersion of the nanofillers with the aim of maximising their effectiveness in enhancing the matrix properties. In order to achieve this goal, different approaches have been proposed, including surface modifications of the cellulose nanofibrils to increase their compatibility with the polymer and optimization of processing steps.

The curing behaviour and other relevant resin processing parameters, such as viscosity, have been evaluated to assess the influence of the modified CNFs presence.

A complete characterization was performed on both the raw materials and the nanocomposite films produced with different filler concentrations, by focusing on mechanical, optical and surface properties.

In order to demonstrate the usefulness of this research, conceptual application was proposed. Specifically, UV nanoimprint lithography (UV-NIL) technique was used to replicate bio-inspired micro-nano-sized hierarchical structures, with the purpose of obtaining transparent super-hydrophobic surfaces with enhanced mechanical properties.

1.3 Structure of the Thesis

The thesis is divided into five chapters, with the remaining four being organized in the following order: State of the Art, Materials and Method, Results and Discussion, Conclusions.

Chapter 2 presents the state of the art with regard to the scientific fields related to the research area. Topics such as photo-polymerization, “click” and thiol-ene reactions, cellulose and cellulose nanofibrils, nanocomposites and bio-inspired surface replication has been presented to provide an overview of the challenges related to this work.

Chapter 3 describes in detail the synthesis and characterization methods used during materials processing. Specifically, the species used to produce the resins, the preparation of the TOCNF surface modifiers, the manufacture of the composite films, the procedure to generate replicas of the hierarchical lotus leaf surface and characterization methods, were explained.

Chapter 4 shows the results obtained and offers a critical commentary, as well as a discussion based on personal reasoning and hypotheses. In particular, the focus was both on optimising the processing steps and on analyzing the material properties of resins, modified TOCNFs and UV-cured composite films.

Finally, Chapter 5 summarises the main outcomes and achievements, as well as providing ideas and suggestions for possible future research.

2. State of the Art

2.1. Photopolymerization

2.1.1. Definition

The process of photopolymerization refers to the synthesis of insoluble polymers by reactions that are initiated upon the absorption of light by a polymerizable starting system [1].

In particular, light acts only as an initiating tool, it does not influence the other reaction steps like propagation and termination stages of the chain process.

2.1.2. UV Light Photoinitiation

Usually a very small amount (less than 2 wt.%) of photoinitiators is added to formulations to be polymerized [2]. Photoinitiators are compounds that are thermally stable at reaction conditions and capable to decompose by absorbing light in different wavelength ranges, in order to generate active species that can initiate the polymerization.

Generally, UV light is the most common photo-initiating source because, compared to visible light, it has the advantage of using a colorless photoinitiator, but raises concerns regarding the protection to the user because of exposure possibility to UV rays can cause premature aging of the skin and signs of sun damage, eye problems and also weaken the immune system [3].

In conclusion, photopolymerization, especially upon UV-irradiation, presents distinguishable advantages, such as rapid drying, solventless formulations, and reduced energy consumption and it can easily be performed without expensive equipment or special skills [2].

As compared with the thermal polymerization techniques, photopolymerization is generally initiated and conducted at lower temperatures, which reduces the overall energy consumption.

In many cases, photoinitiation can replace other initiation techniques, including thermochemical or electrochemical initiation [1], and this is one of the reasons why it is also widely used in industrial processes.

2.1.3. Photopolymerization Mechanisms

Both radical and ionic chain polymerizations can be photoinitiated, provided that appropriate initiators and monomers are employed [1].

2.1.3.1. Free Radical Photopolymerization

The synthesis of polymers by the radical polymerization of monomers starts with the generation of free radicals, which is properly executed through photoreactions of initiator molecules. The subsequent processes, i.e. propagation, including chain transfer, and termination, are thermal reactions, which are not affected by light (Figure 1).

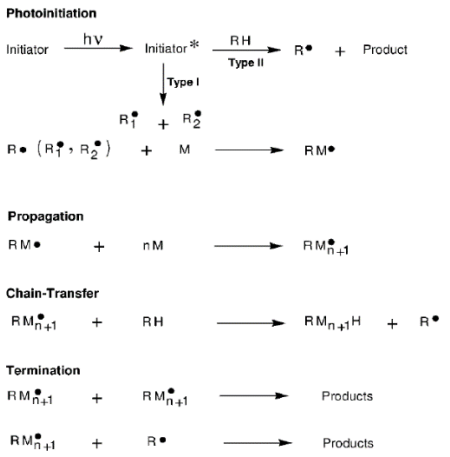

Figure 1- Schematic illustration of the photoinitiated free radical polymerization of a common ene monomer M [1].

Two types of compounds are employed as photoinitiators of free radical polymerizations, which differ in their mode of action of generating reactive free radicals [1]. Type I initiators, after photon absorption, go through a very rapid bond cleavage. On the contrary, type II initiators generate relatively long-lived excited triplet states that undergo reactions such as electron-transfer or hydrogen-abstraction with co-initiator molecules that are purposely added to the monomer-containing system.

Typical radical-based photopolymerization, involving for example acrylates and methacrylates, offers both spatial and temporal control through a chain-growth mechanism; these features make this type of polymerization optimal for a wide range of applications, including coatings, dental materials, contact lenses and photolithographic processes.

Unfortunately, classical photopolymerization reactions suffer several critical problems, such as inhibition by oxygen, complicated volume relaxation and stress development, complex polymerization kinetics, and the formation of highly heterogeneous polymers/networks [5].

2.1.3.2. Cationic Photopolymerization

On the other hand, the virtues of photoinitiated cationic polymerization are rapid polymerization without oxygen inhibition, minimal sensitivity to water, and the ability to polymerize vinyl ethers, oxiranes (epoxides), and other heterocyclic monomers that do not polymerize by a free radical mechanism [1]. In analogy to free radical polymerizations, cationic polymerizations proceed as chain reactions involving initiation and propagation. However, in many cases, there is no termination by neutralization, and the growing chains are only terminated by nucleophilic impurities contained in the system [1].

2.2. “Click” Reactions

A new concept, which concerns the synthesis of organic materials, was described in 2001 by Sharpless et al. by taking advantage of many progresses in this field of research achieved in the 20th century [4]. In particular, by focusing on highly selective, simple orthogonal reactions that do not yield side products and that give heteroatom-linked molecular systems with high efficiency under a variety of mild conditions [5].

The main features of modular click reactions include high yields with by-products (if any) that are easily removable, mild, solventless (or aqueous) reaction conditions, insensitivity to oxygen or water, processability with a wide variety of readily available starting compounds, regiospecificity and stereospecificity, orthogonality with other common organic synthesis reactions [5].

Under the term “click reactions” several efficient reactions have been grouped (Figure 2), sharing the common feature to be capable of producing a wide variety of functional synthetic molecules and organic materials by reflecting the properties mentioned above [6].

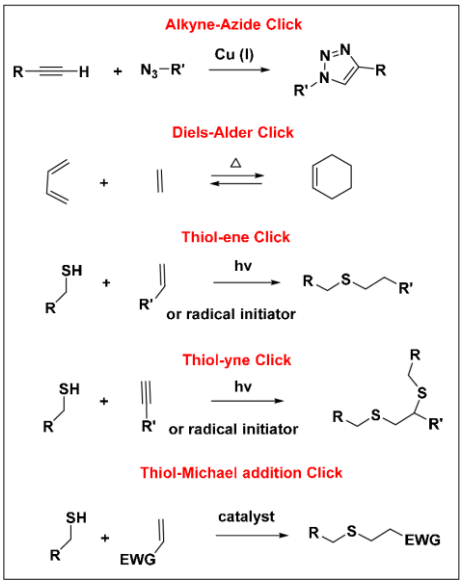

Figure 2- Schematic illustration of different types of click reactions [6].

2.3. Thiol-Ene Reactions

2.3.1. Thiol-Ene Reaction Features

Thiol-ene reactions (Figure 3), despite proceeding by a radical or anionic chain (termed thiol Michael addition), carry many of the qualities of click reactions [5]. The basic materials underlying these reactions are thiols (Figure 4), organic compounds characterized by one or more SH groups and also called mercaptans, and enes (Figure 5), containing reactive carbon–carbon double bonds. In particular, thiol acts as a radical receiver of the radical generated by the photoinitiator, as it is characterized by a higher reactivity than ene [7].

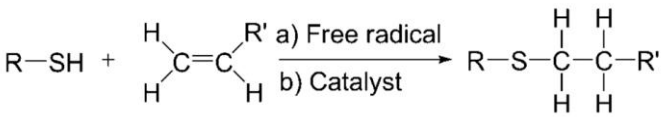

Figure 3- Schematic illustration of an idealized reaction between thiol and ene [5].

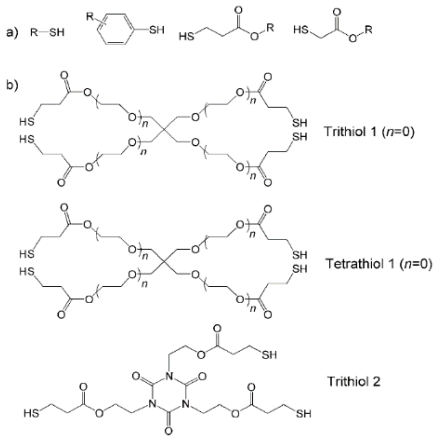

Figure 4- Illustrations of common a) alkyl thiols and (b) multifunctional thiols used in thiol–ene polymerization processes [5].

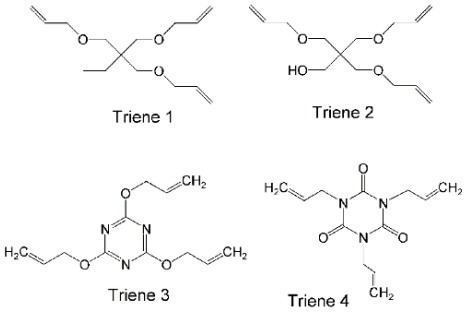

Figure 5- Illustrations of typical multifunctional enes used in thiol–ene polymerization processes [5].

These attributes include achieving quantitative yields, requiring only small concentrations of relatively benign catalysts, having rapid reaction rates with reactions occurring either in bulk or in environmentally benign solvents over a large concentration range, requiring essentially no clean up, being insensitive to ambient oxygen or water, yielding a single regioselective product, and the ready availability of an enormous range of both thiols and enes [5].

The overall simplicity and reliability of the thiol–ene reaction allow to overcome most of the critical limitations of traditional photoinitiated systems. In particular, by reducing shrinkage, stress and sensitivity to oxygen inhibition thanks to the possibility of taking advantage of a controllable combination of step-growth and chain-growth processes, in order to produce an homogeneous polymer network even under ambient atmospheric conditions and very rapidly.

2.3.2. Thiol-Ene Reaction Applications

Considering the remarkable properties of thiol-ene chemistry, specifically its exceptional versatility and propensity for proceeding to quantitative conversions under even the mildest of conditions, the range of suitable applications is very wide, varying from high performance protective polymer networks to processes that are important in the optical [8], biomedical [9], sensing [10], and bioorganic modification [11] fields.

In addition, thiol-ene radical reactions have been extended to novel and specific applications such as microfluidic devices [12], nano-imprinting [13] and holographic diffractive materials [14].

2.3.3. Thiol-Ene Drawbacks and Improvement

Despite many outstanding benefits, thiol-ene systems show some drawbacks, such as poor thermal properties and mechanical properties arising from the formation of flexible thio-ether linkages, which limit their application in some fields [5].

Therefore, to overcome these deficiencies, it has appeared very useful to incorporate second phases into traditional thiol-ene matrices in order to improve their thermal and mechanical properties. There are numerous examples in the literature, e.g. the addition of glass fibers [15], graphene sheets [16] and other kinds of nanofillers, as in the case of this thesis project regarding cellulose nanofibrils.

2.4. Cellulose

2.4.1. Cellulose Features and Sustainability

Nowadays, to solve numerous issues such as reduction of oil stocks and their geographical localization, plastic pollution, carbon footprint and sustainability, there is a strong push towards the replacement of fossil oil-based products with biodegradable [17] and/or bio-based ones [18]. Cellulose is the most abundant natural polymer and it's also a renewable, biodegradable and non-toxic material, therefore it represents a smart solution to the above-mentioned problems as it can be used to produce a wide range of environmentally friendly and biocompatible products. This material has been used for centuries as a source of heat, construction material or for manufacturing of several commodities in textile and paper industry, but he use of cellulose in high added value applications is still rare due to its insolubility in water and most organic solvents, hygroscopic character and no melting [19].

2.4.2. Cellulose Sources

Cellulose can be derived from a variety of sources, such as wood (hardwood and softwood), seed fibers (cotton, coir etc.), bast fibers (flax, hemp, jute, ramie etc.), grasses (bagasse, bamboo etc.), marine animals (tunicate), algae, fungi, invertebrates and bacteria [19].

Wood is presently the most important source of cellulose from an industrial point of view. Anyway, it also contains hemicellulose, lignin and a comparably small amount of extractives and inorganic salts so, as a consequence, even non-wood plants are receiving increasing interest since they, generally, presents a lower amount of lignin that allows easier fiber delignification and purification processes, as well as a less energy-consuming fibrillation.

Wood species can be distinguished as hard- and softwoods based on their anatomical features [19]. Hardwood has a more complex, heterogeneous and rigid structure respect to softwood [20], that is characterized by 3-4 times longer fibers. On the other hand, it was reported that softwood requires less mechanical treatment than hardwood to produce equivalent fibrillation level [21].

It should be also noted that the use of never-dried cellulose comparing to once-dried makes the fibrillation more favorable, since drying promotes irreversible hydrogen-bonding between nanofibrils, known as hornification [22]. Anyway, the dry cellulose is much easier to handle.

2.4.3. Cellulose Structure

Cellulose is a semicrystalline polymer comprising crystalline and amorphous regions within the microfibril and, depending on the origin of cellulose and the isolation method, the native degree of crystallinity is usually in the range of 40–70% [23].

The building blocks of cellulose polymer chain are D-glucopyranose (glucose) molecules. When linked together by β-1,4-glucosidic bonds they turn into anhydroglucose units. Two anhydroglucose units compose anhydrocellobiose, which is the repeating unit of cellulose polymer (Figure 6). Each anhydroglucose unit has six carbon atoms with three hydroxyl groups, giving a high degree of functionality to cellulose molecule [19].

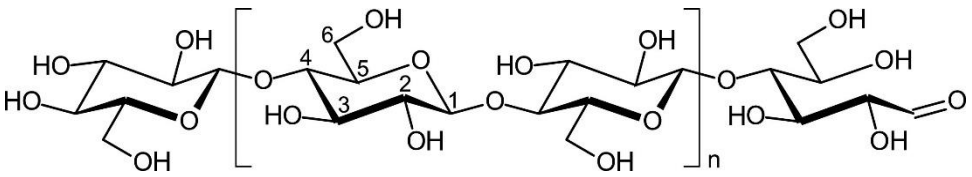

Figure 6- Illustration of the molecular structure of cellulose polymer [19].

This hierarchical structure (Figure 7), composed by fusion of both carbohydrate and polymer chemistry in a macromolecule made of repeating glucose units, generates impressively different architectures, reactivities and functions and, in addition, a high level of specificity.

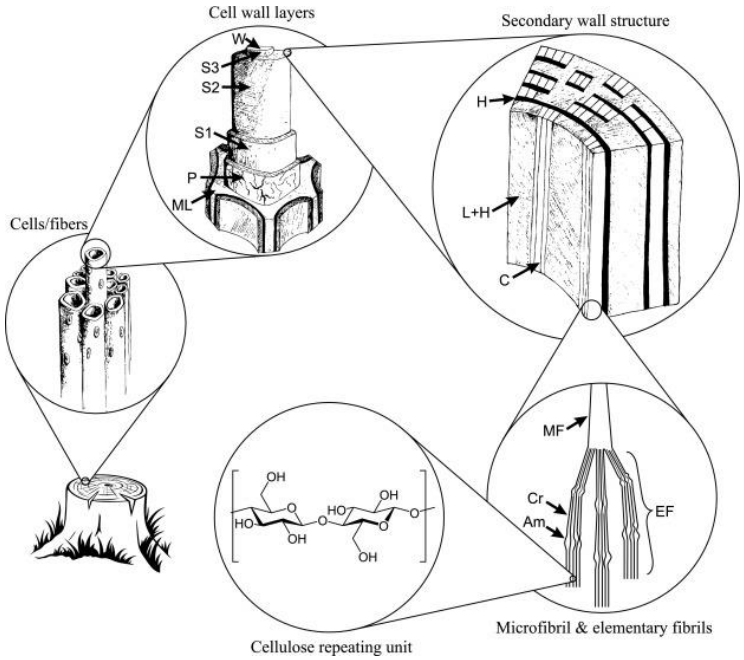

Figure 7- Illustration of the hierarchical structure of wood, showing: the middle lamella (ML), the primary wall (P), the outer (S1), middle (S2) and inner (S3) layers of secondary wall, the wartylayer (W), cellulose (C), hemicellulose (H), lignin (L), microfibril (MF), elementary fibril (EF), crystalline domain (Cr) and amorphous domain (Am) [19].

In contrast to carbohydrates of low molar mass, the reactions and properties of cellulose are determined by intermolecular interactions, cross-linking reactions, chain lengths and their distribution, and by the concentration of functional groups on the repeating units and along the polymer chains. Cellulose, unlike synthetic polymers, is characterized by distinctive polyfunctionality, high chain stiffness and presents also a remarkable sensitivity toward oxidation and hydrolysis of the chain-forming acetal groups, which regulate its handling and chemistry [23].

2.4.4. Nanocellulose

Generally, reference is made to nanocellulose in cases where the cellulose particles have at least one dimension in nanoscale (1–100 nm).

Depending on the production conditions, which influence the dimensions, composition and properties, nanocellulose can be divided into two main categories: 1) cellulose nanocrystals (CNC) or cellulose whiskers and 2) cellulose nanofibrils (CNF), also called nanofibrillated cellulose (NFC), microfibrillated cellulose (MFC) or cellulose nanofibers (Figure 8) [19].

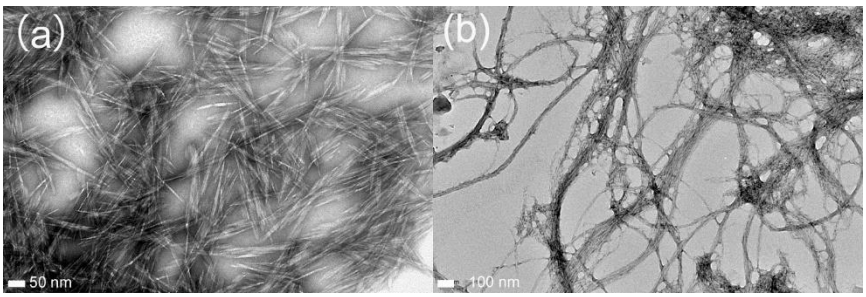

Figure 8- High-resolution transmission electron microscopy (TEM) images of (a) CNCs and (b) CNFs [24].

In addition, bacterial cellulose (BC) and electrospun cellulose nanofibers (ECNF) are also considered as nanocellulose but CNC and CNF are much more common especially considering large-scale production.

BC and ECNF are produced by bottom–up process such as buildup of nanofibers from low molecular weight sugars by bacteria or from dissolved cellulose using electrospinning, respectively. On the contrary, CNC and CNF are generated by disintegration of cellulose fibers into nanoscale particles with a top–down process. Regardless of the nanocellulose type, it exhibits hydrophilicity, relatively large specific surface area and broad potential of surface chemical modification [19].

2.4.4.1. Cellulose Nanofibrils (CNFs)

Using mechanical methods dry cellulose pulp can be disintegrated in order to obtain flexible CNFs in the form of elementary fibrils, with lateral dimensions starting from about 5 nm, or of microfibrils bundles, with diameters in the order of tens of nanometers, and characterized by a length of few micrometers typically, depending on the processing condition [19].

The interfibrillar hydrogen bonding energy should be exceeded in order to delaminate the nanofibrils and moreover reverse coalescence should be prevented [19]. For this reason, CNF is

commonly produced in aqueous medium, which loosens the inter-fibrillar hydrogen bonding, but due to its high water absorption capacity, it's usually dispersed at low concentration (usually < 5 wt.%) [19]. As a consequence, due to low solid concentration, suspensions appear very viscous and hard to handle.

The most common methods used for CNF's mechanical production are refining, homogenization and grinding, thanks to the high efficiency of delamination of fiber cell wall and CNF isolation, as well as to the possibility of being used industrially on a large scale [19].

A particularly effective technique used for the production of CNF is the ultra-fine friction grinding treatment, which is based on the use of Supermass colloider grinders (Figure 9). During this process, the cellulose slurry is passed between static and rotating grinding disks, the distance between them can be adjusted to avoid the problem of clogging. By the shearing forces generated between the discs, the cell wall is delaminated to isolate the nanofibrils [19].

This method was applied to produce the CNF aqueous suspension that has been used during the thesis project, namely the Masuko *Ultrafine Grinder MKZB15-50J* from the University of Maine to obtain a CNF concentration of ~1 wt.% [25].

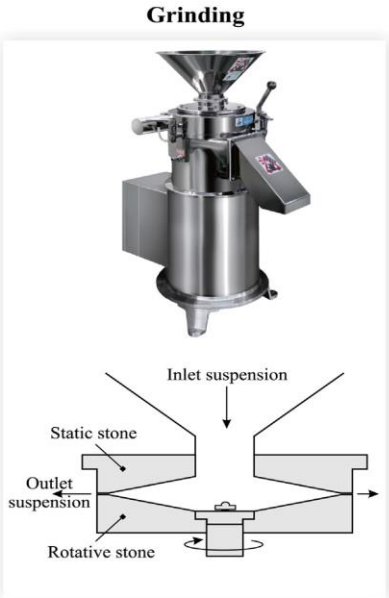

Figure 9- Supermass colloider grinder used in mechanical processes to produce CNFs [19].

2.4.4.2. TEMPO-Oxidized CNFs

In previous decades, the isolation of CNF was one of the most challenging issue due to the high energy demand required by mechanical disintegration process. However, with discovering strong influence of pretreatment methods, e.g. 2,2,6,6-tetramethylpiperidine-N-oxyl (TEMPO)-mediated oxidation [26] or enzymatic hydrolysis [27], which aim is to facilitate the mechanical disintegration, CNF became a more attractive material also for commercial applications.

However, the development of alternative methods that can benefit the production process and allow to obtain new properties for CNF still continues in the research field.

Regarding TEMPO-mediated oxidation, the introduction of negatively charged groups, such as carboxyl or carboxymethyl, on cellulosic fibers leads to an improvement in the delamination of the nanofibrils, thanks to electrostatic repulsion between the negatively charged cellulose nanofibrils [28].

This reaction is based on a system composed by TEMPO/NaBr/NaClO reagents in water at basic pH (Figure 10), the treatment basic principle is the oxidation of cellulose fibers by the nitrosonium ion ($^{+}$N=O), generated in situ through the reaction of TEMPO radical with the oxidants. Consequently, the primary alcohol groups of cellulose are converted into aldehydes, which are further oxidized to carboxylic groups linked to Na^{+} [26].

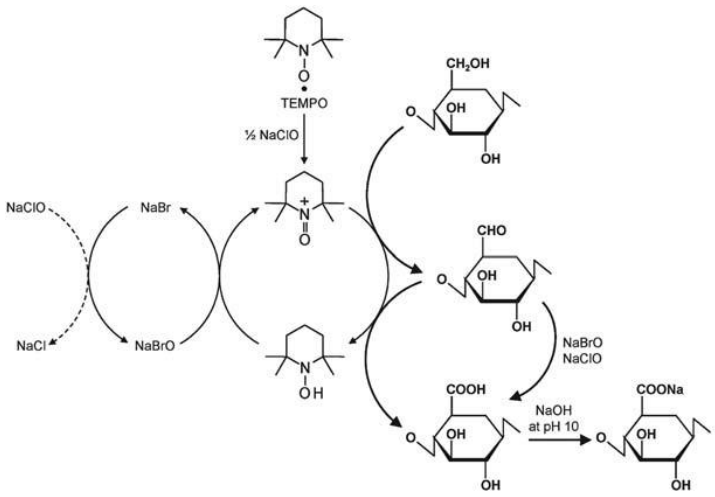

Figure 10- Schematic representation of the regioselective TEMPO oxidation of cellulose alcohol groups using TEMPO/NaBr/NaClO in water at basic pH [26].

The TEMPO oxidized cellulose with a sufficiently high content of carboxylate (Figure 11) makes it possible to get individual nanofibers with almost uniform widths of 3–4 nm, therefore smaller than the visible light wavelength that cause the water dispersion to be almost transparent (Figure 12). More specifically, the large amounts of carboxylate anions, present in high densities on the TOCNF surfaces, may cause the formation of such sufficiently individualized and long cellulose nanofibers by electrostatic repulsion and/or osmotic effects in water suspension, in contrast with former cellulose nanofibers that forms aggregates, resulting in low light transmittance [26].

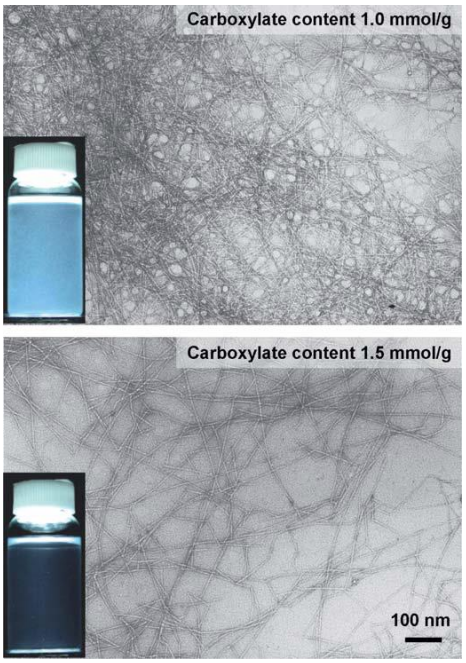

Figure 11- TEM images of dried dispersions of TEMPO-oxidized hardwood celluloses with carboxylate contents of 1.0 and 1.5 mmol g-1, observed by negative staining with uranyl acetate. The insets show the corresponding aqueous dispersions, showing the difference in transparency [26].

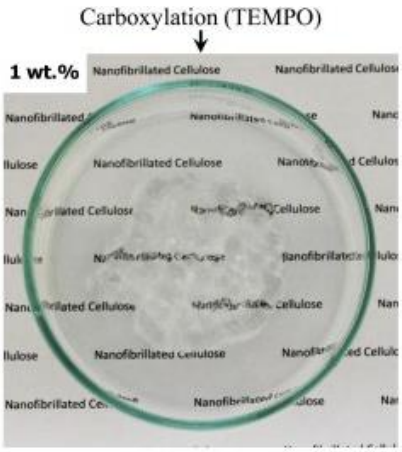

Figure 12- Visual appearance of TEMPO-oxidized CNF aqueous suspension at 1 wt.% (in Petri dishes, top view) [19].

2.5. Nanocomposites

The definition “nanocomposite” refers to a solid material composed by different phases where at least one of them has one dimension in nanometer size (10^{-9}-10^{-10} m) [29].

The nanometer level dimension determines strong interactions between matrix and reinforcing materials due to the outstanding surface area, allowing to obtain a composite with enhanced and specific properties.

The matrix material is composed by a continuous phase such as metallic [30], ceramic [31] or polymer [32] materials, on the contrary the reinforcing phase is dispersed and with different possible morphologies. In particular, the shapes of the second phases can be grouped into nanoparticles, nanoclays and nanofibers (Figure 13).

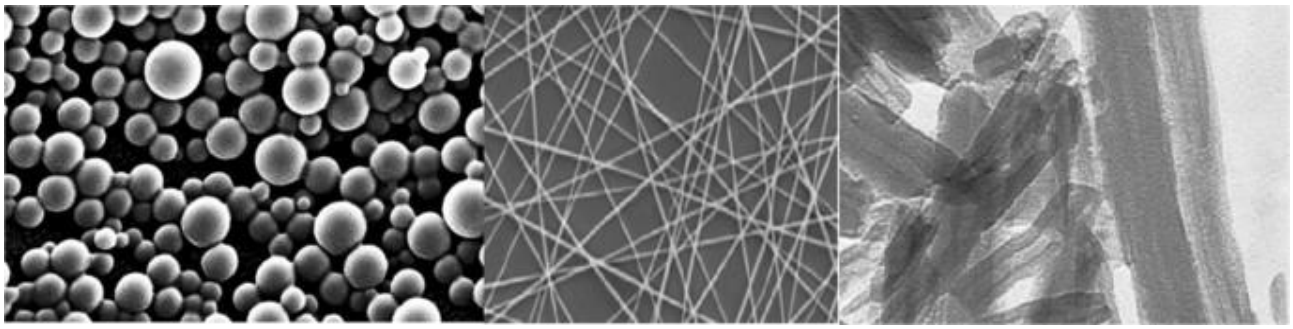

Figure 13- TEM images showing nanoparticles, nanofibers and nanoclays appearances [29].

2.5.1. Second Phase Morphologies

Reinforcing nanomaterial morphologies can be classified in nanoparticles, nanoclays and nanofibers.

2.5.1.1. Nanoparticles

In general, several different morphologies are categorised under the name of nanoparticles (NPs), for example spheres, tubes, rods and prisms [33] with the common feature to have all the dimensions at a nanometer scale.

These type of nanomaterials can be classified into inorganic, such as metal oxides, metals and quantum dots, and carbon-based materials, including fullerenes and carbon nanotubes [33].

NPs have attracted attention in numerous fields of application due to the tunability of their properties, including optical ones [34], as well as the increase in the mechanical and functional properties of the matrices [35].

2.5.1.2. Nanoclays

Nanoclays, platelet-like materials with a nanometre thickness, are obtained from multi-layered bulk materials by separating the single layers through exfoliation and by dispersing them throughout the matrix phase, in order to obtain the so-called "intercalated state" (Figure 14).

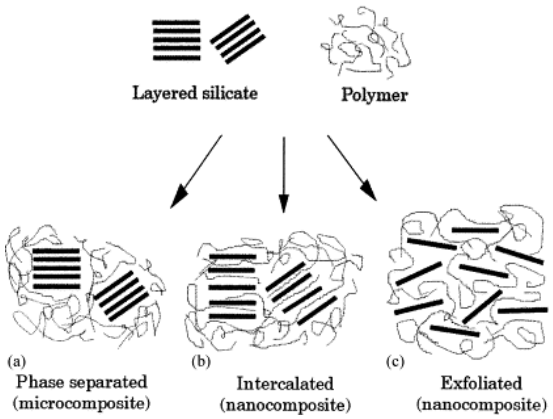

Figure 14- Schematic images representing different types of nanoclays dispersion [36].

In the event that this type of configuration is achieved, numerous benefits for the matrix are acquired such as enhanced thermo-mechanical properties but also reduced gas permeability [36].

Layered materials that are commonly used are montmorillonite, saponite, and synthetic as well as exfoliated graphite or graphene sheet [37].

2.5.1.2. Nanofibers

Nanofibers are characterized by two dimensions in the nanometre range and length in the order of µm or mm, with strongly anisotropic behaviour. Indeed, to reach a satisfying reinforcement it is

necessary to achieve high degree of alignment and effective stress transfer between matrix and second phase [38].

Different materials can be used to produce such fibers, for example polymers, carbon and semiconductors, with the possibility to obtain morphologies such as continuous nanofibers, nanowires and nanotubes or nanofibrous networks.

A wide variety of applications have been implemented for these types of reinforcing materials, specifically reinforcement in nanocomposites [39] but also filter media [40], tissue engineering [41] and micro/nano-electro-mechanical systems (MEMS/NEMS) [42].

2.5.2. Nanocomposite Advantages and Limitations

Nanocomposites represent a solution to overcome current constraints and problems of traditional microcomposite and bulk materials, as well as enabling novel properties otherwise unattainable.

The main benfits can be summarised as high surface/volume ratio which determines high reactivity and high effectiveness even when using concentrations lower than 5 wt.% [43], ability to enhance mechanical properties without reducing the ductility and to improve optical properties through the control of particles size which affects the light transmission [44].

Despite this, some difficulties still remain to be overcome, in particular regarding the lack of a complete knowledge of the relationship between nanostructure and properties [44], the difficulty in obtaining effective dispersion of nanofillers due to the high surface area [45], which leads to the generation of agglomerates due to the strong interactions between the particles, this also determines a limit in the quantity of nanoparticles that can be inserted in the formulation with a consequent limit in the obtainable properties, finally, the relationship between cost and effectiveness must also be taken into account, since special instrumentation is needed to process and characterise this type of material [44].

2.5.3. Polymer Nanocomposites

The concept behind polymer nanocomposites is to exploit the high interfacial area between the nanofillers and the macromolecules in order to improve the matrix properties but also to obtain new ones compared to those obtainable with traditional composites [46].

In particular, the improvement concerns not only mechanical properties but also functional ones such as flame retardancy or electrical conductivity [47] for example.

2.5.3.1. Cellulosic Polymer Nanocomposites and their Applications

Nanocellulose, thanks to biocompatibility and renewable source, but also surface chemistry tailorability, attractive optical properties and excellent mechanical properties (e.g. 150 GPa and 140 GPa Young's modulus, 10 GPa and 3 GPa tensile strenght for CNCs and TOCNFs respectively [48,49]), demonstrates wide applicability in different fields (Figure 15) and to be of growing interest.

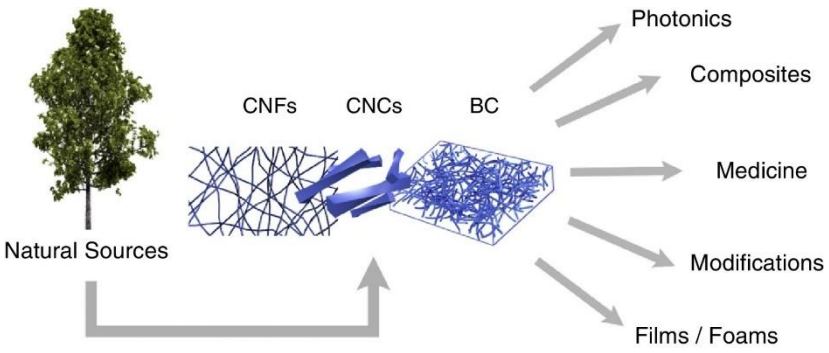

Figure 15- Grafical abstract representing some application fields of nanocellulosic materials, e.g. celllulose nanofibrils (CNFs), cellulose nanocrystals (CNCs) and bacterial cellulose (BC) [48].

In addition, nanocellulose exhibits other interesting features such as versatile chemical and processing options, compatibility with a wide range of polymer, living cells and proteins, tailorable physical and mechanical properties depending on aspect ratios and structures [48], that makes this nanomaterial very attractive for advanced polymer nanocomposites field.

Over the years, cellulosic nanocomposites have been used in numerous sectors, as evidenced by numerous detailed reviews, including protective coatings, barrier films, biomedical applications, composite hydrogels, photonics, optical applications, thermoplastics and protein composites, electronics, superhydrophobic surfaces and nanoimprint lithography [48,50,51].

2.5.4. Thiol-Ene Chemistry and Nanocellulose

The benefits of thiol-ene chemistry have also been used in the field of nanocellulose, in particular to improve polymer matrix compatibility and dispersion [52], to increase hydrophobicity [48] or in general to add specific functional groups on cellulose surface [53].

2.5.4.1. Thiol-Ene Systems in UV Nanoimprint Lithoraphy (UV-NIL)

Recently, UV nanoimprint lithography (UV-NIL) (Figure 16), thanks to its production process semplicity, cost-effectivity and high-throughput [54], has gained increasing interest as an alternative to traditional photo-lithography. In particular, it allows to obtain high-resolution nanostructures (Figure 17) as NIL but increasing the versatility in the choice of suitable materials.

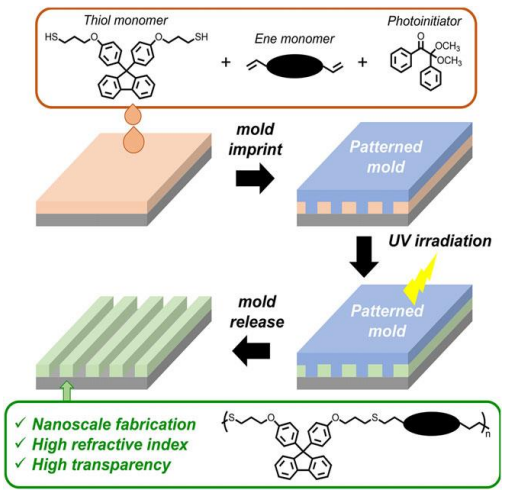

Figure 16- Schematic representation of UV-NIL process on a thiol-ene system [57].

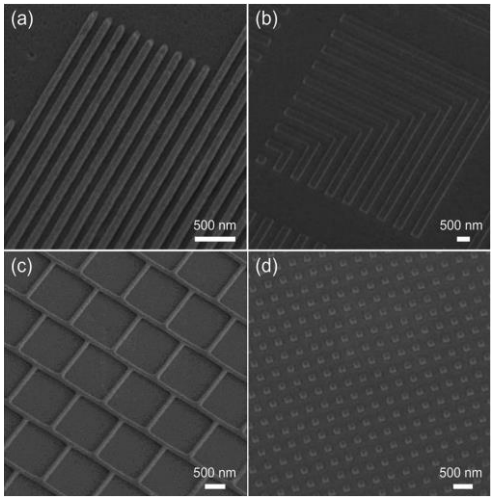

Figure 17- Scanning electron microscopy (SEM) images of UV-NIL nanostructured patterns [57].

Nowadays, acrylate-based materials are the most commonly used for that technique, but the oxygen inhibition represents a severe limitation [55,56]. As a consequence, thiol-ene chemistry and properties, already discussed in previous sections, are highly attractive to overcome this problem but also due to the high refractive index, related to the presence of sulfur atoms [57]. Thus, to meet the properties required for applications such as nanostructured photoresists and replica molds, including good mechanical properties, thermal stability and etch resistance, the development of nanocomposites such as inorganic-organic hybrids is very effective [54].

2.6. Nature-Inspired Hierarchical Surfaces with Micro- and Nano-Structures

Over the past decades, there has been a growing interest in bio-inspired materials [58] based on natural living beings such as leaves and petals but also wings and shells of different animals, and the possibility of mimicking their singular properties.

For example, polymers have been used to replicate the surface properties of these materials with the opportunity to produce synthetic surfaces with super-hydrophobic or super-hydrophilic behaviour (Figure 18) [58]. The role of hierarchical micro- and nano-structured surfaces and surface chemistry is crucial in achieving these exceptional wetting behaviours.

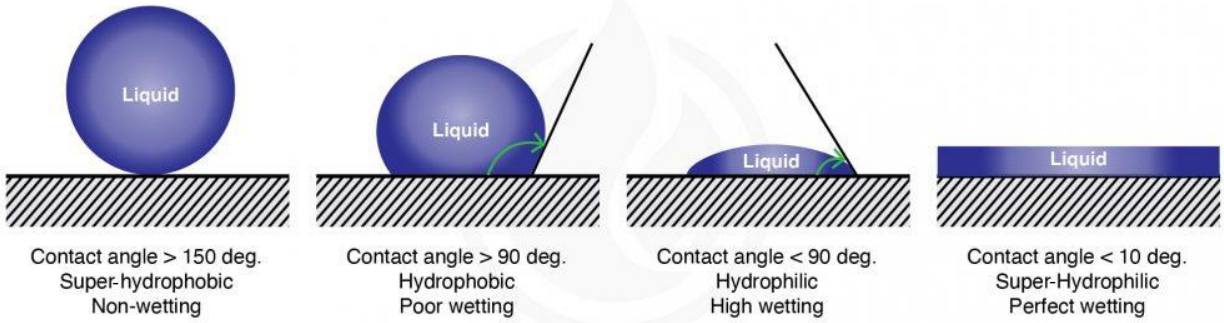

Figure 18- Schematic representation of general cases of wetting behaviour: super-hydrophobic, hydrophobic, hydrophilic, super-hydrophilic [67].

2.6.1. "Lotus Effect" and "Rose Petal Effect"

Rose petals and lotus leaves are part of the natural hierarchical structures with super-hydrophobic properties and have received considerable interest due to their different wetting behaviour as concern the interaction with water droplets (Figure 19), related to their differences in morphology, micro- and nano-structure (Figures 20 and 21) [59].

In particular, the adhesion of water droplets on the surface of lotus leaves is very low so that the droplet can slip easily allowing for self-cleaning properties. On the contrary, rose petals are characterized by a strong adhesion with water droplets and therefore these can remain attached to the surface even if the petal is placed upside down (Figure 22).

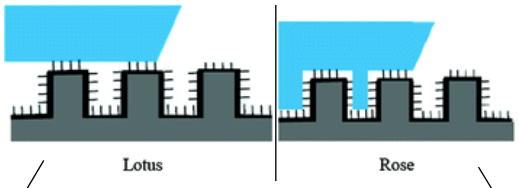

Figure 19- Schematic representation of lotus leaves and rose petals wetting behaviour [61].

Figure 20- SEM image of lotus leaves nano-structure with nano-pillars [60].

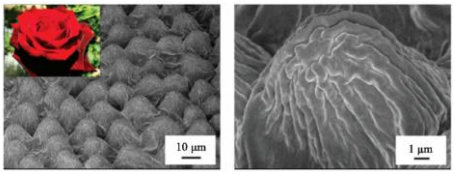

Figure 21- SEM images of rose petal micro- and nano-structure with micro-papillae and nano-folds [68].

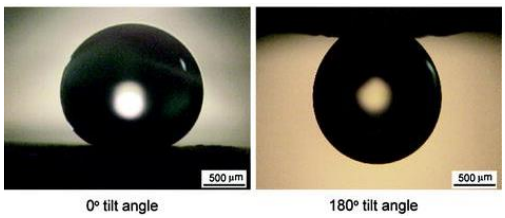

Figure 22- Rose petal static water contact angle (WCA) and upside-down behaviour [68].

2.6.2. Replication of Rose Petal and Lotus Leaf Hierarchical Surfaces

The most widely used method for replicating the surface of rose petals is UV nanoimprint lithography (UV-NIL), specifically using an intermediate negative polydimethylsiloxane (PDMS) mould into which a UV-curable resin is poured and then photo-cured under constant pressure to obtain a precise replica of the micro- and nano-structured surface [62]. This procedure takes place at room temperature and allows process times to be reduced, which greatly increases productivity.

There are several articles in the literature where this method has been used to produce rose petals polymer replicas with outstanding hydrophobic features, such as PDMS replica with 138.5° water contact angle (WCA) [63], hyperbranched polyester acrylate oligomer (HBP) + perfluoropolyether-urethane acrylate surfactant (PFUA) replica with 143° WCA [64] and perfluoropolyether (PFPE) replica with 139° WCA [65].

In addition, with the same procedure lotus leaves were also mimicked using materials such as HBP + PFUA with 151° WCA [64] and epoxy resin (RenShape SL 5180) with 155° WCA [66].

3. Materials and Methods

3.1. Selection and Categorization of Resin Contents

The materials used in the production of nanocomposite resins have been listed in Table I together with their role and specifications.

Table I: Chosen materials for resin preparation.

Name	Acronym	Molecular formula	Brand	Molecular weight (g/mol)	Purity / Concentration	Role
Trimethylolpropane diallyl ether	TMPDE	$C_{12}H_{24}O$	Sigma Aldrich	214.30	90%	Ene monomer
Trimethylolpropane tris (3mercaptopropionate)	TMPTMP	$C_{15}H_{26}O_6S_3$	Sigma Aldrich	398.56	≥95%	Thiol monomer
2,2-Dimethoxy-2-phenylacetophenone	DMPA	$C_{16}H_{16}O_3$	TCI Chemicals	256.30	>98%	Photoinitiator
Butylated hydroxytoluene	BHT	$C_{15}H_{24}O$	Sigma Aldrich	220.35	≥99%	Inhibitor
TEMPO-oxidized cellulose nanofibrils (H_2O suspension)	TOCNFs	-	University of Maine	-	1 wt.%	Fillers
3-(Methacryloyloxy) propyltrimethoxysilane	MPS	$C_{10}H_{20}O_5Si$	Sigma Aldrich	248.35	98%	TOCNF surface modifier
3-(Mercaptopropyl) trimethoxysilane	MPTMS	$C_6H_{16}O_3SSi$	Sigma Aldrich	196.34	95%	
Tetrabutylammonium hydroxide	Bu_4NOH	$C_{16}H_{37}NO$	Sigma Aldrich	259.47	40 wt.%	
N,N-Dimethylformamide	DMF	C_3H_7NO	Acros Organics	73.09	99,5%	Solvent(s)
Ethanol	EtOH	C_2H_5OH	Fisher Chemical	46.07	≥99.5%	
Toluene	-	C_7H_8	Acros Organics	92.14	≥99.8%	
Acetone	-	C_3H_6O	Thommen-Furler	58.08	≥99.5%	

The resins were categorized based on calculated CNF volume percentages and their surface modifications as well as the chosen solvents, as shown in Table II. All TOCNF surface modification(s) were added as 1:1 weight ratio with respect to the TOCNF weight.

Table II: Classification of nanocomposite resin formulations.

Sample name	TOCNFs vol.%	TO-CNFs surface modification(s)			Solvent(s)
		hydrolyzed-MPS	Bu_4NOH	hydrolyzed-MPTMS	
Unm	10	-	-	-	DMF, EtOH-Toluene (95:5 wt.%)
mod1	10	√*	-	-	EtOH-Toluene (95:5 wt.%), Acetone
mod2	10	-	√*	-	Acetone
mod3	10	√*	√*	-	Acetone
mod4	5	-	√*	-	Acetone
mod5	1	√*	√*	-	Acetone
mod6	0.5	√*	√*	-	Acetone
mod7	0.5	-	√*	√*	Acetone
mod8	1	-	√*	√*	Acetone

3.2. Preparation of TOCNF Surface Chemistry Modifiers

3.2.1. Pre-Hydrolysis of Modifiers with Ene and Thiol Moieties

A pH 1 water was obtained by adding 1.5 g of Hydrochloric acid (HCl) into 24.5 g of water (about 6 wt.%), after that, 10 g of 3-(Methacryloyloxy) propyltrimethoxysilane (MPS) was mixed with 2.2 g of pH 1 water together with 1.25 g of ethanol in order to improve the miscibility between MPS and water, until a pH of 4 was obtained. The homogeneous solution thus obtained was subjected to magnetic stirring at 1000 revolutions per minute (rpm) at room temperature overnight to ensure the hydrolysis reaction of the MPS. Finally, a degassing step was applied via a vacuum oven at 70 mbar and 50 °C for 1.5 hours to evaporate residual water and obtain pre-hydrolysed MPS (Figure 23).

The same procedure and quantities were also used in for the pre-hydrolysis of 3-(Mercaptopropyl) trimethoxysilane (MPTMS) (Figure 24).

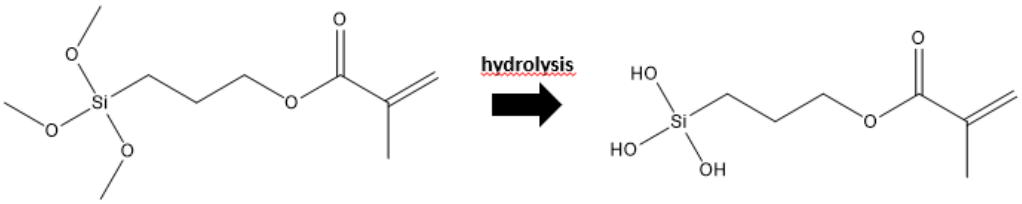

Figure 23- Schematic representation of the change in the molecular structure due to the hydrolysis step of MPS; specifically, CH_3 groups are replaced by OH groups.

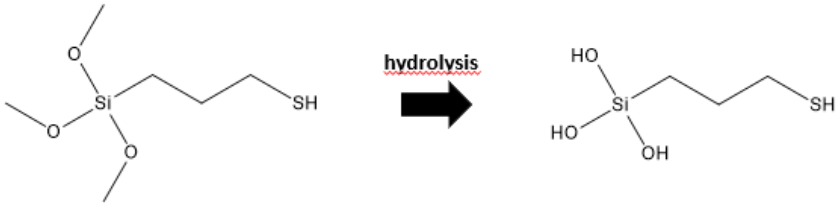

Figure 24- Schematic representation of the change in the molecular structure due to the hydrolysis step of MPTMS; specifically, CH_3 groups are replaced by OH groups.

3.2.2. TOCNFs Surface Modification with Bu_4NOH by Ion Exchange

A certain amount (Table IV) of TOCNFs water suspension (1 wt.%) was added to Bu_4NOH water suspension (40 wt.%) in order to reach 1:1 weight ratio. Then 2 min of vortex stirring and ultrasonication, with a duty cycle composed by 15 s of pulse time and 30 s of pause for a total pulse time of 5 min and a power of 55 W (10%), were applied for mixing. The solvent exchange step was performed by using centrifugation (Heraeus Biofuge Primo, Thermo Scientific, Switzerland) at 6000 rpm for 10 min by removing the supernatant liquid and adding 5 mL of fresh solvent each time (operation repeated 3 times), also allowing the removal of unbound Bu_4NOH.

3.3. Preparation of Composite Films

3.3.1. Processing of Reference Resin without Fillers

A certain amount of Trimethylolpropane diallyl ether (TMPDE) was mixed with Trimethylolpropane tris (3mercaptopropionate) (TMPTMP) in order to obtain a thiol-ene molar ratio of 1:1, whereby the required volumes were calculated on the basis of the molecular structure (Figures 25,26) and physical properties of the two monomers, specifically the densities, 0.955 g/mL for ene and 1.210 g/mL for thiol, and the functionalities, 2 and 3 respectively. In addition, 2,2-Dimethoxy-2-phenylacetophenone (DMPA) (1 wt.%) and Butylated hydroxytoluene (BHT) (9 mmol/L dose [67]) were added to the formulation, mixing was ensured by applying vortex stirring until a homogeneous solution was obtained. Afterwards, the resulting resin was deposited on a glass slide substrate by spin coating with a duty cycle consisting of a first step at 300 rpm for 30 s and a second step at 500 rpm for 30 s. Finally, UV processing (ECE PC-2000, Dymax, USA) was performed for 1 min at 75 mW/cm^2 light intensity for the photocross-linking of the UV resin.

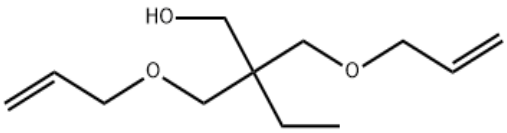

Figure 25- TMPDE molecular structure.

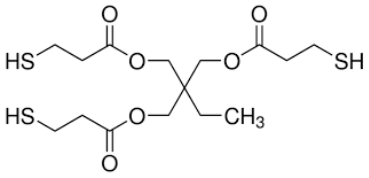

Figure 26- TMPTMP molecular structure.

3.3.2. Processing of Nanocomposite Films

The procedure for manufacturing nanocomposite films underwent several variations during the research project until the optimal process was determined. The different experiments used are listed in Table III below, together with a description of the problems and advantages of the different process steps used.

A detailed description of the processing of the different types of nanocomposite films produced follows.

Table III: Nanocomposite resin processing routes.

Processing route #	Chronological processing steps ⟶												
	High-shear mixing	Degassing	Solvent exchange (vacuum filtration)	Solvent exchange (centrifugation)	Ultrasonication 1 (before resin addition)	Resin addition	Ultrasonication 2 (after resin addition)	Solvent evaporation (silicon oil bath at 50 °C)	Solvent evaporation (fume hood at 25 °C)	Film deposition (casting)	Film deposition (spin coating)	Film deposition (manual doctor blading)	UV curing
1	√	√	√	X	X	√	√	√	X	√	X	X	√
2	X	X	X	√	√	√	√	√	X	X	√	X	√
3	X	X	X	√	√	√	√	X	√	X	X	√	√

Note: “X” = not done, “√” = done.

In conclusion, the procedure described in processing route 3 was selected as optimal and utilized for later experiments as described in following sections.

3.3.3. Photo-Crosslinking of Thiol-Ene Nanocomposites with as received TOCNFs

A certain amount (Table IV) of TOCNFs water suspension (1 wt.%) was subjected to high-shear stirring (Ultra-Turrax T25, IKA-Werke GmbH & Co. KG, Germany) at 10'000 rpm for 10 min to improve dispersion and homogeneity. Then the suspension was degassed for 20 min to remove air bubbles caused by the stirring step. By applying vacuum filtration for about 10 min with Durapore Polyvinylidene fluoride (PVDF) membrane (Merck Millipore, Germany) possessing 0.65 µm pores in diameter a hydrogel structure was obtained. This hydrogel was dipped in the solvent (DMF, EtOH-Toluene or Acetone) for 1 hour and recollected via vacuum filtration (operation repeated 3 times)

in order to ensure a complete solvent exchange from water. Ultrasonication step (Digital Sonifier 550, Branson Ultrasonics Corporation, USA) with a duty cycle composed by 15 s of pulse time and 1 min of pause for a total pulse time of 15 min and a power of 165 W (30%) was applied to break the hydrogel structure and ensure better dispersion. The thiol-ene UV-curable resin was prepared by mixing the monomers TMPDE (ene) and TMPTMP (thiol) with 1:1 thiol-ene molar functionality ratio, 1 wt.% of DMPA (photo-initiator) and 9 mmol/l of BHT (inhibitor). Afterwards, this mixture was added to the prepared TOCNF suspension. A further step of ultrasonication with the previously described parameters (together with temperature control < 50 °C to avoid thermally induced polymerization) was applied to improve particle dispersion and mixing of thiol-ene resin medium and TOCNFs. The solvent was mostly evaporated after about 2.5 hours inside a silicon oil bath kept at 50 °C. The formulation was poured into a silicone mold with glass slides as substrate (Figure 27). The complete solvent evaporation was ensured by reaching a constant weight upon waiting. UV processing (ECE PC-2000, Dymax, USA) was performed for 1 min at 75 mW/cm^2 irradiance to photocross-link the resin resulting with a nanocomposite film forming on the glass substrate.

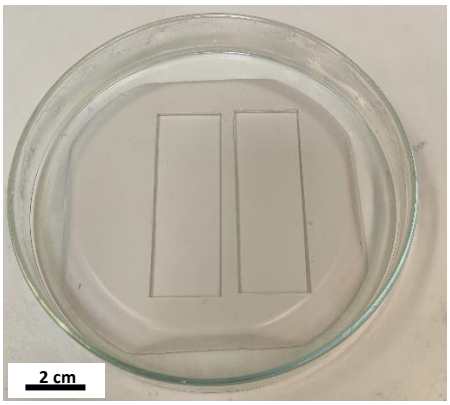

Figure 27- Silicone mold with glass slide substrates used to produce films by casting followed by UV curing.

3.3.4. Photo-Crosslinking of Thiol-Ene Nanocomposites with hyMPS/hyMPTMS-Modified TOCNFs

The processing path was the same as described above for TOCNFs nanocomposites but the following steps have been added: after solvent exchange a certain amount (Table IV) of pre-hydrolyzed MPS was added in order to reach 1:1 weight ratio respect to TOCNFs, ultrasonication with a duty cycle composed by 15 s of pulse time and 30 s of pause for a total pulse time of 5 min and a power of 55 W (10%) was applied to help hyMPS mixing and the formulation was washed with fresh solvent and recollected by vacuum filtration (operation repeated 3 times) to remove unbound hyMPS.

The same procedure and quantities were also used in the case of hyMPTMS.

3.3.5. Photo-Crosslinking of Thiol-Ene Nanocomposites with Bu_4NOH-Modified TOCNFs

As described in section 3.2.2., the TOCNFs have been modified with Bu_4NOH.

Then, dispersion through ultrasonication, UV resin mixing and UV irradiation were applied with the same procedure described above but the formulation transfer on glass substrate was performed by using spin coating, with different rotational speeds (revolutions per minute, rpm) based on formulation compositions (Table V).

3.3.6. Photo-Crosslinking of Nanocomposites with Double Modified TOCNFs

The processing route began with Bu_4NOH modification of TOCNFs which was continued with a certain amount (Table V) of hydrolyzed MPS (or hyMPTMS) addition to reach 1:1 weight ratio with respect to TOCNFs after solvent exchange. This was followed by ultrasonication at 55 W (10%) for 5 min of total pulse time to aid mixing. The formulation was separated from unbound hyMPS (or hyMPTMS) by centrifugation, supernatant removal and fresh solvent addition (operation repeated 3 times). Solvent removal took place under the fume hood at room temperature, waiting overnight and covering the resin with Al foil to avoid exposure to light. The nanocomposite resin was then deposited on the glass substrate by manual doctor blading and UV-cured.

Table IV: List of quantities used in the preparation of formulations.

Sample Type	TOCNF vol.%	TOCNF H_2O suspension weight (g)	Calculated TOCNF weight (mg)	TMPDE* volume (mL)	TMPTMP* volume (mL)	DMPA weight (mg)	BHT weight (mg)	hyMPS weight (mg)	hyMPTMS weight (mg)	Bu_4NOH H_2O suspension weight (mg)	Calculated Bu4NOH weight (mg)
reference resin	-	-	-	2.6	2.4	50	10	-	-	-	-
unm	10	6	60	0.21	0.19	4.5	1	-	-	-	-
mod1	10	6	60	0.21	0.19	4.5	1	70	-	-	-
mod2	10	6	60	0.21	0.19	4.5	1	-	-	175	70
mod3	10	6	60	0.21	0.19	4.5	1	70	-	175	70
mod4	5	6	60	0.44	0.41	10	2	-	-	175	70
mod5	1	6	60	2.3	2.15	50	10	70	-	175	70
mod6	0.5	6	60	4.5	4.2	100	20	70	-	175	70
mod7	0.5	6	60	4.5	4.2	100	20	-	70	175	70
mod8	1	6	60	2.3	2.15l	50	10	-	70	175	70

*TMPDE and TMPTMP amounts are based on calculations that take their physical and chemical parameters into account resulting with a thiol-ene molar functionality ratio of 1:1 and the desired TOCNF volume concentration. The monomer parameters were taken from Sigma Aldrich (USA) and the TOCNF weight concentration from the University of Maine (USA), companies from which they were purchased. In addition, the BHT concentration to be used was taken from the article by Esfandiari et. al [67], Bu_4NOH processing parameters from Shimizu et. al [71] and MPS ones from Lu et al. [72] and Galland et al. [73].

Table V: Procedures used for spin coating multiple resin types.

Samples	**1st step**	**2nd step**
Reference resin without particles	30 s – 300 rpm	30 s – 500 rpm
mod5	30 s – 300 rpm	60 s – 3000 rpm
mod6	30 s – 300 rpm	60 s – 2000 rpm

3.4. Replication of Micro- and Nano-Structured Lotus Leaf surface to obtain Super-Hydrophobic Films

The surface of the Nelumbo Lutea (lotus) leaf was first mimicked with a polydimethylsiloxane (PDMS) template as a negative replication. The PDMS resin was mixed with the curing agent (present with the resin in the Sylgard 184 Silicone Elastomer Kit, Dow, Germany) with a 10:1 weight ratio, specifically 80 g and 8 g respectively, until a homogenous mixture was obtained, which was then degassed for 10 min. In parallel, lotus leaves were cut to generate 2x2 cm^2 square substrates and placed at the bottom of a Petri dish with a double-sided scotch tape of the same size (3 lotus leaves per Petri dish). After degassing, the mixture of PDMS and curing agent was poured into the Petri dish until the leaves were completely covered with a sufficiently thick layer allowing safe handling. Then the Petri dish was degassed for 20 min to remove air bubbles. After 48 hours at room temperature the PDMS was assumed as completely cured and the 2x2 cm^2 PDMS squares were cut and used as negative replicas of the micro- and nano-structured surface of the lotus leaves. Subsequently, UV resin (with or without modified TOCNFs) was deposited on a poly(methyl methacrylate) (PMMA) substrate using the doctor blade technique to obtain a 200 µm thick film. The PDMS negative template was placed on resin and a pressure of 2 bar was applied to the assembly. Finally, after waiting for a creep time of 2 or 5 min to allow the resin to flow throughout the nanostructure, UV light was applied at 75 mW/cm^2 for 3 min for crosslinking.

Once the PDMS negative template was removed from the top, the film with a positive replica of the nanostructured lotus surface was obtained.

3.5. Characterization Methods

3.5.1. Fourier Transform-Infrared (FT-IR) Spectroscopy

The FT-IR technique was used to evaluate the thiol-ene reaction between TMPDE and TMPTMP and the effectiveness of TOCNFs surface modifications. Specifically, the Nicolet 6700 FT-IR Spectrometer

(Thermo Fisher Scientific, USA) was used for analysis in a wavenumber range between 650 and 4000 cm^{-1} with transmission method.

The effectiveness of the surface modification of TOCNFs with Bu_4NOH and hyMPS or hyMPTMS was tested by comparing the FT-IR spectra of unmodified and modified TOCNFs, in particular using samples consisting of dried cellulose nanofibrils embedded in a potassium bromide (KBr) disk through the procedure described below.

A given amount of as received TOCNFs suspension, specifically 6 g, was solvent-exchanged with acetone through centrifugation at 6000 rpm for 10 min (3 times) to benefit from faster solvent evaporation. Then, the solvent was completely evaporated by heating in oven at 120 °C until dried agglomerates of the material are obtained. Finally, the resulting powder, about 60 mg, was mixed with KBr powder to obtain a concentration of 1.5 wt.% and then pressed for 2 min at 10 bar to form a disk. The disk was heat-treated in an oven at 120 °C for 2 days to ensure complete removal of residual moisture and then characterized by FT-IR.

The same procedure was also followed for the TOCNFs modified with Bu_4NOH after mixing the Bu_4NOH water suspension with that of TOCNFs, in particular by using an amount to achieve a 1:1 weight ratio as in the modification processes described above. The solvent exchange steps also allowed the unbound Bu_4NOH to be removed.

In the case of the hyMPS and hyMPTMS modified TOCNFs, the mixing step with the silane took place following solvent exchange step and a fresh solvent washing step through centrifugation (3 times) was added to remove the unbound silane.

3.5.2. Zeta Potential Measurements

For further investigation regarding the Bu_4NOH surface modification of TOCNFs, zeta potential measurements were performed with Zetasizer Nano ZS (Malvern Panalytical, UK).

The analyzed samples consisted of water suspension diluted to 0.1 wt.% of TOCNFs and Bu_4NOH modified TOCNFs.

3.5.3. Ultraviolet-Visible Light (UV-Vis) Spectroscopy

UV-Vis measurements were carried out with the Lambda 365 UV-Vis Spectrophotometer (PerkinElmer, USA) in a wavelength range set from 250 to 700 nm and with transmittance method, in order to evaluate the transparency of the UV-cured nanocomposite films produced respect to the UV-cured reference resin film. At 400 nm wavelength the exchange between visible and UV sources takes place, resulting in a slight discontinuity in transmittance related to the measurement artifact.

The analyzed samples consisted of UV-cured films of different compositions of about 200 µm thickness on glass substrate, produced by manual doctor blading; the blank glass tile was used as baseline for the measurement.

3.5.4. Thermogravimetric Analysis (TGA)

A thermogravimetric analysis was used to assess the thermal degradation of various materials including UV-cured reference resin, dried TOCNF powder and UV-cured nanocomposite film with the aim of comparing their thermal stability. The dried TOCNF powder was obtained following the same procedure as described for the preparation of samples for FT-IR analysis, without embedding the powder in the KBr disk.

Specifically, samples of about 10 mg were tested with air flow with a temperature ramp from 30 to 600 °C at a constant rate of 10 °C/min, by using the TGA 4000 Thermogravimetric Analyzer (PerkinElmer, USA).

3.5.5. Rheology Analysis

The flow behaviour of monomers (TMPDE and TMPTMP), reference and nanocomposite resins before UV-curing was analyzed with Modular Compact Rheometer MCR 302e (Anton-Paar, Austria) in the plate-plate configuration (25 mm diameter). Specimens of approximately 500 µL were subjected to a shear rate between 0.1 and 100 1/s.

3.5.6. Photo-Rheology Analysis

The AR 2000ex Rheometer (TA Instruments, USA) was used to perform photo-rheometry analysis in order to evaluate the curing behaviour of the nanocomposite resins with respect to the reference resin.

Specifically, specimens of about 100 µL were subjected to UV radiation of 5.5 mW/cm^2 intensity via 200 W Series 2000 OmniCure UV3-Surface Cure Lamp (Exfo, Canada) after 20 s of pre-shearing, maintaining the application of a 1% strain with 1 Hz frequency, at room temperature (25 °C); light intensity was measured and calibrated using the Silver Line UV Radiometer (CON-TROL-CURE, Germany).

3.5.7. Photo-Differential Scanning Calorimetry (Photo-DSC)

In order to evaluate the effect of the surface modifications on the kinetics of the photo-crosslinking with respect to the reference resin, a photo-DSC analysis was carried out on specimens of about 20 mg by applying a UV light intensity of 0.5 mW/cm^2 after 2 minutes of waiting (to allow to reach a stable condition) for about 20 minutes to ensure the completion of the reaction, at room temperature (25 °C). The light intensity of 0.5 mW/cm^2 was used to allow a slower reaction to follow the kinetics more precisely.

In particular, we focused on the effect of both the concentration of TOCNFs and the type of surface modification applied on cellulose nanofibrils.

3.5.8. Nanoindentation Measurements

The effect on the mechanical properties of the produced films related to the addition of TOCNFs in the reference resin was evaluated through nanoindentation measurements, in particular by focusing on property variations such as reduced modulus and surface hardness.

The tests were performed on UV-cured nanocomposite films, produced as described in the Materials and Methods section, and compared to the properties of the UV-cured reference resin film.

In particular, the Hysitron TI 950 TriboIndenter nanoindenter (Bruker,USA) was used applying nanoindentation arrays of 16 to 100 indents with 10 to 150 µN force and power law was used for fitting the unloading curves.

3.5.9. Contact Angle Measurements and Self-Cleaning Test

The measurements of the contact angles were carried out with the DSA20E Easy Drop Goniometer (Krüss, Germany), to test the wetting behaviour of the surfaces of the nanocomposite films with respect to the reference resin film. Specifically, the sessile drop method was used by depositing 2 µL drops of different liquids, both polar and non-polar, such as distilled water, ethylene glycol and diiodomethane (Table VI), at room temperature (25 °C). For each sample, 3 measurements were repeated for each liquid.

In addition, the water contact angle (WCA) of the lotus leaf replica films, produced as described in chapter 3.4. of the Materials and Method section, was also measured but by depositing 8 µL water drops, both for reference and nanocomposite resins.

Table VI: Surface energy contributions of different liquids used in contact angle measurements.

Liquid	Surface Energy Contribution [mN/m]		
	Polar	Dispersive	Total
Water	51.0	21.8	72.8
Ethylene Glycol	19.0	29.0	48.0
Diiodomethane	0.0	50.8	50.8

Finally, the self-cleaning test was performed on the nanoimprinted composite film by placing pepper grains on the surface, tilting it and dropping drops of water on it. This test made it possible to assess whether the patterned film exhibited self-cleaning properties, in the event that water was able to trap hydrophobic particles, such as pepper, by sliding over the surface.

3.5.10. Scanning Electron Microscopy (SEM)

The samples for SEM analysis were prepared by immobilizing them on sample holders using double-side carbon tape. In addition, a thin copper foil with a conductive glue was applied between a small spot of the sample surface and the metal sample holder to reduce charging. Then, a 10-nanometer layer of Iridium was deposited on the samples using the Q150T magnetron sputtering multi-coater (Quorum Technologies, UK) to make the surface conductive and therefore analysable with SEM. Iridium was chosen because it allows to obtain smoother and more homogeneous coating, even if very thin, compared to gold and therefore allows to analyse the surface morphology with a greater magnification and higher resolution [68].

The analyzed specimens consist of the PDMS template, which represents the negative replica of the nanostructured surface of the lotus leaf, and the films nanopatterned by UV-NIL technique, which show the positive replica of the lotus leaf surface, made of reference resin and nanocomposite resin with 0.5% vol Bu_4NOH-hyMPS-TOCNF. For the study of nanopatterned surface morphology, images were acquired with SEM (Gemini-SEM 300, Zeiss, USA) by using the In-Lens detector at a working distance of 3 mm and acceleration voltage of 1 kV, and the secondary electrons external detector (SE2) at a working distance of 6 mm and acceleration voltage of 3 kV.

4. Results and Discussion

4.1. Optimization of the Cured Reference and Composite Films Preparation Method

Various process steps were evaluated during the continuation of the thesis project, with the aim of achieving the optimal process for the production of cured reference and composite films. Specifically, the objective is to obtain a free-flowing resin following complete solvent evaporation, with the highest loading possible by maintaining the particles homogeneously dispersed without the use of dispersants and additives, in order to produce smooth and transparent films with enhanced mechanical properties.

The application of high-shear stirring, followed by degassing, was not satisfactory regarding both TOCNFs dispersion and mixing, therefore was avoided for later steps. On the other hand, ultrasonication showed an improved particle dispersion and resin mixing. Therefore, high-shear mixing step was replaced with ultrasonication.

The vacuum filtration step, used to allow solvent exchange, resulted in a loss of TOCNFs when applied following ultrasonication. This was due to the dispersion of the aggregates of cellulose nanofibrils, which allowed the TOCNFs to pass through the filter, making their concentration unpredictable. Weight loss was proved by measuring the mass of dried TOCNFs following a drying step at 120 °C. Specifically, 6 g of 1 wt.% TOCNFs water suspension yielded only about 30 mg dry

mass compared to the expected 60 mg. Thus, centrifugation ensures a solvent exchange step without the loss of TOCNFs and was therefore the better alternative.

The use of the silicon oil bath, as a method to completely evaporate the solvent, leads to the risk of losing material, due to the need to pour the formulation into a larger beaker to speed up the process. In addition, the combination of light, air and a temperature of 50 °C can cause pre-mature partial cross-linking of the resin. As a consequence, it is preferable to evaporate overnight at room temperature with an aluminium foil covering to safely avoid possible cross-linking of the resin.

Film deposition by casting does not allow control over the thickness of the film, as well as leading to the formation of an inhomogeneous film. Spin coating is a good alternative but can only be used for formulations that are not too viscous, in order to ensure a good resin spreading on the substrate. The doctor blade method was found to be a more suitable coating technique due to simplicity and improved thickness homogeneity compared to the previously mentioned methods despite potential human errors.

As a result of these considerations, the procedure described in processing route 3 was selected as optimal and utilized for later experiments. The transparency characterising the nanocomposite resin (Figure 28) shows that the dispersion of the double modified TOCNFs is very satisfactory.

Figure 28- Transparency of the nanocomposite resin, thanks to well dispersed modified CNFs.

4.2. Material Properties of TOCNFs and Modified TOCNFs

4.2.1. Thermal Stability of TOCNFs

TGA results (Figure 29) show that TOCNFs are characterized an onset temperature of thermal degradation of approximately 215 °C. The thermo-degradation process is characterized by three

steps: dehydration, depolymerization and decomposition of glycosyl-units [69], as shown also by derivative TGA (DTGA) results; moreover, they exhibit about 7-8 wt.% residual char when reaching 600 °C.

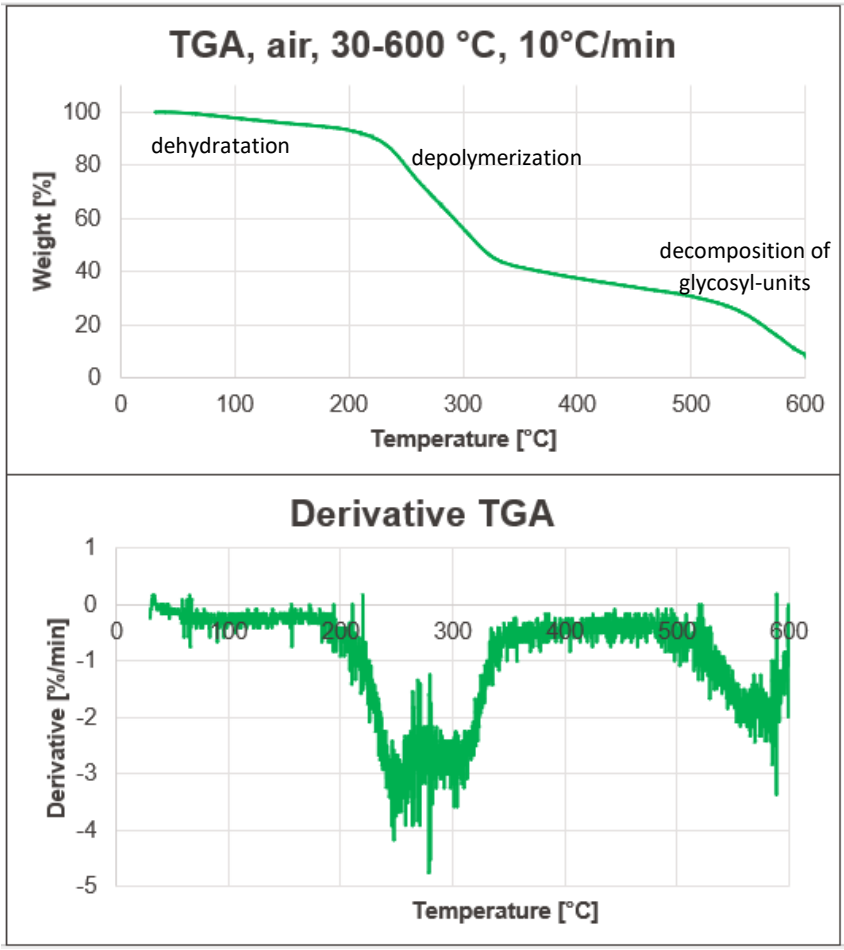

Figure 29- TGA and derivative TGA (DTGA) curve of dried TOCNF powder tested in air between 30-600 °C with a constant rate of 10 °C /min.

4.2.2. TOCNFs Surface Modifications

The successful surface modification of TOCNFs with hyMPS is proven by the absorption increase at the peak of the carbonyl group (C=O, approx. 1720 cm^{-1}) (Figure 30), which is already present in the spectrum of cellulose nanofibrils due to TEMPO-oxidation, due to the presence of carbonyl groups in the hyMPS molecules.

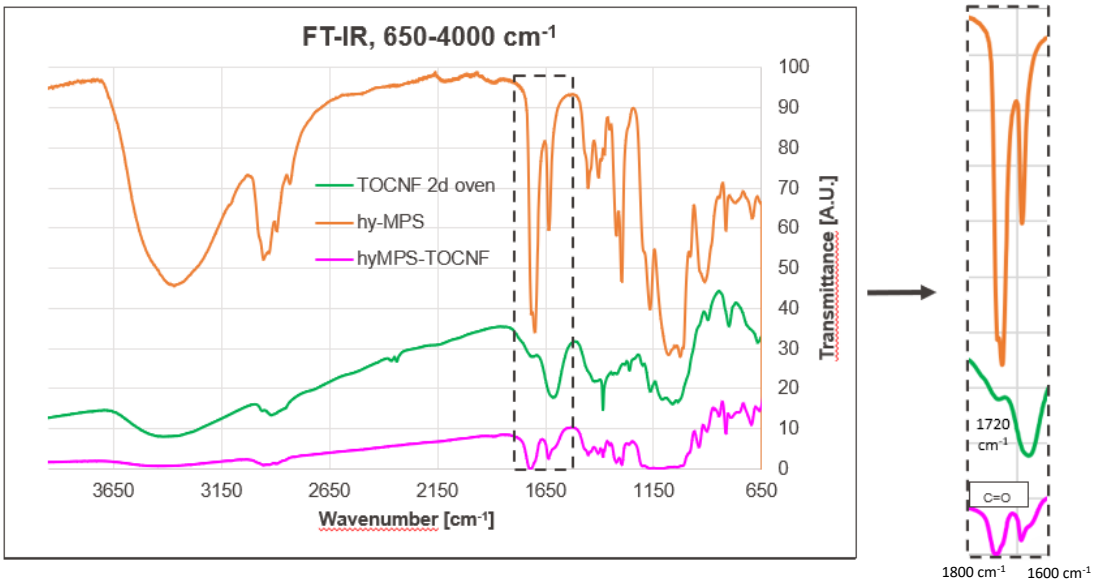

Figure 30- FT-IR spectra of dried TOCNFs (inside KBr disk), pure hydrolyzed MPS and dried hyMPS modified TOCNFs (inside KBr disk); both dried TOCNFs and hyMPS-TOCNFs samples were subjected to a drying step of 2 days in oven at 120 °C to ensure a reduction in residual humidity.

The modification of TOCNFs by hyMPTMS is ensured by the appearance of the thiol (SH) group peak (approx. 2550 cm^{-1}) (Figure 31), which is linked to the thiol groups present in the hyMPTMS molecules. The amplitude of the thiol peak is low but clearly visible compared to the spectrum of TOCNF where it is not present.

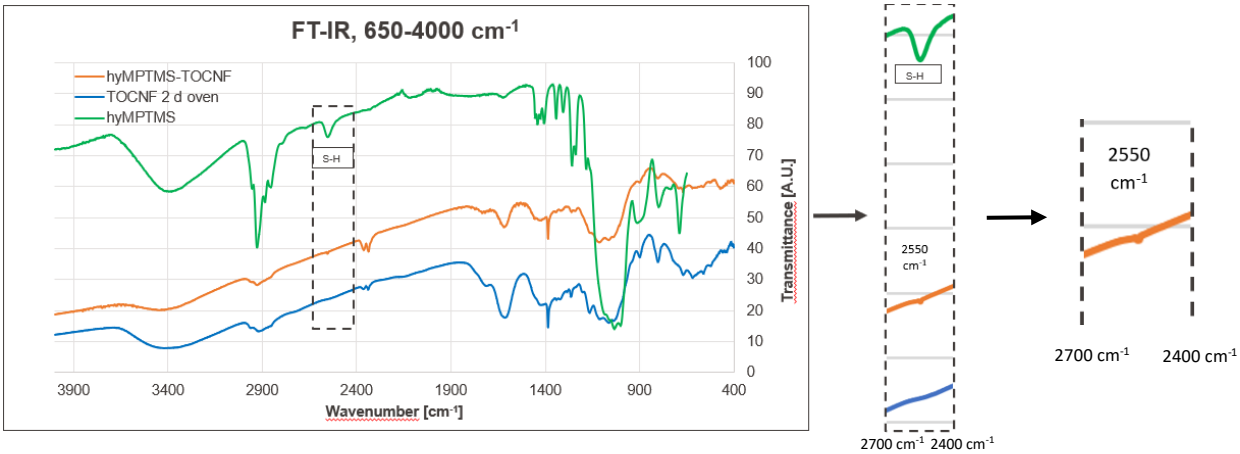

Figure 31- FT-IR spectra of dried TOCNFs (inside KBr disk), pure hydrolyzed MPTMS and dried hyMPTMS modified TOCNFs (inside KBr disk); both dried TOCNFs and hyMPTMS-TOCNFs samples were subjected to a drying step of 2 days in oven at 120 °C to ensure a reduction in residual humidity.

The presence of tetrabutylammonium bound to the surface of cellulose nanofibrils is demonstrated by the red shift of the C=O carbonyl group peak (approx. 1720 cm^{-1}) belonging to TOCNFs (Figure 32) due to the increased electronic density and the formation of permanent ionic bonds between COO- and N+, replacing covalent bonds with H atoms, related to the stable salt-like structure that has been generated. The red shift makes the C=O peak dominated by the larger adjacent peak (approx. 1650 cm^{-1}).

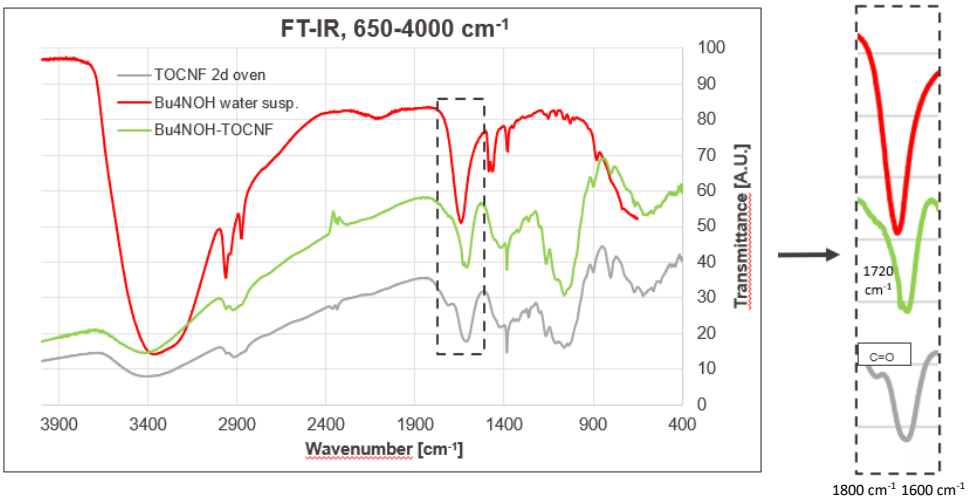

Figure 32- FT-IR spectra of dried TOCNFs (inside KBr disk), Bu_4NOH water suspension (40 wt.%) and dried Bu_4NOH modified TOCNFs (inside KBr disk); both dried TOCNFs and Bu_4NOH-TOCNFs samples were subjected to a drying step of 2 days in oven at 120 °C to ensure a reduction in residual humidity.

For further investigation regarding the Bu_4NOH surface modification of TOCNFs, zeta potential (Table VII) measurements were performed.

The decrease in the modulus of the zeta-potential following surface modification with Bu_4NOH shows that the modified cellulose nanofibrils exhibit a lower repelling power and thus lower stability in the aqueous medium. In contrast, dispersion in a non-aqueous apolar medium, such as the resin used in this project, will be better, in agreement with why the modification was applied on TOCNFs.

The zeta potential value of the Bu_4NOH-TOCNF water suspension may not be quantitatively accurate as it has a basic pH, unlike the neutral water suspension with TOCNF, which has an influence on the zeta potential. However, the above conclusions can still be considered qualitatively valid.

Table VII: Zeta-potential measurements results concerning TOCNFs and Bu_4NOH-TOCNFs water suspensions (0.1 wt.%).

Material	Medium	Concentration [wt.%]	Zeta potential [mV]	Literature reference [mV]
TOCNF	water	0.1	-54.5	-55.8*
Bu_4NOH-TOCNF	water	0.1	-39.0	-

*Wei, Jinguang, Yufei Chen, Hongzhi Liu, Chungui Du, Huilong Yu, and Zhongxi Zhou. «Thermo-Responsive and Compression Properties of TEMPO-Oxidized Cellulose Nanofiber-Modified PNIPAm Hydrogels». *Carbohydrate Polymers* 147 (20 August 2016): 201–7. https://doi.org/10.1016/j.carbpol.2016.04.015.

4.3. Characteristics of Reference and Composite Resins

4.3.1. Rheological Behaviour of Reference and Composite Resins

The flow curves (Figure 33) show a higher viscosity for TMPTMP, while both TMPDE and reference resin exhibit higher fluidity. At low viscosities (≤ 100 mPa·s) the plate-plate geometry loses accuracy at low shear rates because it can't measure the torque in a precise way, therefore the results in that region can be affected by errors.

As far as the nanocomposite resins are concerned, the presence of the fillers leads to a clear increase in viscosity compared to the reference resin and the behaviour is shear thinning, whereas, when varying the concentration of TOCNF from 0.5 to 1 wt.%, the difference in viscosity is rather low due to the fact that a lower concentration of fillers allows for better dispersion in the matrix.

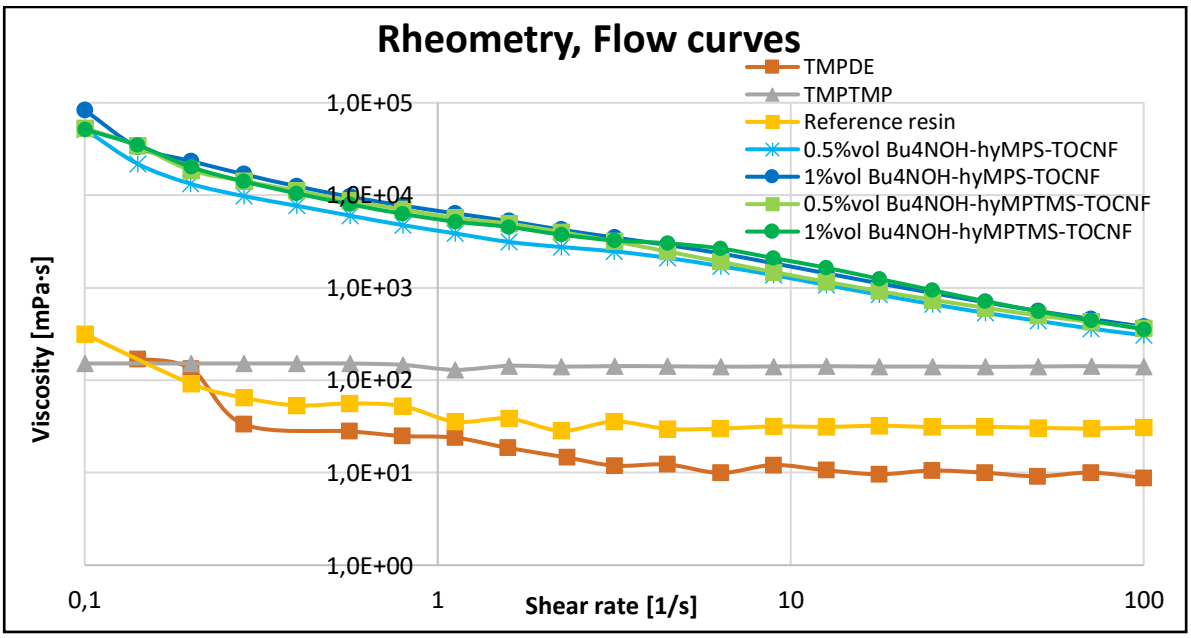

Figure 33- Flow curves of TMPDE and TMPTMP monomers, reference resin and nanocomposite resins with different compositions, before UV-curing step.

4.3.2. UV-Curing of Reference and Composite Resins

The FT-IR technique was used to evaluate the thiol-ene reaction between TMPDE and TMPTMP, following the photoinitiation by DMPA, in particular by analyzing the liquid ene and thiol monomers and the UV-cured thiol-ene reference resin by focusing on the C=C and SH groups involved in the reaction.

By comparing the FT-IR spectra of the different species (Figure 34), the disappearance of the C=C (920, 1600 and 3080 cm^{-1}) and SH (2550 cm^{-1}) groups, present in the monomers, following UV photo-crosslinking is evident, confirming that the reaction has taken place.

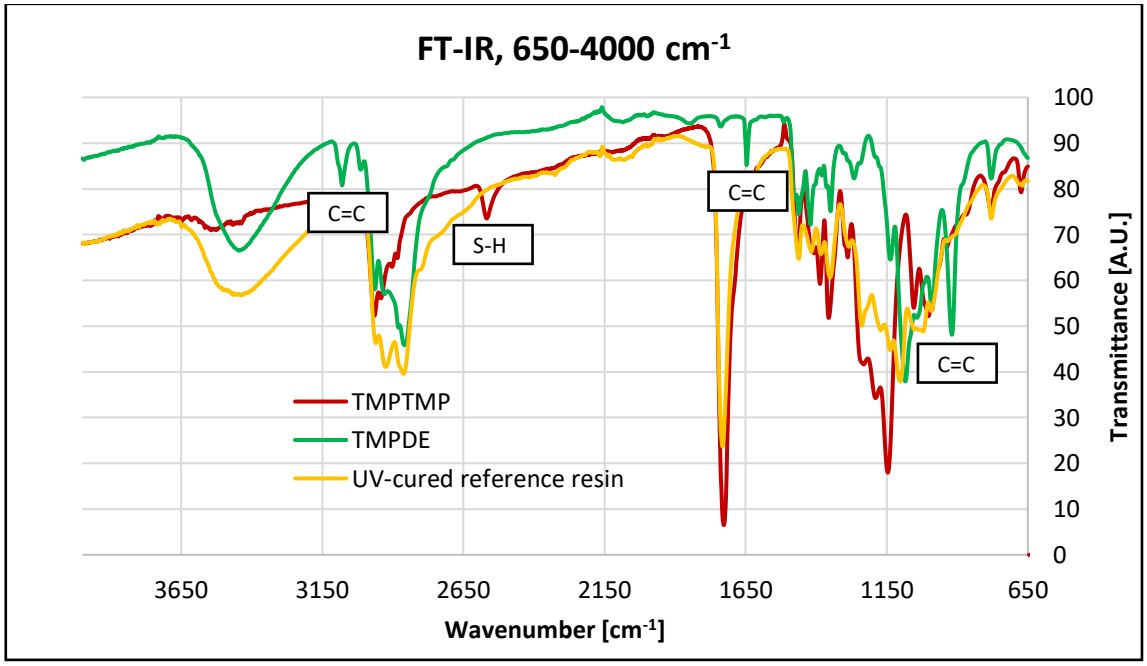

Figure 34- FT-IR spectra of TMPDE, TMPTMP and UV-cured reference resin.

Based on the results of photo-rheometry (Figure 35), it is observed that the introduction of TOCNFs causes a higher initial viscosity due to the increased particle-particle and particle-medium interactions and decreased interparticle distance, but, despite this, all nanocomposite formulations are characterized by a rapid photo-crosslinking reaction. Indeed, nanocomposite resins reach machine viscosity upper limit in times comparable to reference resin or even shorter (about 4-5 s). In contrast, 1 vol.% Bu_4NOH-hyMPTMS-TOCNF resin is characterized by a slower reaction.

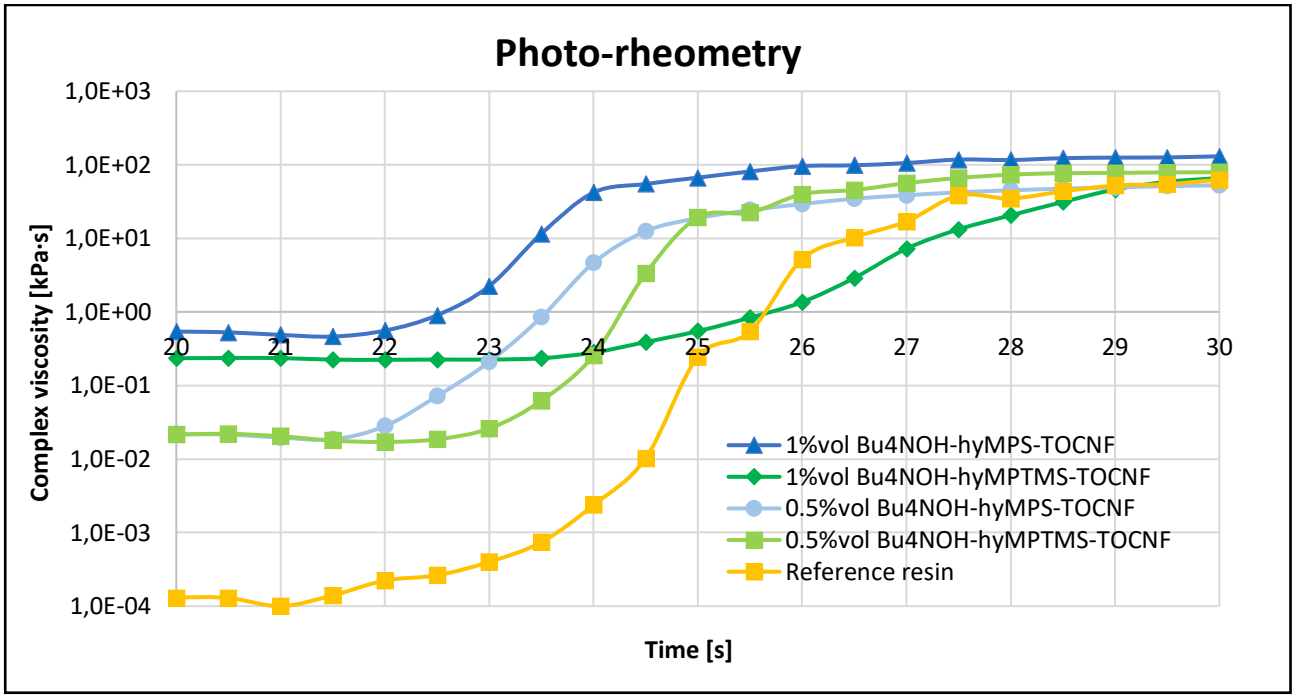

Figure 35- Photo-rheometry curves of reference resin and nanocomposite resins with different compositions, subjected to 5.5 mW/cm² light intensity to analyse the photo-crosslinking kinetics.

By analyzing the photo-DSC curves obtained (Figure 36) and focusing on the time needed to reach the top of the peak (Time to peak), the area of the peak (Peak area) and the total time needed to complete the reaction (Total reaction time) (Table VIII), it is observed that the addition of modified TOCNFs inside the resin allows to obtain a higher reaction speed than the reference resin, even if a higher concentration of TOCNFs is used, passing from 0.5 to 1 wt.%, and specifically the nanocomposite resin with 1%vol Bu_4NOH-hyMPS-TOCNF presents the highest reaction rate.

The light intensity of 0.5 mW/cm^2 was used to allow to obtain a measurable kinetics, as a consequence a slower reaction, compared to photo-rheometry measurements, is observed. In general, the photo-crosslinking reaction is rapid for all formulations as it takes about 30 s to reach the top of the peak and about 4 min to reach the complete reaction. However, when comparing the time required to reach approximately the end of the reaction, it is evident that the formulation with 1%vol Bu_4NOH-hyMPTMS-TOCNF needs a visibly longer time (280 s) to complete the reaction than the other formulations (approx. 240 s).

Furthermore, it has been noted that the use of hyMPS as a modification allows to reach a higher reaction rate than in the case of hyMPTMS modified TOCNFs, as well as a greater reactivity, proven

by obtaining a higher peak area. In addition, the modification with hyMPTMS also determines a clearly smaller peak area and therefore a lower reactivity even with respect to reference resin.

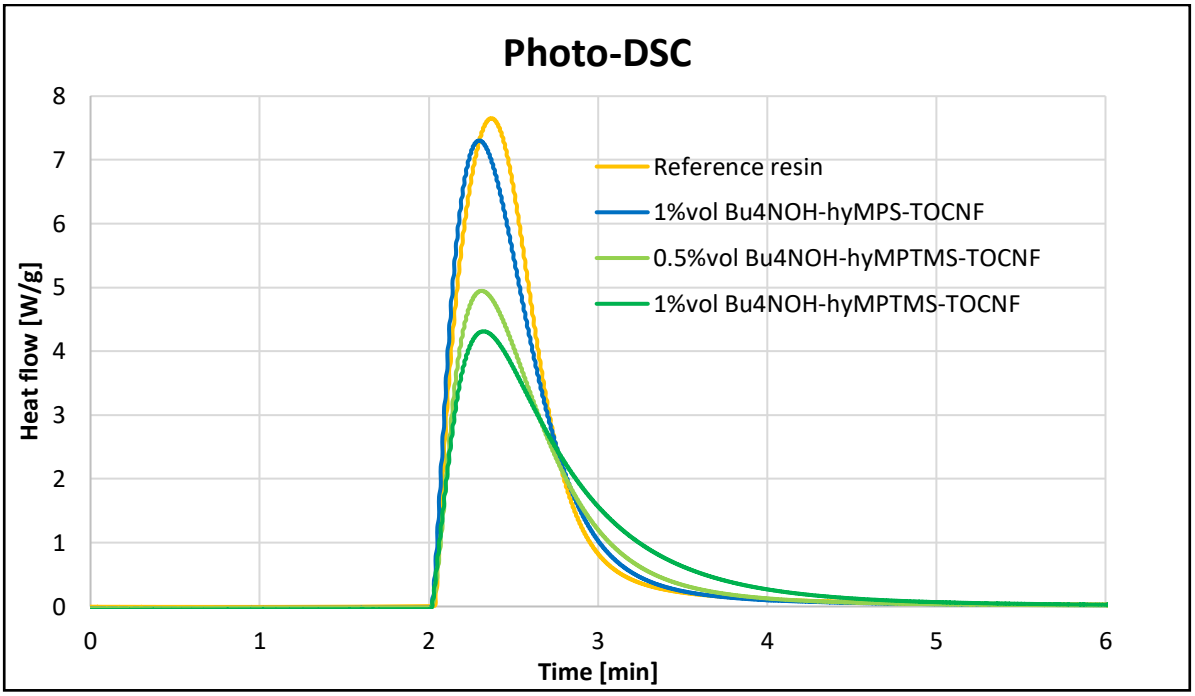

Figure 36- Photo-DSC curves of reference resin and nanocomposite resins with different compositions, subjected to 0.5 mW/cm² light intensity to analyse the photo-crosslinking kinetics.

Table VIII: Photo-DSC parameters obtained from the analysis of the photo-DSC curves of reference resin and nanocomposite resins with different compositions.

Material	Time to peak [s]	Peak area [J/g]	Total reaction time* [s]	
			0.1 W/g	0.01 W/g
Reference resin	33	280	247	567
1 vol.% Bu_4NOH-hyMPS-TOCNF	27	278	238	466
0.5 vol.% Bu_4NOH-hyMPTMS-TOCNF	27	226	249	416
1 vol.% Bu_4NOH-hyMPTMS-TOCNF	30	254	281	538

*It represents the time necessary to reach the threshold showed in the upper columns in term of heat flow [W/g].

4.4. Material Properties of Cured Reference and Composite Films

4.4.1. Transmission and Transparency Properties of Cured Reference and Composite Films

UV-Vis spectra (Figure 37) show that it is possible to obtain mostly transparent nanocomposite films (approx. 85-90% transmittance) (Figure 38), comparable to reference resin, if the concentration of TOCNFs is sufficiently low, in particular ≤ 5 vol.%, and surface modifications are applied to the cellulose nanofibrils as they result with well-dispersed fillers inside the polymer matrix.

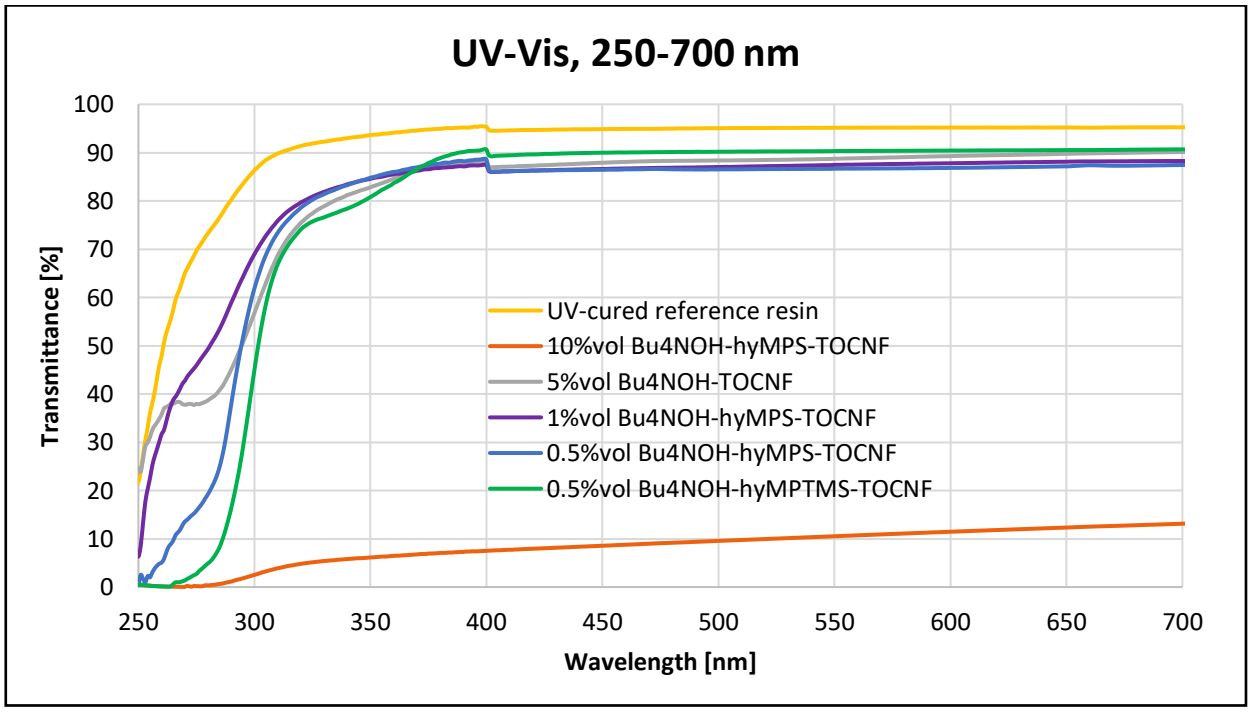

Figure 37- UV-Vis spectra of UV-cured nanocomposite films with different compositions compared to UV-cured reference resin film.

Figure 38- Transparency of UV-cured nanocomposite films with 1%vol Bu_4NOH-hyMPS-TOCNF.

4.4.2. Thermal Stability of Cured Reference and Composite Films

The resulting TGA curves (Figure 39) showed that the cured reference resin has a higher thermal stability (T_{onset} ≈ 350 °C) than the TOCNFs (T_{onset} ≈ 215 °C) and the degradation process is also different in terms of the number of degradation steps. In fact, the cellulose nanofibrils undergo 3 degradation steps at different temperatures while the reference resin only undergoes a single step, as also shown by the derivative TGA curves. Finally, the thermal stability of the UV-cured nanocomposite film is not affected by the presence of TOCNFs, maintaining a T_{onset} comparable to the reference resin (around 340 °C), as well as a similar thermal degradation process characterized by a single step.

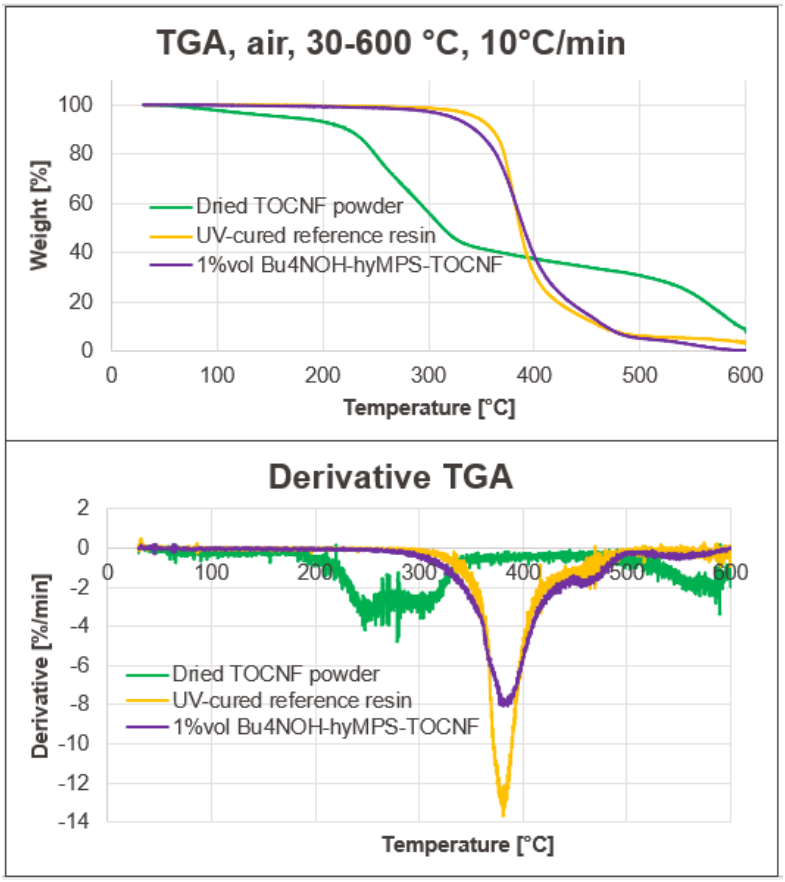

Figure 39- TGA and derivative TGA (DTGA) curves of UV-cured reference resin, dried TOCNF powder and UV-cured nanocomposite film with 1 vol.% of Bu_4NOH-hyMPS-TOCNF tested in air between 30-600 °C with a constant rate of 10 °C /min.

4.4.3. Surface Properties of Cured Reference and Composite Films

By comparing the obtained nanoindentation results (Table IX, Figure 40), it is evident that the addition of TOCNFs allows reaching much higher reduced modulus (R.M.) and surface hardness (S.H.) values than the reference resin, especially if high concentrations of cellulose nanofibrils and hyMPTMS as surface modification are used. It is even possible to achieve 6-times higher R.M. and 3-times higher S.H. than the reference resin when 10 vol.% modified TOCNFs are added.

At low TOCNF concentrations, surface modification with hyMPTMS resulted in better mechanical properties than modification with hyMPS; this may be related to the greater reactivity of the thiol groups, which, being also present as a functionality on the cellulose nanofibrils, may have resulted in a better-connected network of particles and matrix. On the contrary, in the case of hyMPS, the C=C groups, that are present on the surface of TOCNFs, are less reactive and this might have led to the formation of a less dense network around the particles.

By observing the images obtained with the nanoindentation tool (Figure 41), it is clear that as the loading of modified TOCNFs decreases, the surface roughness is consistently reduced.

Table IX: Reduced modulus and surface hardness of the reference resin and nanocomposite cured films, measured by means of nanoindentation tests, with relative percentage variations in properties compared to the reference resin.

Material	Reduced Modulus [MPa]	Surface Hardness [MPa]	R.M. increase [%]	S.H. increase [%]
Reference resin	11.1	2.3	reference	reference
10%vol Bu_4NOH-hyMPS-TOCNF	78.5	10.1	606	346
5%vol Bu_4NOH-hyMPS-TOCNF	34.8	4.5	213	98
1%vol Bu_4NOH-hyMPS-TOCNF	13.3	2.5	19	10
1%vol Bu_4NOH-hyMPTMS-TOCNF	15.5	3.5	39	53
0.5%vol Bu_4NOH-hyMPS-TOCNF	9.6	2.2	-13	-4
0.5%vol Bu_4NOH-hyMPTMS-TOCNF	12.9	3.1	16	35

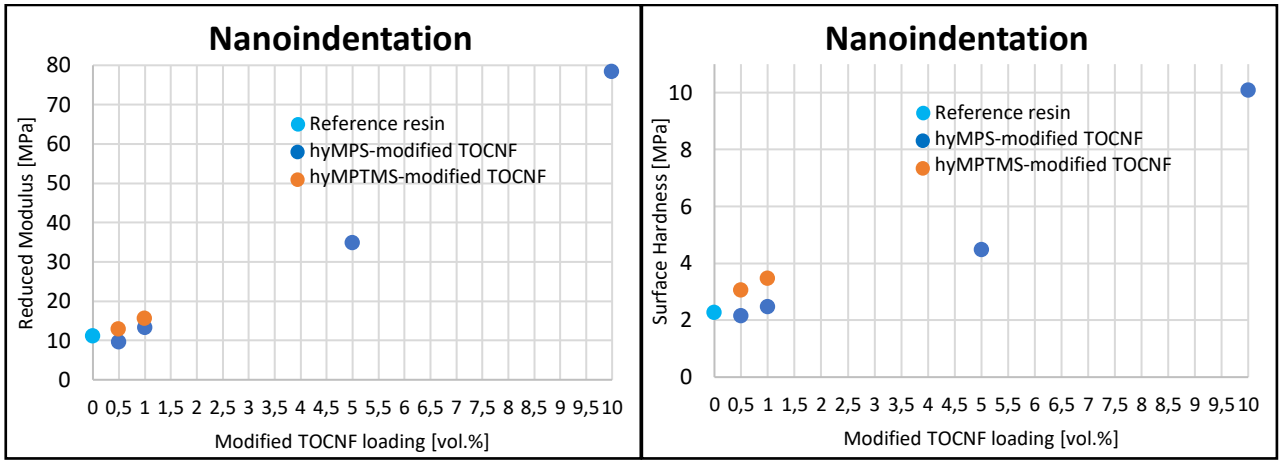

Figure 40- Graphs showing the behaviour of the reduced modulus and surface hardness of cured films of reference resin and nanocomposite resins as a function of the concentration of modified TOCNF used; results obtained through nanoindentation tests.

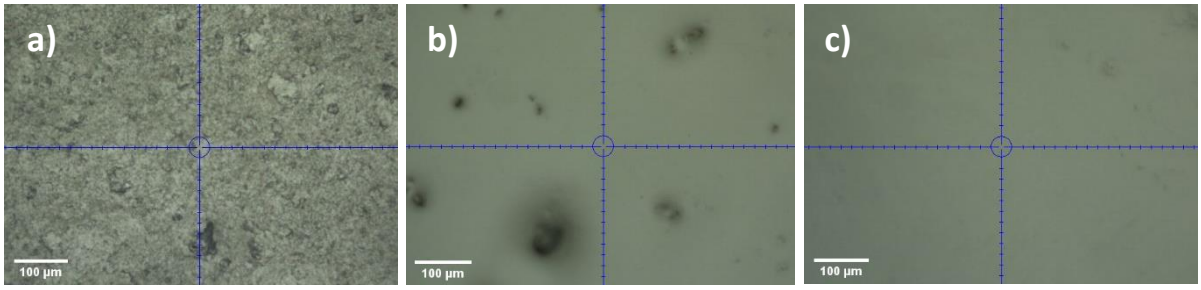

Figure 41- Nanoindentation images showing the surface roughness of cured nanocomposite films containing a) 10%vol Bu_4NOH-hyMPS-TOCNF, b) 5%vol Bu_4NOH-hyMPS-TOCNF and c) 1%vol Bu_4NOH-hyMPS-TOCNF.

Based on the results of the contact angle measurements (Table X), it is observed that the reference resin is slightly hydrophobic (78° WCA) while the introduction of modified cellulose nanofibrils allows to obtain greater hydrophobicity (about 85-90° WCA) thanks to both the increase in surface roughness and non-polarity, due to Bu_4NOH and hyMPS or hyMPTMS surface modifications of the TOCNFs.

The replication of the nanostructured surface of the lotus leaf using UV-NIL technique has allowed to produce super-hydrophobic coatings characterized by very high WCA values (Table X); the maximum WCA value reached is 155° (Figure 42), an outstanding value given that the original nature of cellulose is hydrophilic and no surfactants were used.

In addition, the self-cleaning capability was also proved by means of the test with pepper grains described in section 3.5.9. Specifically, by tilting the patterned composite film by 25°, it was possible to clean the surface with water drops (Figure 43). The sliding angle is highly dependent on the material used, in our case it was not functionalized with fluorine, which is often used to increase

hydrophobicity and self-cleaning properties due to its migration and accumulation on the surface [64], so the result is still impressive.

Pepper grains are characterized by their hydrophobic nature, so they adhere strongly to the super-hydrophobic film. However, due to the nano-patterning, the contact area between the particles and the surface is very small and thus the water droplets are still able to capture the hydrophobic contaminants while sliding. This further demonstrates the effectiveness of nanoimprinting the nanocomposite film.

Table X: Contact angle measurements results, displaying average contact angle values calculated between 5 values.

Material	Water [°]			Ethylene Glycol [°]	Diiodomethane [°]
	Flat	Lotus patterned			
		Average	Max		
Reference resin	78.1 ± 0.8	139 ± 8	147	50.3 ± 1.3	42.3 ± 0.7
0.5%vol Bu_4NOH-hyMPS-TOCNF	87.6 ± 0.3	144 ± 11	155	49.7 ± 0.2	35.1 ± 1.9
0.5%vol Bu_4NOH-hyMPTMS-TOCNF	86.6 ± 0.7	140 ± 10	150	55.6 ± 0.8	26.6 ± 1.2
1%vol Bu_4NOH-hyMPS-TOCNF	83.8± 0.8	-	-	53.7 ± 1.2	23.1 ± 2.3
1%vol Bu_4NOH-hyMPTMS-TOCNF	89.5 ± 0.6	-	-	59.8 ± 2.0	29.9 ± 1.9

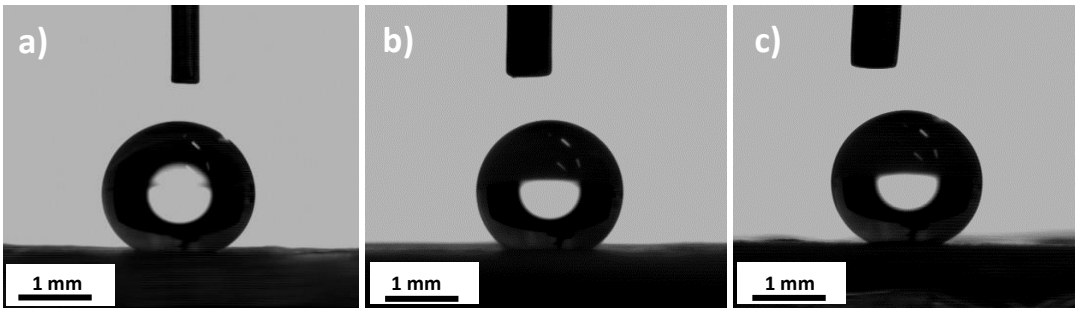

Figure 42- Pictures showing the morphology of the 8 µL water drop on the surface of a) reference resin (with 147 ° WCA), b) 0.5% vol Bu_4NOH-hyMPTMS-TOCNF (with 150° WCA) and c) 0.5% vol Bu_4NOH-hyMPS-TOCNF (with 155° WCA), lotus leaf nano-patterned film.

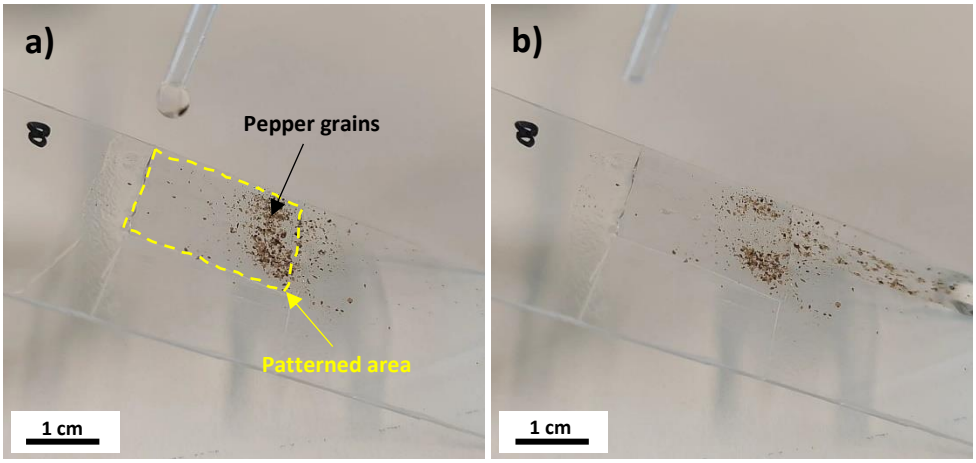

Figure 43- Pictures showing the behaviour of lotus leaf nano-patterned composite film (0.5%vol Bu_4NOH-hyMPS-TOCNF) contaminated by pepper grains on the surface: a) before water cleaning, b) after cleaning, water droplets captured pepper grains while sliding and a clean trace has been left on the imprinted surface.

As shown by the SEM images (Figure 44), the PDMS mold produced is able to mimic the rough micro- and nano-structured surface of the lotus leaf, in the form of a negative replica.

Regarding the UV-NIL imprinted reference resin film, the positive replication of the lotus surface is not completely successful since the micropapillae have been copied but not the nanopillars at the top; moreover, the morphology is also characterized by flat regions and, consequently, the wrinkled surface of the lotus leaf is not mimicked in an optimal way.

On the contrary, the nano-imprinted nanocomposite film with 0.5%vol Bu_4NOH-hyMPS-TOCNF shows an optimal replication of micropapillae, nanopillars and rough surface, allowing to obtain even greater super-hydrophobic properties than the reference resin, in agreement with the WCA results. The more precise replication of the nanostructure shape is most probably due to the improved mechanical properties obtained following the addition of cellulose nanofibrils.

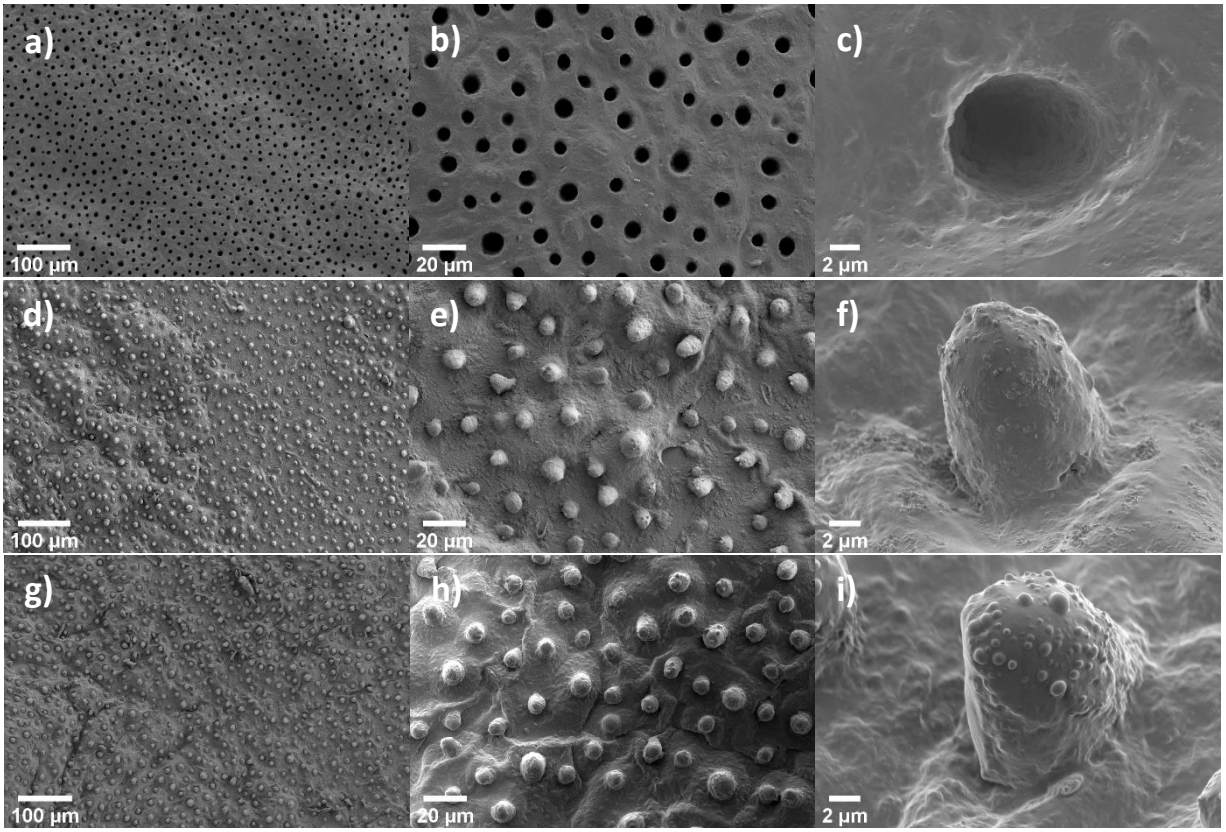

Figure 44- SEM images at 3 different magnifications (150X, 600X and 4000X respectively) of PDMS negative replica of lotus leaf hierarchical surface (a-c), UV-NIL imprinted reference resin film (d-f) and UV-NIL imprinted 0.5%vol Bu_4NOH-hyMPS-TOCNF nanocomposite resin film.

In conclusion, it was not possible to produce imprinted nanocomposite films characterized by concentrations of modified TOCNFs greater than 0.5 vol.% because the cured film broke during peeling off from the PDMS mold surface following the UV-NIL step. As shown in the SEM images (Figure 45), part of the film remains attached to the PDMS mold leading to an imperfect replication and rendering the mold incapable for repeated use.

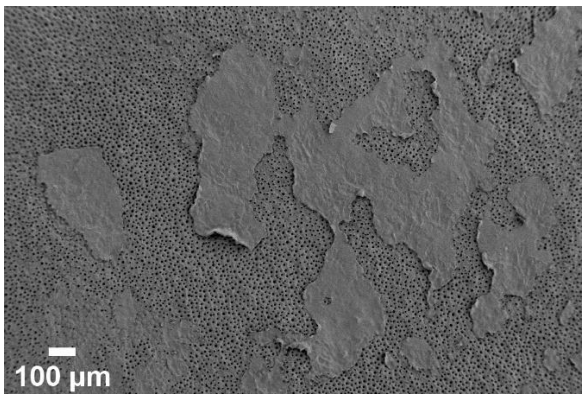

Figure 45- SEM image of PDMS mold surface after UV-NIL imprinting of 1%vol Bu_4NOH-hyMPS-TOCNF nanocomposite resin, showing the residues of the imprinted cured film remaining on the PDMS surface following peeling off.

5. Conclusions

The focus of this thesis is the processing of a UV curable thiol-ene-based resin with the addition of cellulose nanofibrils as fillers to produce a nanocomposite film.

The use of cellulose, a bio-based material obtainable from numerous natural sources, made it possible to improve the low mechanical performance of the polymer matrix, as well as obtaining remarkable surface properties.

The possibility of employing thiol-ene “click” chemistry and UV photo-crosslinking enables very fast, simple processing without oxygen inhibition, as shown by photo-rheometry and photo-differential scanning calorimetry (photo-DSC) analyses.

Through the testing of several alternative processing steps, an optimised method was achieved; the main objective of preparing a processable free-flowing composite resin, characterized by a well dispersed fillers, was accomplished, opening to the possibility of further processing methods such as printing. In addition, the constituent components of the resin are kept to a minimum, as no surfactants, dispersants or reactive solvents are used.

Furthermore, due to the effectiveness of the surface modifications applied on the TOCNFs, an improved compatibility and excellent dispersion of the fibrils in the resin was achieved. This allowed the reinforcement to be fully exploited while maintaining the typical transparency of the thiol-ene matrix, as proven by nanoindentation and UV-Vis spectroscopy analyses respectively.

By means of the thermogravimetric analysis (TGA), it was observed that the thermal stability of the composite remains almost unchanged compared to that of the polymer, even though the TOCNFs are characterized by a lower thermal degradation temperature.

A complete characterization was carried out both on the raw materials, i.e. the UV curable thiol-ene system and the TOCNFs, and on the nanocomposite films produced.

Focusing on surface and wettability properties, an application was proposed based on mimicking the hierarchical surface of a lotus leaf in order to achieve super-hydrophobic behaviour.

Despite the hydrophilic nature of cellulose, the use of surface modifications to improve compatibility with a non-polar matrix and an increase in surface roughness increased the material's hydrophobicity. The use of the UV-NIL technique was successful in replication, as evidenced by SEM and WCA measurements, so it was possible to produce a transparent, micro- and nano-structured,

super-hydrophobic nanocomposite patterned film with enhanced mechanical properties and self-cleaning capability that may be promising in various application fields where protective coatings are used. In addition, it was observed that the addition of cellulose nanofibrils also allowed a more precise replication of the micro-nanosized structure shape, most probably due to the improved mechanical properties, which improves the usage possibilities of thiol-enes for the UV-NIL process in both research and manufacturing.

Thanks to the promising features of the nanocomposite films obtained, it would be interesting to implement the characterization regarding the properties of wear resistance, essential in case of use as a protective coating.

A further future perspective can be based on the proven processability through UV-NIL, as demonstrated by this project, and to the well-known narrow glass transition of thiol-ene based resins [5], which could allow to produce nanopatterned films characterized by tunable mechanical properties through the control of process parameters, thiol-ene ratio, filler loading etc. and shape memory capabilities, as recently demonstrated by Zhang X. et al. [70].

Acknowledgements

The master thesis project was entirely developed at EPFL Laboratory for Processing of Advanced Composites (LPAC). The SEM (and EDX) analysis were carried out at EPFL Interdisciplinary Center for Electron Microscopy (CIME) and the other material characterizations at EPFL Hybrid Materials Characterization Center (MHMC). The botanical garden of Lausanne is acknowledged for the supply of fresh lotus leaves.

A special thanks goes out to my family and friends who have always supported me and been there for me, despite the distance.

I would also like to thank Dr. Yves Leterrier and Prof. Marco Sangermano for allowing me to do my Master thesis at the Laboratory for Processing of Advanced Composites (LPAC) at EPFL and for helping me with their valuable advice and expertise.

A big thank you to my supervisor Alper Balkan for always being present and willing to help me with his great skills, even in difficult times, making them lighter.

Finally, a general thank you to all my colleagues at LPAC who made me feel part of the group right from the start and helped me with their great knowledge, always very helpful.

References

1. «Photopolymerization». In *Polymers and Light*, 273–304. John Wiley & Sons, Ltd, 2007. https://doi.org/10.1002/9783527611027.ch10.
2. Chiulan, Ioana, Ellinor Bævre Heggset, Ştefan Ioan Voicu, and Gary Chinga-Carrasco. «Photopolymerization of Bio-Based Polymers in a Biomedical Engineering Perspective». *Biomacromolecules* 22, n. 5 (10 May 2021): 1795–1814. https://doi.org/10.1021/acs.biomac.0c01745.
3. «Ultraviolet (UV) Radiation». Visited on 21 April 2022. https://www.cancer.org/cancer/cancer-causes/radiation-exposure/uv-radiation.html.
4. Kolb, Hartmuth C., M. G. Finn, and K. Barry Sharpless. «Click Chemistry: Diverse Chemical Function from a Few Good Reactions». *Angewandte Chemie International Edition* 40, n. 11 (2001): 2004–21. https://doi.org/10.1002/1521-3773(20010601)40:11<2004::AID-ANIE2004>3.0.CO;2-5.
5. Hoyle, Charles E., and Christopher N. Bowman. «Thiol–Ene Click Chemistry». *Angewandte Chemie International Edition* 49, n. 9 (2010): 1540–73. https://doi.org/10.1002/anie.200903924.
6. Sharma, Anjali, and Ashok Kakkar. «Designing Dendrimer and Miktoarm Polymer Based Multi-Tasking Nanocarriers for Efficient Medical Therapy». *Molecules* 20, n. 9 (2015): 16987–15. http://dx.doi.org/10.3390/molecules200916987.
7. Northrop, Brian H., and Roderick N. Coffey. «Thiol–Ene Click Chemistry: Computational and Kinetic Analysis of the Influence of Alkene Functionality». *Journal of the American Chemical Society* 134, n. 33 (22 August 2012): 13804–17. https://doi.org/10.1021/ja305441d.
8. Natali, Marco, Stefano Begolo, T. Carofiglio, and Giampaolo Mistura. «Rapid Prototyping of Multilayer Thiolene Microfluidic Chips by Photopolymerization and Transfer Lamination». *Lab on a Chip* 8, n. 3 (27 February 2008): 492–94. https://doi.org/10.1039/B716594C.
9. Chen, Gaojian, Sadik Amajjahe, and Martina H. Stenzel. «Synthesis of Thiol-Linked Neoglycopolymers and Thermo-Responsive Glycomicelles as Potential Drug Carrier». *Chemical Communications*, n. 10 (24 February 2009): 1198–1200. https://doi.org/10.1039/B900215D.
10. Brigo, Laura, Tommaso Carofiglio, Carlo Fregonese, Filippo Meneguzzi, Giampaolo Mistura, Marco Natali, and Umberto Tonellato. «An Optical Sensor for PH Supported onto Tentagel Resin Beads». *Sensors and Actuators B: Chemical*, Proceedings of the Eleventh International Meeting on Chemical Sensors IMCS-11, 130, n. 1 (14 March 2008): 477–82. https://doi.org/10.1016/j.snb.2007.09.020.
11. Triola, Gemma, Luc Brunsveld, and Herbert Waldmann. «Racemization-Free Synthesis of S-Alkylated Cysteines via Thiol-ene Reaction». *The Journal of Organic Chemistry* 73, n. 9 (1 May 2008): 3646–49. https://doi.org/10.1021/jo800198s.
12. Hung, Lung-Hsin, Robert Lin, and Abraham Phillip Lee. «Rapid Microfabrication of Solvent -Resistant Biocompatible Microfluidic Devices». *Lab on a Chip* 8, n. 6 (2008): 983–87. https://doi.org/10.1039/B717710K.
13. Khire, Vaibhav S., Youngwoo Yi, Noel A. Clark, and Christopher N. Bowman. «Formation and Surface Modification of Nanopatterned Thiol-ene Substrates using Step and Flash Imprint Lithography». *Advanced Materials* 20, n. 17 (2008): 3308–13. https://doi.org/10.1002/adma.200800672.
14. Y. Li, Christopher, Michael J. Birnkrant, Lalgudi V. Natarajan, Vincent P. Tondiglia, Pamela F. Lloyd, Richard L. Sutherland, and Timothy J. Bunning. «Polymer Crystallization /Melting Induced Thermal Switching in a Series of Holographically Patterned Bragg Reflectors». *Soft Matter* 1, n. 3 (2005): 238–42. https://doi.org/10.1039/B506876B.
15. Trey, Stacy M., E. Kristofer Gamstedt, Edith Mäder, Sonny Jönsson, and Mats Johansson. «Glass Fiber Reinforced High Glass Transition Temperature Thiol–Ene Networks». *Composites Part A: Applied Science and Manufacturing* 42, n. 11 (November 2011): 1800–1808. https://doi.org/10.1016/j.compositesa.2011.08.003.
16. Yu, Bin, Xin Wang, Weiyi Xing, Hongyu Yang, Xiaofeng Wang, Lei Song, Yuan Hu, and Siuming Lo. «Enhanced Thermal and Mechanical Properties of Functionalized Graphene/Thiol-Ene Systems by Photopolymerization

Technology». *Chemical Engineering Journal* 228 (July 2013): 318–26. https://doi.org/10.1016/j.cej.2013.04.093.

17. Prakasam, Mythili, Janis Locs, Kristine Salma-Ancane, Dagnija Loca, Alain Largeteau, and Liga Berzina-Cimdina. «Biodegradable Materials and Metallic Implants—A Review». *Journal of Functional Biomaterials* 8, n. 4 (December 2017): 44. https://doi.org/10.3390/jfb8040044.
18. Weiss, Martin, Juliane Haufe, Michael Carus, Miguel Brandão, Stefan Bringezu, Barbara Hermann, e Martin K. Patel. «A Review of the Environmental Impacts of Biobased Materials». *Journal of Industrial Ecology* 16, n. s1 (2012): S169–81. https://doi.org/10.1111/j.1530-9290.2012.00468.x.
19. Nechyporchuk, Oleksandr, Mohamed Naceur Belgacem, and Julien Bras. «Production of Cellulose Nanofibrils: A Review of Recent Advances». *Industrial Crops and Products* 93 (December 2016): 2–25. https://doi.org/10.1016/j.indcrop.2016.02.016.
20. Wiedenhoeft, Alex. «Structure and Function of Wood». Wood Handbook: Wood as an Engineering Material: Chapter 3. Centennial Ed. General Technical Report FPL; GTR-190. Madison, WI: U.S. Dept. of Agriculture, Forest Service, Forest Products Laboratory, 2010: P. 3.1-3.18. 190 (2010): 3.1-3.18.
21. Stelte, Wolfgang, e Anand R. Sanadi. «Preparation and Characterization of Cellulose Nanofibers from Two Commercial Hardwood and Softwood Pulps». *Industrial & Engineering Chemistry Research* 48, n. 24 (16 dicembre 2009): 11211–19. https://doi.org/10.1021/ie9011672.
22. Spinu, Monica, Nuno Dos Santos, Nicolas Le Moigne, and Patrick Navard. «How Does the Never-Dried State Influence the Swelling and Dissolution of Cellulose Fibres in Aqueous Solvent?» *Cellulose* 18, n. 2 (April 2011): 247–56. https://doi.org/10.1007/s10570-010-9485-8.
23. Klemm, Dieter, Brigitte Heublein, Hans-Peter Fink, and Andreas Bohn. «Cellulose: Fascinating Biopolymer and Sustainable Raw Material». *Angewandte Chemie International Edition* 44, n. 22 (2005): 3358–93. https://doi.org/10.1002/anie.200460587.
24. Xu, Xuezhu, Fei Liu, Long Jiang, J. Y. Zhu, Darrin Haagenson, and Dennis P. Wiesenborn. «Cellulose Nanocrystals vs. Cellulose Nanofibrils: A Comparative Study on Their Microstructures and Effects as Polymer Reinforcing Agents». *ACS Applied Materials & Interfaces* 5, n. 8 (24 April 2013): 2999–3009. https://doi.org/10.1021/am302624t.
25. The Process Development Center. «UMaine Nanomaterial Pilot Plant - The Process Development Center - University of Maine». Visited on 21 April 2022. https://umaine.edu/pdc/nanocellulose/umaine-nanomaterial-pilot-plant/.
26. Isogai, Akira, Tsuguyuki Saito, and Hayaka Fukuzumi. «TEMPO-Oxidized Cellulose Nanofibers». *Nanoscale* 3, n. 1 (2011): 71–85. https://doi.org/10.1039/C0NR00583E.
27. Janardhnan, Sreekumar, and Mohini M. Sain. «Isolation of Cellulose Microfibrils - An Enzymatic Approach». *BioResources* 1, n. 2 (21 September 2006): 176–88. https://doi.org/10.15376/biores.1.2.176-188.
28. Bäckström, M., Bolivar, S., and Paltakari, J. «Effect of ionic form on fibrillation and the development of the fibre network strength during the refining of the kraft pulps». *O Papel: Revista Mensal de Tecnologia em Celulose*, n. 73 (2012): 57–65. https://www.academia.edu/22921261/Effect_of_ionic_form_on_fibrillation_and_the_development_of_the_fibre_network_strength_during_the_refining_of_the_kraft_pulps.
29. Omanović-Mikličanin, Enisa, Almir Badnjević, Anera Kazlagić, e Muhamed Hajlovac. «Nanocomposites: A Brief Review». *Health and Technology* 10, n. 1 (1 January 2020): 51–59. https://doi.org/10.1007/s12553-019-00380-x.
30. Casati, Riccardo, and Maurizio Vedani. «Metal Matrix Composites Reinforced by Nano-Particles—A Review». *Metals* 4, n. 1 (March 2014): 65–83. https://doi.org/10.3390/met4010065.
31. Behera, Ajit, Biswajit Swain, and Deepak Kumar Sahoo. «Chapter 16 - Fiber-Reinforced Ceramic Matrix Nanocomposites», *Fiber-Reinforced Nanocomposites: Fundamentals and Applications*, 359–68. Micro and Nano Technologies. Elsevier, 2020. https://doi.org/10.1016/B978-0-12-819904-6.00016-5.

32. Hussain, Farzana, Mehdi Hojjati, Masami Okamoto, and Russell E. Gorga. «Review Article: Polymer-Matrix Nanocomposites, Processing, Manufacturing, and Application: An Overview». *Journal of Composite Materials* 40, n. 17 (1 September 2006): 1511–75. https://doi.org/10.1177/0021998306067321.
33. Ju-Nam, Yon, and Jamie R. Lead. «Manufactured Nanoparticles: An Overview of Their Chemistry, Interactions and Potential Environmental Implications». *Science of The Total Environment* 400, n. 1 (1 August 2008): 396–414. https://doi.org/10.1016/j.scitotenv.2008.06.042.
34. Naganuma, T., and Y. Kagawa. «Effect of Particle Size on the Optically Transparent Nano Meter-Order Glass Particle-Dispersed Epoxy Matrix Composites». *Composites Science and Technology* 62, n. 9 (1 July 2002): 1187–89. https://doi.org/10.1016/S0266-3538(02)00059-3.
35. Singh, R. P., M. Zhang, and D. Chan. «Toughening of a Brittle Thermosetting Polymer: Effects of Reinforcement Particle Size and Volume Fraction». *Journal of Materials Science* 37, n. 4 (1 February 2002): 781–88. https://doi.org/10.1023/A:1013844015493.
36. Alexandre, Michael, and Philippe Dubois. «Polymer-Layered Silicate Nanocomposites: Preparation, Properties and Uses of a New Class of Materials». *Materials Science and Engineering: R: Reports* 28, n. 1 (15 June 2000): 1–63. https://doi.org/10.1016/S0927-796X(00)00012-7.
37. Thostenson, Erik T., Chunyu Li, and Tsu-Wei Chou. «Nanocomposites in Context». *Composites Science and Technology*, JNC13-AMAC-Strasbourg, 65, n. 3 (1 March 2005): 491–516. https://doi.org/10.1016/j.compscitech.2004.11.003.
38. Tan, E. P. S., and C. T. Lim. «Mechanical Characterization of Nanofibers – A Review». *Composites Science and Technology*, Nanocomposites, 66, n. 9 (1 July 2006): 1102–11. https://doi.org/10.1016/j.compscitech.2005.10.003.
39. Chatterjee, A., and B. L. Deopura. «Carbon Nanotubes and Nanofibre: An Overview». *Fibers and Polymers* 3, n. 4 (1 December 2002): 134–39. https://doi.org/10.1007/BF02912657.
40. Karabulut, Fabrice N. H., Günther Höfler, Naveen Ashok Chand, and Gareth W. Beckermann. «Electrospun Nanofibre Filtration Media to Protect against Biological or Nonbiological Airborne Particles». *Polymers* 13, n. 19 (2021). https://doi.org/10.3390/polym13193257.
41. Bhattarai, Shanta Raj, Narayan Bhattarai, Ho Keun Yi, Pyong Han Hwang, Dong Il Cha, and Hak Yong Kim. «Novel Biodegradable Electrospun Membrane: Scaffold for Tissue Engineering». *Biomaterials* 25, n. 13 (1 June 2004): 2595–2602. https://doi.org/10.1016/j.biomaterials.2003.09.043.
42. Sundararajan, Sriram, Bharat Bhushan, Takahiro Namazu, and Yoshitada Isono. «Mechanical Property Measurements of Nanoscale Structures Using an Atomic Force Microscope». *Ultramicroscopy*, Proceedings of the third International Conference on Scaning Prob e Microscopy, Sensors and Nanostructures, 91, n. 1 (1 May 2002): 111–18. https://doi.org/10.1016/S0304-3991(02)00089-X.
43. Islam, Md Saiful, Reza Masoodi, and Hossein Rostami. «The Effect of Nanoparticles Percentage on Mechanical Behavior of Silica-Epoxy Nanocomposites». *Journal of Nanoscience* 2013 (22 December 2013): 1–10. https://doi.org/10.1155/2013/275037.
44. Omanović-Mikličanin, Enisa, Almir Badnjević, Anera Kazlagić, and Muhamed Hajlovac. «Nanocomposites: A Brief Review». *Health and Technology* 10, n. 1 (January 2020): 51–59. https://doi.org/10.1007/s12553-019-00380-x.
45. Wong, Dominick, Mahmood Anwar, Sujan Debnath, Abdul Hamid, and S. Izman. «A Review: Recent Development of Natural Fiber-Reinforced Polymer Nanocomposites». *JOM* 73, n. 8 (1 August 2021): 2504–15. https://doi.org/10.1007/s11837-021-04749-0.
46. Pielichowski, Krzysztof, and Kinga Pielichowska. «Chapter 11 - Polymer Nanocomposites», *Handbook of Thermal Analysis and Calorimetry*, 6:431–85. Recent Advances, Techniques and Applications. Elsevier Science B.V., 2018. https://doi.org/10.1016/B978-0-444-64062-8.00003-6.
47. Keledi, Gergely, József Hári, and Béla Pukánszky. «Polymer Nanocomposites: Structure, Interaction, and Functionality». *Nanoscale* 4, n. 6 (2012): 1919–38. https://doi.org/10.1039/C2NR11442A.

48. Abitbol, Tiffany, Amit Rivkin, Yifeng Cao, Yuval Nevo, Eldho Abraham, Tal Ben-Shalom, Shaul Lapidot, and Oded Shoseyov. «Nanocellulose, a Tiny Fiber with Huge Applications». *Current Opinion in Biotechnology*, Systems biology, Nanobiotechnology, 39 (1 June 2016): 76–88. https://doi.org/10.1016/j.copbio.2016.01.002.
49. Isogai, Akira, and Lennart Bergström. «Preparation of Cellulose Nanofibers Using Green and Sustainable Chemistry». *Current Opinion in Green and Sustainable Chemistry*, Green and Sustainable Nanotechnology / Selected papers from the ACS Symposium on Green chemistry synthesis of nanomaterials and manufacturing, 12 (1 August 2018): 15–21. https://doi.org/10.1016/j.cogsc.2018.04.008.
50. Poothanari, Mohammed Arif, Aigoul Schreier, Karim Missoum, Julien Bras, and Yves Leterrier. «Photocured Nanocellulose Composites: Recent Advances». *ACS Sustainable Chemistry & Engineering* 10, n. 10 (14 March 2022): 3131–49. https://doi.org/10.1021/acssuschemeng.1c07631.
51. Hubbe, Martin A., Orlando J. Rojas, Lucian A. Lucia, and Mohini Sain. «Cellulosic nanocomposite: a review». *BioResources* 3, n. 3 (31 July 2008): 929–80.
52. Fein, Kendra, Douglas W. Bousfield, and William M. Gramlich. «Thiol-Norbornene Reactions to Improve Natural Rubber Dispersion in Cellulose Nanofiber Coatings». *Carbohydrate Polymers* 250 (15 December 2020): 117001. https://doi.org/10.1016/j.carbpol.2020.117001.
53. B. Lowe, Andrew. «Thiol-Ene "Click" Reactions and Recent Applications in Polymer and Materials Synthesis». *Polymer Chemistry* 1, n. 1 (2010): 17–36. https://doi.org/10.1039/B9PY00216B.
54. Lin, Hong, Xia Wan, Xuesong Jiang, Qingkang Wang, and Jie Yin. «A Nanoimprint Lithography Hybrid Photoresist Based on the Thiol–Ene System». *Advanced Functional Materials* 21, n. 15 (2011): 2960–67. https://doi.org/10.1002/adfm.201100692.
55. Dickey, Michael D., Ryan L. Burns, E. K. Kim, Steve C. Johnson, Nick A. Stacey, and C. Grant Willson. «Study of the Kinetics of Step and Flash Imprint Lithography Photopolymerization». *AIChE Journal* 51, n. 9 (2005): 2547–55. https://doi.org/10.1002/aic.10477.
56. Dickey, Michael D., and C. Grant Willson. «Kinetic Parameters for Step and Flash Imprint Lithography Photopolymerization». *AIChE Journal* 52, n. 2 (2006): 777–84. https://doi.org/10.1002/aic.10666.
57. Nakabayashi, Kazuhiro, Shigeki Sobu, Yuji Kosuge, and Hideharu Mori. «Synthesis and Nanoimprinting of High Refractive Index and Highly Transparent Polythioethers Based on Thiol-Ene Click Chemistry». *Journal of Polymer Science Part A: Polymer Chemistry* 56, n. 19 (2018): 2175–82. https://doi.org/10.1002/pola.29181.
58. Pan, Zihe, Fangqin Cheng, and Boxin Zhao. «Bio-Inspired Polymeric Structures with Special Wettability and Their Applications: An Overview». *Polymers* 9, n. 12 (December 2017): 725. https://doi.org/10.3390/polym9120725.
59. Wang, Chunnan, Ruomei Shao, Guiqiang Wang, and Shuqing Sun. «Hierarchical Hydrophobic Surfaces with Controlled Dual Transition between Rose Petal Effect and Lotus Effect via Structure Tailoring or Chemical Modification». *Colloids and Surfaces A: Physicochemical and Engineering Aspects* 622 (5 August 2021): 126661. https://doi.org/10.1016/j.colsurfa.2021.126661.
60. Zhang, Xi, Feng Shi, Jia Niu, Yugui Jiang, and Zhiqiang Wang. «Superhydrophobic Surfaces: From Structural Control to Functional Application». *Journal of Materials Chemistry* 18, n. 6 (2008): 621–33. https://doi.org/10.1039/B711226B.
61. Bhushan, Bharat, e Michael Nosonovsky. «The rose petal effect and the modes of superhydrophobicity». *Philosophical transactions. Series A, Mathematical, physical, and engineering sciences* 368 (28 ottobre 2010): 4713–28. https://doi.org/10.1098/rsta.2010.0203.
62. Choo, Soyoung, Hak-Jong Choi, and Heon Lee. «Replication of Rose-Petal Surface Structure Using UV-Nanoimprint Lithography». *Materials Letters* 121 (15 April 2014): 170–73. https://doi.org/10.1016/j.matlet.2014.01.037.
63. Ghosh, Udita Uday, Sachin Nair, Anuja Das, Rabibrata Mukherjee, and Sunando DasGupta. «Replicating and Resolving Wetting and Adhesion Characteristics of a Rose Petal». *Colloids and Surfaces A: Physicochemical and Engineering Aspects* 561 (20 January 2019): 9–17. https://doi.org/10.1016/j.colsurfa.2018.10.028.

64. González Lazo, Marina A., Ioannis Katrantzis, Sara Dalle Vacche, Feyza Karasu, and Yves Leterrier. «A Facile in Situ and UV Printing Process for Bioinspired Self-Cleaning Surfaces». *Materials* 9, n. 9 (September 2016): 738. https://doi.org/10.3390/ma9090738.
65. Ryu, Sang-woo, Soyoung Choo, Hak-Jong Choi, Chae-Hyun Kim, and Heon Lee. «Replication of Rose Petal Surfaces Using a Nickel Electroforming Process and UV Nanoimprint Lithography». *Applied Surface Science* 322 (15 December 2014): 57–63. https://doi.org/10.1016/j.apsusc.2014.10.063.
66. Lee, Seung-Mo, and Tai Hun Kwon. «Effects of Intrinsic Hydrophobicity on Wettability of Polymer Replicas of a Superhydrophobic Lotus Leaf». *Journal of Micromechanics and Microengineering* 17, n. 4 (1 April 2007): 687–92. https://doi.org/10.1088/0960-1317/17/4/003.
67. Esfandiari, Paricher, Samuel Clark Ligon, Jean Jacques Lagref, Richard Frantz, Zoubair Cherkaoui, and Robert Liska. «Efficient Stabilization of Thiol-Ene Formulations in Radical Photopolymerization». *Journal of Polymer Science Part A: Polymer Chemistry* 51, n. 20 (2013): 4261–66. https://doi.org/10.1002/pola.26848.
68. Abdullah, Syed Z., Pierre R. Bérubé, and Derrick J. Horne. «SEM Imaging of Membranes: Importance of Sample Preparation and Imaging Parameters». *Journal of Membrane Science* 463 (1 August 2014): 113–25. https://doi.org/10.1016/j.memsci.2014.03.048.
69. Kumar, Anuj, Yuvraj Singh Negi, Veena Choudhary, and Nishi Kant Bhardwaj. «Characterization of Cellulose Nanocrystals Produced by Acid-Hydrolysis from Sugarcane Bagasse as Agro-Waste». *Journal of Materials Physics and Chemistry* 2, n. 1 (29 October 2020): 1–8. https://doi.org/10.12691/jmpc-2-1-1.
70. Zhang, Xinpeng, Lewis Cox, Zhibin Wen, Weixian Xi, Yifu Ding, and Christopher N. Bowman. «Implementation of Two Distinct Wavelengths to Induce Multistage Polymerization in Shape Memory Materials and Nanoimprint Lithography». *Polymer* 156 (November 2018): 162–68. https://doi.org/10.1016/j.polymer.2018.09.032.
71. Shimizu, Michiko, Tsuguyuki Saito, and Akira Isogai. «Bulky Quaternary Alkylammonium Counterions Enhance the Nanodispersibility of 2,2,6,6-Tetramethylpiperidine-1-oxyl-Oxidized Cellulose in Diverse Solvents». *Biomacromolecules* 15, n. 5 (12 May 2014): 1904–9. https://doi.org/10.1021/bm500384d.
72. Lu, Jue, Per Askeland, and Lawrence T. Drzal. «Surface Modification of Microfibrillated Cellulose for Epoxy Composite Applications». *Polymer* 49, n. 5 (3 MarchUV 2008): 1285–96. https://doi.org/10.1016/j.polymer.2008.01.028.
73. Galland, Sylvain, Yves Leterrier, Tommaso Nardi, Christopher J. G. Plummer, Jan Anders E. Månson, and Lars A. Berglund. «UV-Cured Cellulose Nanofiber Composites with Moisture Durable Oxygen Barrier Properties». *Journal of Applied Polymer Science* 131, n. 16 (2014). https://doi.org/10.1002/app.40604.